NEW WORLDS OBSERVER ASMCS STUDY
APPENDIX E.1

Analytical Modeling of Starshades

Webster Cash

Center for Astrophysics and Space Astronomy,

University of Colorado, Boulder, CO 80309, USA

I. Introduction

Nearly everybody wants to know if Earth-like planets abound in the Universe. Are warm, watery paradises common, and does life arise everywhere it is given a chance? To answer these age-old questions requires a very good telescope capable of pulling the signal from a faint Earth-like planet out of the glare of its parent star. We will probably have to look out to distances of 10 parsecs or more to have a good chance of finding an Earth twin (Turnbull et al, 2009). But at that distance, the Earth is only thirtieth magnitude and hovers less than 0.1 arcseconds from the star.

This is a daunting challenge for telescope builders. An m=30 object is right at the sensitivity limit of the Hubble Space Telescope. And a tenth of an arcsecond is right at the spatial resolution limit. So the telescope has to be expensive and high quality if it is to be able to resolve and study the planetary system - even if there is no glare from the star.

The Terrestrial Planet Finder program developed two approaches to building telescopes that can null out the parent star. One uses high precision nulling between spacecraft in the mid-infrared to suppress the stellar glare. The other uses wavefront control and correction in an internal coronagraph to remove the central starlight. Both approaches have proven to be dauntingly inefficient, difficult and expensive.

More recently, we resurrected the idea of an external occulter (Spitzer, 1962). The idea is to keep the starlight from ever entering the telescope where it causes such havoc.

A properly shaped device flown on a separate spacecraft, can be moved into the line of sight such that it blots out the star. If the occulter (which we now call a starshade) subtends a sufficiently small angle on the sky it can blot out the star without impeding the light from the nearby planet. But this forces the shade onto a separate spacecraft. Even if the shade is only slightly larger than the telescope, it must be flown thousands of kilometers from the telescope in order to appear small enough.

However, diffraction around the starshade and into the telescope can be severe. This forces the starshade to be even larger and farther away. In 1985 Marchal showed that starshades could be designed to suppress the diffraction, but the sizes and distances involved were simply not practical. Copi and Starkman revisited this problem of suppression in 2000 and proposed a practical design that could suppress to the $4x10^{-5}$ level. Unfortunately, the Earth is about 10^{-10} times fainter than the Sun, so no further work was done in developing the concept.

Then Cash (2006) revisited the apodization problem and found a more nearly optimized apodization function that allows one to shrink the starshade substantially so that practical designs could be generated. The new function was the "offset hypergaussian" given by:

$$A(\rho) = 0 \qquad \text{for } \rho < a$$

and

$$A(\rho) = 1 - e^{-\left(\frac{\rho - a}{b}\right)^n} \qquad \text{for } \rho > a \qquad \mathbf{1}$$

In that paper he showed how a practical starshade could be built and flown in pursuit of the goal of finding Earths and searching for life. A great deal more work has transpired in studying these systems. In particular, they are now embodied in a space astronomy mission concept called the New Worlds Observer. The starshade for NWO is designed to be practical and buildable. It nominally has design parameters of a=b=12.5m and n=6, which makes it about 50m across – 62m tip to tip. It flies at a nominal distance (F) of 80,000km, which makes it appear to be 0.062 arcseconds in radius, small enough to allow observation of Earth-like planets at 10pc. It operates in the visible band from 0.3μ to 1μ

wavelength. We will use these baseline parameters throughout the paper when a nominal design is needed.

The search for the solution to the high contrast occulter must be carried out with the full complexity of the Fresnel regime. A Fraunhoffer solution implies that, to good approximation, all the rays impinge upon the mask with the same phase. But an occulting mask fundamentally cannot operate in that manner. A shadow is formed only when the sum of electric fields outside the mask is small, implying a range of phases that sums to zero. But a Fraunhoffer solution would require the mask to be restricted to a single zone and the sum of phases cannot be zero. To achieve a net zero electric field in the focal plane, the integral must extend out of the central zone at least into the first negative Fresnel half zone.

While it is quite remarkable that shadows of such extreme depth can be generated across just a few zones, that fact alone is not enough to justify their choice for use in the pursuit of exoplanets. We must first understand them and be certain that we can build and use starshades in a practical and affordable manner. Unfortunately there is no long history of use that has created a body of generally accepted knowledge and we must start our analysis anew.

There are two aspects to the modeling that are necessary for full understanding. First, we must try to model the shadows analytically. Direct use of the equations of diffraction as applied to the apodization functions can give us basic insight into the performance of the shades. Simple scaling laws and an understanding of the linkages between parameters can best be understood from such results.

Secondly, we need detailed computer modeling. Just as raytracing is necessary for full understanding of the behavior and tolerancing of complicated geometrical optics systems, so too is the full-up computer modeling necessary to design of starshades. In this paper we address both these needs.

II. Analytic Analysis of the Problem

A. Helmholtz-Kirchoff formulation

The mathematical formulation of the Huygens-Fresnel principle can be found in most general optics textbooks (e.g. Hecht[1]). The law states that the electric field at some focal plane, a distance r from a plane aperture, illuminated by a uniform plane wave from infinity is given by:

$$E = \frac{E_0}{i\lambda r}\iint A e^{ikr}\, dS \qquad \mathbf{2}$$

where the integration is over the surface S. E_0 is the strength of the electric field of the radiation incident from infinity onto the surface and r is the distance from each point on the surface to the point in the focal plane that is being evaluated. k is the usual $2\pi/\lambda$ and A is the apodization function on the occulter plane.

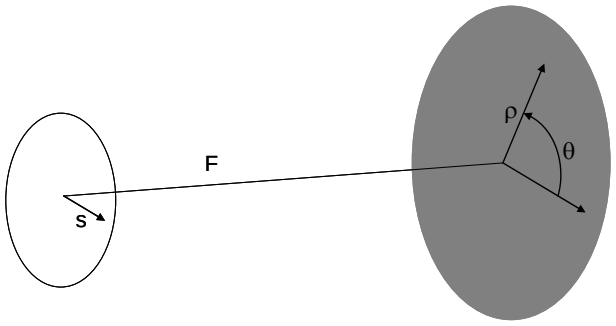

Figure 2: The coordinates of the system are shown. The shade is to the right and its plane is described by **ρ** and **θ.** The telescope is stationed in the plane to the left. We define the distance off axis as **s**.

Figure 2 defines our coordinate system. F is the distance from mask to focal plane. ρ is the radius on the mask, and θ its angle. s is the distance off axis on the focal plane. Then, following the usual Fresnel approximation for large F

$$E = \frac{E_0 e^{ikF} e^{\frac{iks^2}{2F}}}{i\lambda F}\int_0^\infty e^{\frac{ik\rho^2}{2F}}\rho \int_0^{2\pi} A(\theta,\rho) e^{\frac{ik\rho s\cos\theta}{F}}\, d\theta d\rho \qquad \mathbf{3}$$

In the case of a circularly symmetric apodization we can first integrate over angle, finding

$$E = \frac{E_0 k e^{ikF} e^{\frac{iks^2}{2F}}}{iF}\int_0^\infty e^{\frac{ik\rho^2}{2F}} A(\rho) J_0\left(\frac{k\rho s}{F}\right)\rho d\rho \qquad \mathbf{4}$$

If A(ρ) is unity to some radius a, and zero beyond, and if $ik\rho^2/2F$ is small, then this integral leads to the familiar Airy disk that describes the point spread function of the typical diffraction-limited telescope.

To evaluate the diffraction properties of a mask we must use the Fresnel integral, integrating over the entire area that is open to the sky. Since we are designing a mask that covers only a tiny solid angle around the direction to the star, we would need to perform an integral that sums the wavefronts over the entire sky. This is clearly impractical, so we employ Babinet's principle (Hecht) to ease the mathematics.

Babinet's principle states that:

$$E_0 = E_1 + E_2 \qquad \textbf{5}$$

where E_0 is the electric field of the signal in the focal plane, unimpeded by a mask, E_1 is the field at the focal plane obtained by integrating the Fresnel equations over the shape of the mask as if it were an aperture, and E_2 is the field obtained by integrating over all directions outside the mask.

If we assume our unimpeded wave has amplitude of one and phase of zero at the mask, then

$$E_2 = e^{ikF} - E_1 \qquad \textbf{6}$$

We simply seek a solution to the Fresnel integral over the shape of the mask such that

$$E_1 = e^{ikF} \qquad \textbf{7}$$

We seek a solution in which the electric field integrated over the aperture yields, over some region on the focal plane, the same strength it would have had without an aperture.

B. On-Axis Analysis

For mathematical simplicity we confine ourselves to analysis of the on-axis (s=0) position. When *s* is much smaller than $F/k\rho$ across the mask, the Bessel function term remains close to one and equation 4 simplifies to

$$E = \frac{k}{iF} e^{ikF} \int_0^\infty A(\rho) e^{\frac{ik\rho^2}{2F}} \rho d\rho \qquad \textbf{8}$$

So we seek a solution such that

$$\frac{k}{iF}\int_0^{\infty} A(\rho)e^{\frac{ik\rho^2}{2F}}\rho d\rho = 1 \qquad \textbf{9}$$

because the phase is unimportant to the depth of the shadow and the term e^{ikF} can be safely dropped.

To investigate an apodization function of the form of equation 1 we have once again used the Fresnel integral as in equation 8

$$E = \frac{k}{iF}\int_0^{a} e^{\frac{ik\rho^2}{2F}}\rho d\rho + \frac{k}{iF}\int_a^{\infty} e^{-\frac{(\rho-a)^n}{b^n}+\frac{ik\rho^2}{2F}}\rho d\rho \qquad \textbf{10}$$

To show this, we first perform a change of variable to what turns out to be a set of natural units. Multiplying each distance variable by the same scaling factor gives

$$\alpha = a\sqrt{\frac{k}{F}} \qquad \beta = b\sqrt{\frac{k}{F}} \qquad \tau = \rho\sqrt{\frac{k}{F}} \qquad \textbf{11}$$

So that

$$E = \frac{1}{i}\int_0^{\alpha} e^{\frac{i\tau^2}{2}}\tau d\tau + \frac{1}{i}\int_{\alpha}^{\infty} e^{\frac{i\tau^2}{2}-\left(\frac{\tau-\alpha}{\beta}\right)^n}\tau d\tau \qquad \textbf{12}$$

And

$$E = 1 - e^{\frac{i\alpha^2}{2}} + \frac{1}{i}\int_{\alpha}^{\infty} e^{\frac{i\tau^2}{2}-\left(\frac{\tau-\alpha}{\beta}\right)^n}\tau d\tau \qquad \textbf{13}$$

The next step is a change of variable to

$$x = \frac{\tau-\alpha}{\beta} \qquad \textbf{14}$$

so that

$$E = 1 - e^{\frac{i\alpha^2}{2}} - i\beta\int_0^{\infty} e^{-x^n} e^{\frac{i}{2}(\beta x+\alpha)^2}(\beta x+\alpha)dx \qquad \textbf{15}$$

Integration by parts then gives us

$$E = 1 - e^{\frac{i\alpha^2}{2}} - e^{-x^n} e^{\frac{i}{2}(\beta x+\alpha)^2}\Big|_0^\infty - n\int_0^\infty e^{\frac{i}{2}(\beta x+\alpha)^2} e^{-x^n} x^{n-1} dx \qquad \textbf{16}$$

Or

$$E = 1 - n\int_0^\infty e^{\frac{i}{2}(\beta x+\alpha)^2} e^{-x^n} x^{n-1} dx \qquad \textbf{17}$$

Therefore, equation 9 is satisfied except for a remainder term R. Returning to the coordinates of equation 13 we have

$$R = n\int_\alpha^\infty e^{\frac{i\tau^2}{2}} e^{-\left(\frac{\tau-\alpha}{\beta}\right)^n} \left(\frac{\tau-\alpha}{\beta}\right)^{n-1} d\tau \qquad \textbf{18}$$

To evaluate this integral we once again integrate by parts:

$$R = e^{\frac{i\rho^2}{2}} e^{-\left(\frac{\tau-\alpha}{\beta}\right)^n} \left(\frac{\tau-\alpha}{\beta}\right)^{n-1} \left(\frac{1}{i\tau}\right)\Big|_\alpha^\infty + \int_\alpha^\infty e^{\frac{i\tau^2}{2}} e^{-\left(\frac{\tau-\alpha}{\beta}\right)^n} f(\tau)\, d\tau \qquad \textbf{19}$$

where

$$f(\tau) = n\left(\frac{\tau-\alpha}{\beta}\right)^{2n-2}\left(\frac{1}{i\tau}\right) - \frac{n}{i\tau^2}\left(\frac{\tau-\alpha}{\beta}\right)^{n-1} + \frac{n(n-1)}{i\tau}\left(\frac{\tau-\alpha}{\beta}\right)^{n-2} \qquad \textbf{20}$$

The first term of equation 19 is identically zero when evaluated from α to ∞, as will be any term that contains both the exponential and a term of positive power in $(\tau-\alpha)/\beta$. Equation 20 has three terms, each of which must be integrated in the second term of equation 19. The first term of equation 20 has a higher power in $(\tau-\alpha)/\beta$ and as such will be a smaller term than the rest of R. The second term is similarly related to R itself, but is smaller by a factor of n/τ^2. Thus, if $\beta^2 >> n$ the third term will dominate. If β^2 is not larger than *n* then the transmission rises so quickly near $\rho=\alpha+\beta$ that the shade will start to resemble a disk, and Arago's Spot will re-emerge.

We proceed to integrate by parts and taking the dominant term until we finally reach a term that does not evaluate to zero, and we find

$$R = \frac{n!}{\beta^n} \int_{\alpha}^{\infty} e^{\frac{i\tau^2}{2}} e^{-\left(\frac{\tau-\alpha}{\beta}\right)^n} \tau^{1-n} d\tau \qquad \textbf{21}$$

To approximate the value we consider that cosine terms vary rapidly and will integrate to a net of zero at some point in the first half cycle. That cycle will have a length of no more than $1/\alpha$. During this half cycle the second exponential term remains near one and the term in powers of τ will never exceed $\alpha(1\text{-}n)$. So we can expect that

$$R \le \frac{n!}{\beta^n} \frac{1}{\alpha} \left(\frac{1}{\alpha}\right)^{n-1} = \frac{n!}{\alpha^n \beta^n} \qquad \textbf{22}$$

which tells us the accuracy to which the electric field can be suppressed. The square of R is approximately the contrast ratio to be expected in the deep shadow. There were many approximations made to achieve this result and they are only valid in certain parts of parameter space. A large number of small terms were dropped in the repeated integration by parts, which raises a concern as to the accuracy of equation 22. The validity of this formulation has been checked computationally and found to be reasonable when $\beta^2 >> n$.

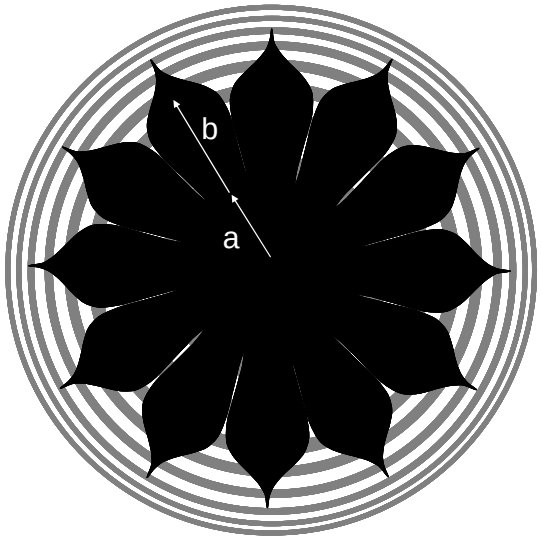

Figure 3: A twelve petal version of the starshade is shown with Fresnel zones in the background.

Again, we see that the optimally sized occulter will have α approximately equal to β. Also, to achieve high contrast, α^n must be quite large. This is clearly easier to achieve as *n* increases, explaining why the higher order curves give more compact solutions, just a few half zones wide. If *n* gets too high, there are diminishing returns as *n!* rises and β approaches unity. Powers as high as *n*=10 or 12 can be practical.

III.Two-Dimensional Computer Modeling

The most obvious approach to the problem of computer computation is simply to evaluate the Fresnel integral (equation 10) directly at each point in the shadow. Unfortunately, a very, very large number of points must be evaluated before the accuracy of the net integral is sufficiently good and the direct approach becomes impractically slow. Alternative, faster approaches are required.

At least three such codes have been developed by members of the New Worlds team, the edge integral approach I discuss here, a code that performs a Fourier propagation of the Fresnel diffraction (Glassman, 2009) and a Henckel Transform (Vanderbei, 2007).

What we desired is an approach that is physically oriented. Particularly for tolerance simulations, it is important to have a code where a small deviation can be added or subtracted on its own, without being convolved with the rest of the system. We found such an approach by making use of the fundamentally binary nature of the starshades. All parts of the starshade must be either fully opaque or fully transmitting. Errors are thus related to errors in the projected shape as defined by the outline of the occulter. By Babinet's Principle this is mathematically equivalent to calculating the diffraction over a clear aperture with opaque surroundings.

We sought a solution which would operate in a manner similar to a Green's Theorem, in which a surface integral can be converted to a line integral around the edge. Dubra and Ferrari (1999) published a paper entitled "Diffracted field by an arbitrary aperture" in which they integrated the Kirchoff formulation of diffraction theory by means of a Green's function approach and converted the two-dimensional integral to a one-dimensional parametric integral. We follow their approach but concentrate on the simpler case of a plane wavefront.

In the case of a binary optic, the apodization is everywhere unity across the aperture, so that equation 3 becomes

$$E = \frac{E_0 e^{ikF} e^{\frac{iks^2}{2F}}}{i\lambda F} \iint_S e^{\frac{ik\rho s\cos\theta}{F}} e^{\frac{ik\rho^2}{2F}} d\theta d\rho \qquad \textbf{23}$$

where *S* represents the surface of the aperture. But S is a completely general surface, and, specifically, there is no requirement that surface be centered or symmetrical about the origin. So, if our source is at infinity, we can calculate an off-axis point by moving the aperture off center. That allows us to set *s* to 0 for any point in the focal plane, by shifting the aperture of integration.

So, setting E_0 to unity, we have

$$E = \frac{e^{ikF}}{i\lambda F}\iint_S e^{\frac{ik\rho^2}{2F}} d\theta\rho d\rho \qquad \textbf{24}$$

and, noting that we can integrate over ρ in closed form, we have

$$E = \frac{1}{2\pi}\int_0^{2\pi} e^{\frac{ik\rho^2}{2F}} d\theta \qquad \textbf{25}$$

evaluated from the inner radius ρ_i to the outer radius ρ_o at that value of θ.

In the case where the area does not include the origin, and is simple, in that any radial line cuts the surface twice, we have

$$E = \frac{1}{2\pi}\int_0^{2\pi} e^{\frac{ik\rho_o^2}{2F}} d\theta - \frac{1}{2\pi}\int_0^{2\pi} e^{\frac{ik\rho_i^2}{2F}} d\theta \qquad \textbf{26}$$

In the case where the area is simple, and the origin is inside, then each radial line cuts the perimeter once at ρ_o and ρ_i is every where 0, so

$$E = \frac{1}{2\pi}\int_0^{2\pi} e^{\frac{ik\rho_o^2}{2F}} d\theta - 1 \qquad \textbf{27}$$

In equation 26 we recognize that the first term is the line integral along the far edge of the area, while the second term is the return on the near side. Thus the integral can be turned into a line integral around the edge of the shape. So, in the case of a simple, convex shape that excludes the origin (ρ=0) within, the equation becomes

$$E = \frac{1}{2\pi}\int_s e^{\frac{ik\rho^2}{2F}} \frac{\hat{\rho}\cdot d\vec{s}}{\rho} \qquad \textbf{28}$$

where $\hat{\rho}$ is the unit vector in the radial direction and $d\vec{s}$ is in the direction of the normal to the edge element and has size equal to length of the edge element. So one merely breaks the edge into small elements and sums the phase factor around the edge.

In the case where the shape is simple, but includes the origin inside, we have

$$E = \frac{1}{2\pi}\int_s e^{\frac{ik\rho^2}{2F}} \frac{\hat{\rho}\cdot d\vec{s}}{\rho} - 1 \qquad \textbf{29}$$

From an algorithmic point of view, we now have a simple prescription for the electric field at the origin. Create a set of points that outline the starshade. At each point calculate the distance between the adjacent points and create the vector ds, which is the vector normal to the surface at that point, with a value equal to the length of the edge element. For each element create the dot product of the normal and the unit vector from the center. Divide by distance from the center and multiply by the Fresnel phase term. Sum this all the way around the edge, and the result will be desired value in the center. To find a point off axis, shift the shape terms and recalculate.

It should be noted that this works well for non-simple forms as well. A complex shape may be broken into simple shapes and each shape integrated separately. The borders between the simple shapes are integrated in one direction for one shape and in the other direction for the adjacent shape, so the net along the border is zero. In practice this means that one can follow the algorithm described in the preceding paragraph around the edge of any, arbitrary shape. Holes may be calculated inside a mask by integrating the edge in the opposite direction. Of course, one must still calculate whether or not the origin falls inside or outside the shape. If found to be inside, then one must subtract the one.

We have built such a code and it works very effectively, and very quickly. It typically takes 0.1 seconds on today's laptops to calculate a single point in the shadow. About 40,000 points are needed around the edge of a starshade to gain sufficient accuracy to predict the residual field to the 10^{-12} level. At the start of algorithm we define the

starshade through four vectors. These are the x and y values of the points around the edge and the x and y values of the normal vectors.

The trickiest part of the algorithm is finding a way to accurately check whether or not the origin is inside the shape. This is difficult near the edges where there is a mathematical discontinuity, and an incorrect value of inside/outside can lead to value near unity, when the true value may be very different. It is even more difficult near corners and tips on the shade. The vectors must be built with care there to ensure that small, round-off errors do not create an incorrect value for inside/outside.

The code is versatile because it mimics reality rather closely. A small deviation from the nominal value of the edge in reality is reflected directly in the sum of the electric field. The code sums the local behaviors to create a single global value at a point. This makes the code ideal for modeling tolerances and other real effects. All the computer modeled results in this paper have been generated using this code. The results have been carefully cross-checked with another code that will be reported upon elsewhere (Glassman et al, 2009)

IV. Tolerancing

So far, we have treated the starshade concept as a mathematical construct, without regard to whether it has any practical application. If it is ever to be built, then the tolerances for fabrication must be investigated. Any device in which the tolerances are impractically tight would be of little value. Since the starshade concept is insensitive to wavelength and to rearrangement into petals, the presumption is that the tolerances will not be particularly difficult to achieve.

A. Alignment

Lateral Position: For this we mean the position of the detector in the x-y direction relative to the line that extends from the source through the centre of the starshade. If the telescope drifts too far laterally it will start to leave the shadow. This distance is set by the size of the shadow. The depth of the shadow increases as one approaches the center, and the telescope must be smaller than the diameter of the region with sufficient contrast. This region becomes larger as the shade becomes larger and more distant. Thus, an optimized starshade would fit the shadow size to the telescope size. So, a margin of 20%

on the starshade size appears reasonable. Thus we simply choose ±0.1a as the constraint on lateral position.

Depth of Focus: By this we mean the position of the detector on the z-axis, the line from the star through the centre of the starshade. Because of the insensitivity of the design to scaling by wavelength, it is similarly insensitive to scaling by distance. Equation 22 relates the depth of the shadow to the distance, F, through the dimensionless parameters, α and β. Since each scales as the square root of wavelength times F, the tolerance on F is set by the tolerance on λ. At the long wavelength end, the performance of the starshade degrades rapidly, so the design actually starts with the long wavelength constraint. Assuming that a ten percent degradation in wavelength is acceptable, so is a 10% change in distance. Since a typical design places the starshade at 50,000km, the depth of focus is effectively 5000km, rather easy to implement.

Rotational: Because of the circular symmetry built into the design, there is no constraint on θ_z, the rotation angle about the line of sight. Sometimes it might be better to actually spin the starshade about this axis to smooth out residual diffraction effects.

Pitch and Yaw: Because of the rotational symmetry the constraint on errors in alignment about the pitch axis, θ_x and yaw axis, θ_y, may be combined into a single pointing error. It turns out that the design is highly forgiving of such errors, but the proof takes some calculation.

We assume that the shade is out of alignment with the axis of symmetry by an angle φ about the y-axis, such that the shade appears foreshortened in the x direction by a factor of $\cos\varphi$, which we shall approximate by $1-\varepsilon$. The net optical path difference is small, about $(a+b)\theta\varphi^2/2$ for small θ and φ. As long as φ is $<<1$ the net path delay is a small fraction of a wavelength and may be ignored.

We start by rewriting equation 8 for the on-axis (s=0) case in Cartesian coordinates with the integration now taking place over the projected area which is foreshortened in one dimension

$$E = \frac{k}{2\pi iF} e^{ikF} \left[\begin{array}{l} \int e^{\frac{ikx^2}{2F}} \int e^{\frac{iky^2}{2F}} dxdy + \\ \\ \int e^{\frac{ikx^2}{2F}} \int e^{\frac{iky^2}{2F}} e^{-\left(\frac{\sqrt{x^2+y^2}-a}{b} \right)^n} dxdy \end{array} \right] \quad \textbf{30}$$

By a change of coordinate to z=x/(1-ε) we have

$$E = \frac{k}{2\pi iF} e^{ikF} \left[\begin{array}{l} (1-\varepsilon) \int e^{\frac{iky^2}{2F}} \int e^{\frac{ikz^2(1-\varepsilon)^2}{2F}} dydz + \\ \\ (1-\varepsilon) \int e^{\frac{iky^2}{2F}} \int e^{\frac{ikz^2(1-\varepsilon)^2}{2F}} e^{-\left(\frac{\sqrt{y^2+z^2(1-\varepsilon)^2}-a}{b} \right)^n} dydz \end{array} \right] \quad \textbf{31}$$

where the integration is now over a circularly symmetric shape as before. Converting to polar coordinates we find

$$E = \frac{k}{2\pi iF} e^{ikF} \left[\begin{array}{l} (1-\varepsilon) \int_0^{2\pi} \int_0^{a} e^{\frac{ik\rho^2}{2F}} e^{-\frac{ik\rho^2\cos^2\theta(2\varepsilon-\varepsilon^2)}{2F}} \rho d\rho d\theta + \\ \\ (1-\varepsilon) \int_0^{2\pi} \int_a^{\infty} e^{\frac{ik\rho^2}{2F}} e^{-\frac{ik\rho^2\cos^2\theta(2\varepsilon-\varepsilon^2)}{2F}} e^{-\left(\frac{\sqrt{\rho^2-\rho^2\cos^2\theta(2\varepsilon-\varepsilon^2)}-a}{b} \right)^n} \rho d\rho d\theta \end{array} \right] \quad \textbf{32}$$

Converting to polar coordinates, expanding and ignoring terms in ε^2 and higher, then differencing from the unperturbed integral we have an expression for the remainder caused by the misalignment:

$$\begin{array}{l} R = \frac{k}{2\pi iF} \int_0^{2\pi} \int_0^{a} e^{\frac{ik\rho^2}{2F}} \left[1-(1-\varepsilon) e^{\frac{ik2\varepsilon\rho^2\cos^2\theta}{2F}} \right] \rho d\rho d\theta \\ + \frac{k}{2\pi iF} \int_0^{2\pi} \int_a^{\infty} e^{\frac{ik\rho^2}{2F}} e^{-\left(\frac{\rho-a}{b} \right)^n} \left[1-(1-\varepsilon) e^{\frac{ik2\varepsilon\rho^2\cos^2\theta}{2F}} e^{-\frac{2n\varepsilon\rho^2\cos^2\theta}{b\rho}\left(\frac{\rho-a}{b} \right)^{n-1}} \right] \rho d\rho d\theta \end{array} \quad \textbf{33}$$

Approximation of the exponentials in the brackets and dropping higher order terms reduces this to:

$$R = \frac{k^2\varepsilon}{2F^2}\left[\int_0^a e^{\frac{ik\rho^2}{2F}}\rho^3 d\rho + \int_a^\infty e^{\frac{ik\rho^2}{2F}} e^{-\left(\frac{\rho-a}{b}\right)^n}\rho^3 d\rho\right]$$

$$-\frac{nk\varepsilon}{Fb}\int_a^\infty e^{\frac{ik\rho^2}{2F}} e^{-\left(\frac{\rho-a}{b}\right)^n}\rho^2\left(\frac{\rho-a}{b}\right)^{n-1} d\rho \qquad \textbf{34}$$

To evaluate this we use our usual change of variable:

$$\alpha = a\sqrt{\frac{k}{F}} \qquad \beta = b\sqrt{\frac{k}{F}} \qquad x = \rho\sqrt{\frac{k}{F}} \qquad x = y\beta + \alpha \qquad \textbf{35}$$

and integrate by parts. The higher order terms cancel as before, leaving us with an expression for the remainder

$$R = n\varepsilon\int_0^\infty e^{\frac{i(\beta y+\alpha)^2}{2}} e^{-y^n} y^{n-1} dy \qquad \textbf{36}$$

which is a form similar to that encountered in the original integral over the unperturbed aperture. We may therefore conclude that, to first order,

$$R = \varepsilon R_{cs} \qquad \textbf{37}$$

where R_{cs} is the remaining electric field in the original circularly symmetric case. We conclude that misalignments of axis have almost no effect. They create a scale change in one axis that has no significant effect. Many degrees of misalignment can be tolerated, but in a practical mission it is likely that control issues will dictate pointing to a few arcminutes anyway.

B. Tips and Valleys

Truncation of Petals: Mathematically, the apodization carries out to infinity. In the case of a binary mask, this means that petals extend to infinity, something which clearly cannot be done in practice. At what radius is it safe to truncate the petal? We can write the remainder of the electric field created by truncating at a radius T.

$$R = \int_T^\infty e^{\frac{ix^2}{2}} e^{-\left(\frac{x-\alpha}{\beta}\right)^n} x dx \qquad \textbf{38}$$

which is definitely less than

$$R = \frac{1}{N} e^{-\left(\frac{T-\alpha}{\beta}\right)^n}$$

39

per petal. The remainder due to truncation can be safely ignored in a typical case when the thickness of each petal has fallen below about 0.1mm. Thus the petals must be sharp at their tips, but do not have to be controlled at a microscopic level.

C. Distortions

Area Change: Finally we consider the case where the shape changes in a discontinuous manner. Since there are many possible classes of such error, we can only address them as a generality. Consider a petal that is missing a chunk along one edge. The missing part can be contained within one half zone or spread over several. To the extent that the missing area is monotonic across the zones, the net effect is less than the largest area within one half zone. So, the size of the missing area must be less than 10^{-5} of the starshade area, but can be substantially larger if spread over several zones.

D. Shape

Azimuthal Errors in Petal Shape: When we gathered the apodization function into the petals to make the function binary, we significantly perturbed the distribution of the electric field in the azimuthal direction. The total, when integrated over the circle at any given value of ρ, remained unchanged. Thus, within the azimuthal sector of width $2\pi/N$ radians at any fixed radius ρ, we are free to move the obscuration around. Essentially, the starshade is insensitive to shear in the azimuthal direction. We must simply keep the shear from slipping into the region of the adjacent petals.

Radial Errors in Petal Shape: If the petal is stretched or compressed such that the smoothness of the fall of the apodization is maintained, then there is little impact on the performance. This is reflected in the insensitivity to alignment, wherein the petals in some directions are changed in projected length, but there is no noticeable impact on performance. Similarly the petal analysis shows that each petal independently creates its own deep shadow zone. Hence, radial scaling of modest amounts does not hurt the performance.

E. Holes

Opacity: The shade must be opaque to the needed level. If the star is to be suppressed to better than a ratio S, then the shade must transmit less than 1/S of the incident radiation

Pinholes: The presence of pinholes can simulate a level of transparency. By the Fresnel integral we see that the area of the pinholes must represent 1/S of the area of the starshade if uniformly distributed. If contained in one zone, they must add up to less than $1/\sqrt{S}$ of the area of that zone.

Large Holes: A single large hole can be restricted to a single zone. Since a zone has an area

$$A_z = \pi\lambda F \qquad \textbf{40}$$

the hole must have an area less than

$$A_{Hole} < \frac{\pi\lambda F}{\sqrt{S}} \qquad \textbf{41}$$

and for typical cases the area of the hole can be as large as a square centimeter, well within a practical range.

References

1. Cash, W. "Detection of Earth-like planets around nearby stars using a petal-shaped occulter", *Nature*, **442**, 51-53 (2006)
2. Copi, C. J., and Starkman, G. D., *Astrophysical Journal*, **532**, 581-592 (2000).
3. Dubra, A., and Ferrari, J., "Diffracted Field by an Arbitrary Aperture", *Am. J. Phys*, **1**, 87-92, (1999)
4. Glassman, T. et al, in preparation, (2009)
5. Hecht, E., Optics, Addison Wesley, 4th Edition (2001).
6. Marchal, C., "Concept of a space telescope able to see the planets and even the satellites around the nearest stars", *Acta Astronautica*, **12**, 195-201 (1985).
7. Spitzer, L., "The Beginnings and Future of Space Astronomy", *American Scientist*, **50**, 473-484 (1962)
8. Vanderbei, R.J., Spergel, D.N., and Kasdin N.J., "Circularly Symmetric Apodization via Star-shaped Masks", *Astrophysical Journal*, **599**, 686-694 (2003).
9. Vanderbei, R., Cady, E., Kasdin, N., "Optimal Occulter Design for Finding Extrasolar Planets", *Astrophysical Journal*, **665**, 794, (2007)

Laboratory Studies of Petal-Shaped Occulters

E. Schindhelm[a], A. Shipley[a], P. Oakley[a], D. Leviton[c], W. Cash[a], G. Card[b]
[a]Center for Astrophysics and Space Astronomy, University of Colorado
[b]High Altitude Observatory, Boulder CO
[c]NASA Goddard Space Flight Center, Greenbelt, MD

ABSTRACT

We present laboratory studies of scaled occulting starshades for the New Worlds Observer (NWO). A deep reactive ion etched silicon starshade has been fabricated by NIST, designed to cover the same number of Fresnel zones as in the proposed mission. The broadband shadow is mapped with a photometer in a dark vacuum tunnel fed by a heliostat at HAO. CCD images provide direct contrast measurements of different features around the starshade. Preliminary measurements reach $5x10^{-6}$ suppression in the center of the shadow at the focal plane. The two-dimensional structure of the starshade diffraction pattern is compared to that produced by the Fresnel integral.

Keywords: New Worlds Observer, TPF-O, extrasolar planets, occulter, coronagraph, high contrast

1. INTRODUCTION

The field of exoplanet study is rapidly expanding, with many new and exciting results published regularly. Indirect methods of studying these extrasolar planetary systems are growing with their correspondant technologies. However, the direct observation of exoplanets is hindered by the difficulty of distinguishing planetary photons from parent starlight. Current proposed methods involve diffracting away parent star photons either inside the telescope, or before light enters the telescope. The New Worlds mission architecture solves the latter problem by utilizing an external occulter, dubbed a 'starshade'. A class of shapes has been found[1] that can efficiently keep less than 10^{-10} of incident stellar photons from entering the telescope. The design currently under consideration consists of 12-24 "petals," so named due to their resemblance to petals of a flower. A proposed design for New Worlds would be a starshade roughly 12.5 meters in radius, flying 50,000 km away from a conventional 4 meter telescope. Simulations produce a contrast better than 10^{-10} for an inner working angle of 40 milliarcseconds. This system also benefits from no outer working angle limitations.

One of the major tall poles in the design and fabrication of such a starshade is our detailed understanding of diffraction tolerancing. How do slight defects in petal shape create distortions of the expected diffraction pattern at the focal plane? How many petals are necessary to sufficiently approximate a circularly symmetric apodization? In this study we have begun to answer these questions by bringing together theory and observation. We have performed a series of tests at the High Altitude Observatory (HAO) vacuum facility at the National Center for Atmospheric Research (NCAR). A heliostat allows the use of the sun as a light source. Scaled starshades have been fabricated with silicon by the National Institute for Standards and Technology (NIST). Hung in the vacuum tank to suppress rayleigh scatter, the starshade casts a shadow that is mapped by a photometer. Thus far we have demonstrated a contrast of $5x10^{-9}$. An efficient algorithm has been developed to calculate the Fresnel integral for an occulting mask. This forms a focal plane image which can be directly compared to data. Section 2 reviews in more detail the occulter shape and the method for calculating the resulting diffraction. The test setup is described in Section 3. In Section 4 we present initial results and discuss contrast and suppression calculations.

2. OCCULTERS FOR STELLAR SUPPRESSION

The starshade is essentially a pupil plane instrument, with the telescope viewing diffracted light in the Fresnel regime as opposed to Fraunhoffer. The starshade and the Fresnel treatment have been presented in detail before, but we briefly discuss the mathematics here. Incident plane waves from the star form spherical "zones" once they interact with the occulter. These zones represent portions of the electric field which are positive and negative; thus two half zones cancel out to zero electric field. A circular disk could, at the right radius and distance from the focal plane, cancel out

Techniques and Instrumentation for Detection of Exoplanets III, edited by Daniel R. Coulter
Proc. of SPIE Vol. 6693, 669305, (2007) · 0277-786X/07/$18 · doi: 10.1117/12.734480

all impingent light at one wavelength. However, at other wavelengths the zones are of a different size, and the electric field does not cancel out. At some wavelengths it can even be amplified. The solution for exoplanet study is to use an apodization that covers the zones such that the starlight cancels out over a broad band across a wide enough space for a telescope, allowing detailed photometry and spectroscopy.

By using Babinet's principle with a class of apodizations studied before as apertures, an occulting apodization was found. The ideal, circularly symmetric apodization A as a function of occulter radius ρ is:

$$A(\rho)=\begin{cases} 0 & for \quad \rho \le a \\ 1-e^{-\left(\frac{\rho-a}{b}\right)^n} & for \quad \rho > a \end{cases} \tag{1}$$

Where a is the radius of the inner disk through which no light is transmitted, and b is the e-folding length of each of the petals. N is an even integer that determines how long the petals are. The apodization can be optimized[2], however for the first experiments we use that of Equation 1. The occulting starshade is binary, manifesting this in the petals which fall off in angular radius according to A(ρ). Our test articles use this shape for its petals with n=6, and a=b=12.5mm.

The major problem for tolerancing is understanding how the valleys and petal tips deviate from this perfect apodization, letting more or less light through in some zones. The electric field at a point P due to an occulting apodization can be calculated using the Fresnel integral:

$$E_P = \frac{E_0}{i\lambda R}\iint A e^{ikR}\, dS \tag{2}$$

Where E_0 is the incident electric field, λ the particular wavelength, k the wavenumber, and R the distance from P to a given area element dS. While a simple equation, trying to calculate the diffraction pattern with this 2D integral is unwieldy for most computers. Using a Green's function treatment[3], the integral can be simplified to an integration over one variable. For an arbitrary aperture, the coordinates for this method are shown in Figure 1 depending upon the position P.

The point P' is the projection of P on the aperture plane, and calculation of the electric field is different based on whether P' is inside or outside the aperture. Cylindrical coordinates are adopted and the electric field is simplified to an integration in φ around the edge of the aperture. For the case in which P' is inside the aperture, R(φ) is a simple function of F and c(φ), the distance between P' and the aperture boundary at a given φ. When P' is outside the aperture, the case is more complicated.

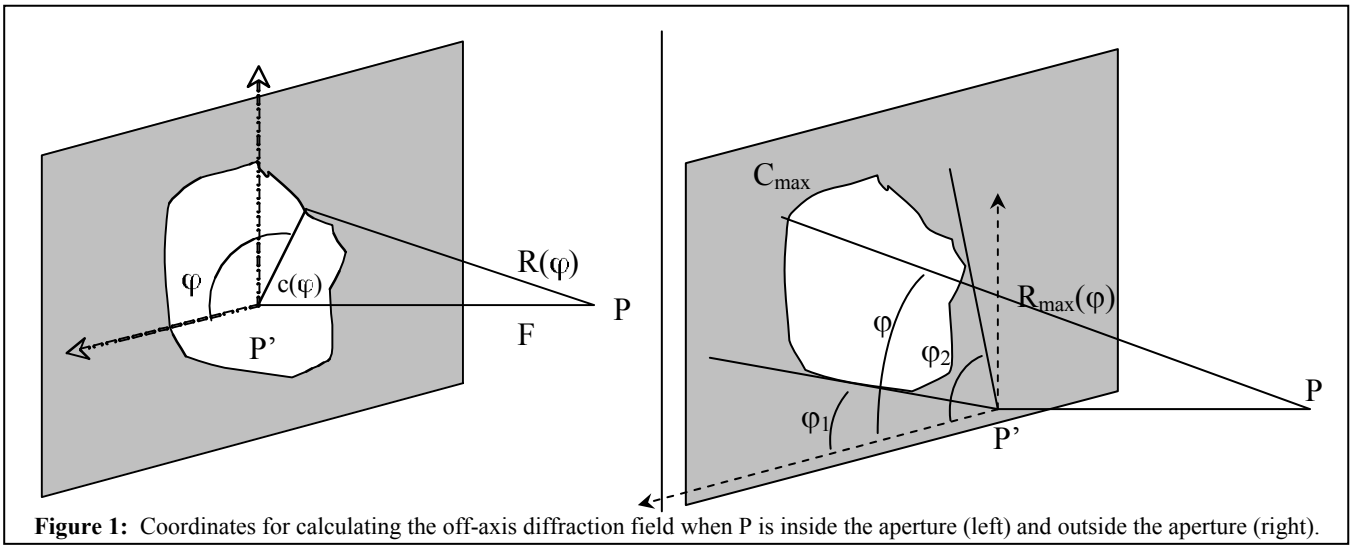

Figure 1: Coordinates for calculating the off-axis diffraction field when P is inside the aperture (left) and outside the aperture (right).

$R_{max}(\varphi)$ runs through the curve C_{max}, which runs between the limit polar angles φ_1 and φ_2. At any point P' there are two angles φ_1 and φ_2 that divide the aperture boundary into C_{max} and C_{min} which are the curves further from and closer to P', respectively. C_{min} and its corresponding R_{min} are not shown in Figure 1 due to cluttering the plot. For the case where P' is inside the aperture, the electric field is

$$E_P = E_0\left[e^{ikF} - \frac{F}{2\pi}\int_0^{2\pi}\frac{e^{ik\sqrt{F^2+c^2(\varphi)}}}{\sqrt{F^2+c^2(\varphi)}}d\varphi\right] \tag{3}$$

Here F is the distance to the focal plane. When P' is outside the aperture, the electric field is

$$E_P = -\frac{E_0 F}{2\pi}\left[\int_{C_{\max}}\frac{e^{ikR_{\max}(\varphi)}}{R_{\max}(\varphi)}d\varphi - \int_{C_{\min}}\frac{e^{ikR_{\min}(\varphi)}}{R_{\min}(\varphi)}d\varphi\right] \tag{4}$$

By application of Babinet's principle, we can integrate or a petal-shaped aperture and subtract from the incident electric field. An example of this code's product is shown in Figure 2 for the proposed New Worlds mission. A starshade ~25 meters in diameter is placed 20,000 km away from the telescope, achieving a suppression of 10^{-15} over the central few meters. This theoretically shows that the mission is feasible, with only zodiacal and exozodiacal light providing noise against which exoplanets must be studied. However in reality, defects in the starshade can deter the achievement of such suppression. In this study we begin to address this issue by looking at the diffraction patterns of scaled starshades at air and vacuum.

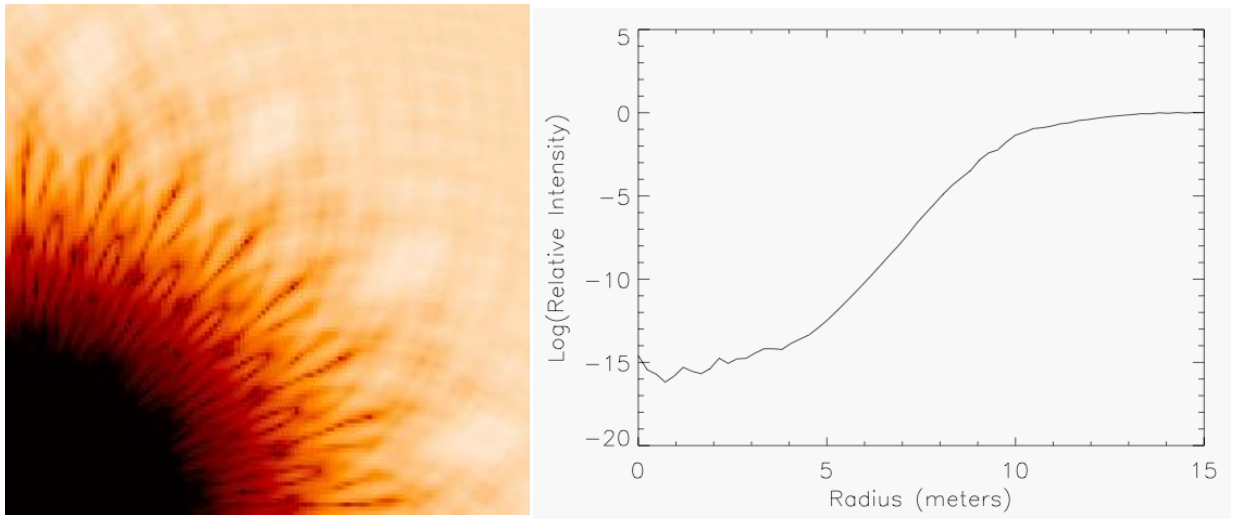

Figure 2: Theoretical 2D pattern of a quadrant of the electric field calculated from Equations 3 & 4 (left), and angle-averaged suppression (right). Starshade parameters are a=b=12.5 meters and F=20,000 km.

3. EXPERIMENT SETUP

For our experiment we use the sun as our light source. The heliostat consists of two large (3'x4') mirrors, a steerable primary and stationary secondary. At the entrance window to the vacuum tank, a pickoff mirror directs some of the sunlight to a series of mirrors, allowing for a long throw to track the beam relative to its position down the tank. This allows us to keep the beam of sunlight centered on the starshade and detector. The vacuum tank itself is approximately 100 feet from the entrance chamber to the instrument chamber, and 4 feet in diameter. The inside of the tank is painted black, and baffles are placed every ~18 feet to control scatter.

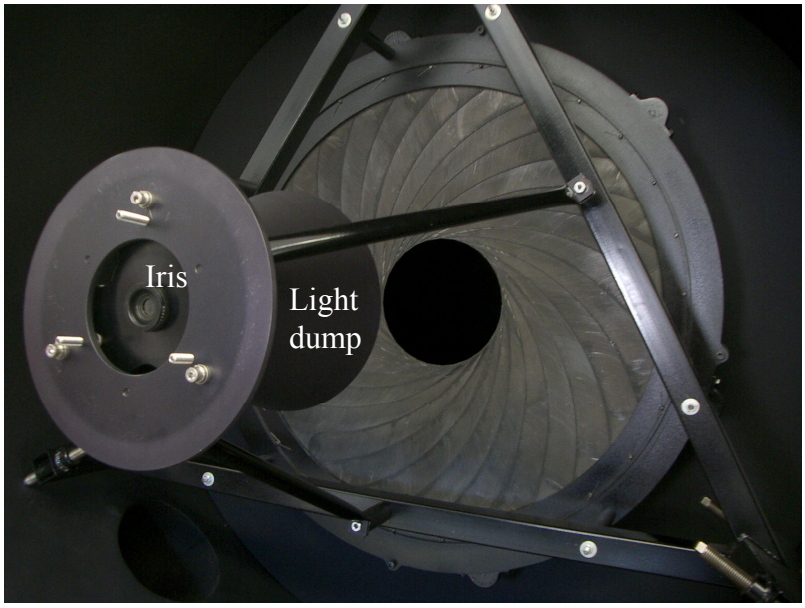

Figure 3: The entrance iris fixture. Sunlight enters from the left.

The entrance chamber is shown in Figure 3 with the front flange removed. A truss holds the iris fixture close to the window to keep light from scattering around the iris. In addition the entrance window is covered mostly in cinefoil to the same end. The iris is opened to a one millimeter diameter so as to let an appropriate amount of light through. A light dump is attached to the front side of the fixture. It is made of welded aluminum cones and has undergone a Deep Space Black process. This makes the light dump absorb and disperse light more uniformly, controlling light which bounces off the entrance side of the starshade. This technique keeps the iris fixture from being illuminated and seen by our detectors. A larger iris is positioned after the light dump for additional scatter control.

The occulter is placed ~60 feet down the tank from the iris so as to cover the same number of fresnel zones as would be covered in the actual proposed mission. A full scale starshade of a=b=12.5 meters flying 2 x10^7 meters away from the telescope corresponds, in this experiment, to an occulter with a=b=8 mm placed ~12 meters from the detector.

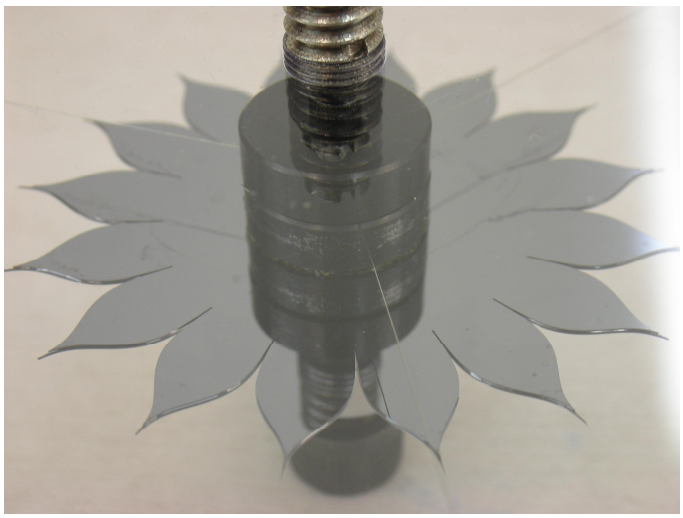
Figure 4: Mounted silicon starshade with 16 petals. Puck is taped to the back of the starshade, and held in its mounting ring by wires.

The test articles were photo-etched out of silicon to a tolerance of ~5 microns. Starshades had thicknesses of 100 and 200 microns, and were made with either 12 or 16 petals. A mounting puck was fixed to the non-reflective side of the occulter, and wire 3 mil in diameter was used to hang it from a mounting ring 17 inches in diameter. This mounting ring was fixed in the middle of the vacuum tank with tripod poles for stability. An example starshade is shown in Figure 4, mounted in its ring. A set screw holds the puck down against a Teflon post for stability during transportation and mounting to the tank.

A block diagram of the detector end is shown in Figure 5, first developed by Leviton et. al[4]. We used two types of detectors in this experiment, the first being a photomultiplier tube (PMT) run by a high volts power supply and connected to a discriminating pulse conditioner to

reject events that do not originate from the photocathode. A frequency counter then relays the number of counts to our computer through a GPIB interface. A photometer is set at the entrance end of the tank to roughly measure the intensity of the incoming sunlight, providing a normalization. The PMT allows for high signal to noise mapping of the electric field intensity. We also use a CCD,

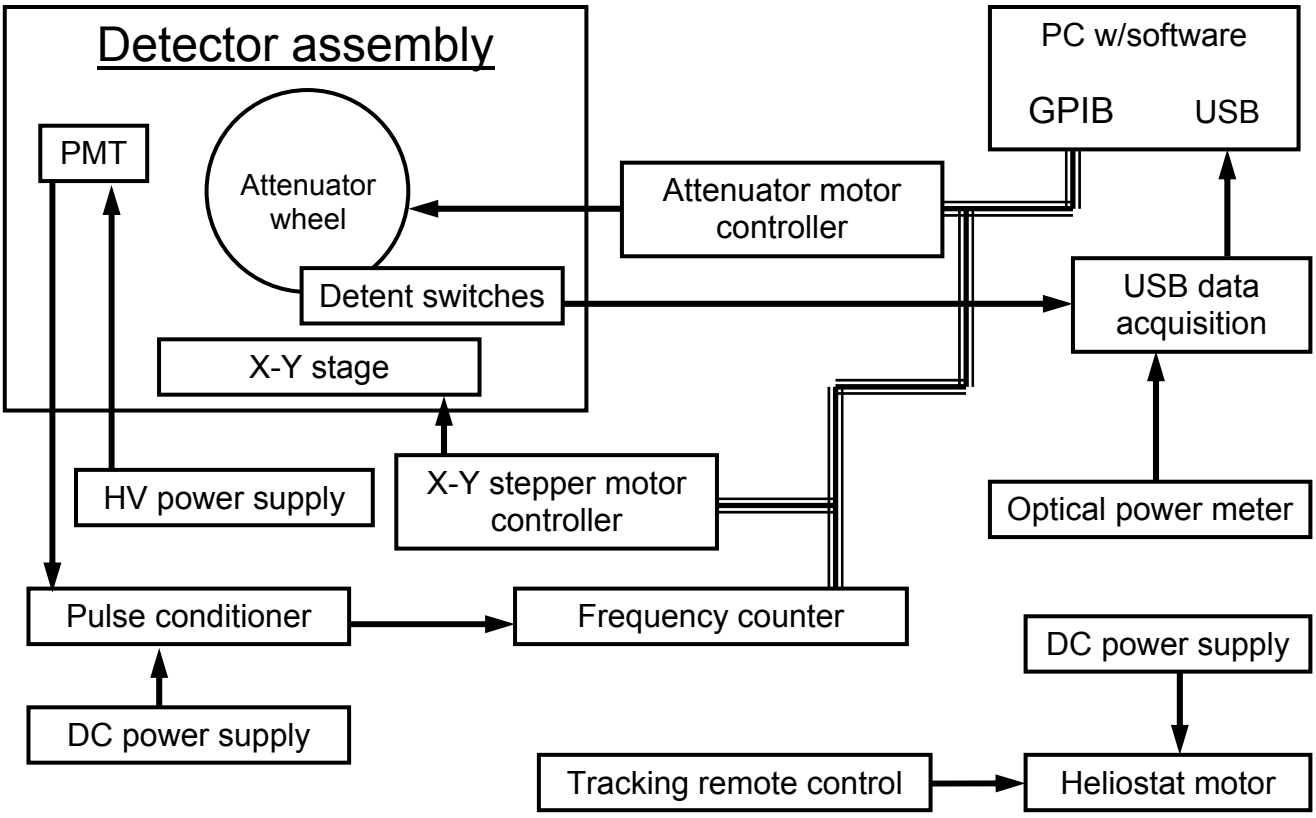

Figure 5: Block diagram for the detector end of the experiment.

allowing us to form an image and identify sources of light around the starshade. Both the PMT and CCD attach separately to the back of our detector mount, which has XY stages for mapping the focal plane and testing off-axis response. The detector mount is shown in Figure 6. In addition, a filter wheel on the front end contains neutral density filters that allow high contrast measurements. Detent switches communicate with the computer as to which filter is placed in front of the detector. A light dump cone, also Deep Sky Blackened, attaches to the front of the detector mount that serves two purposes. First, it keeps the beam, which is 10 inches in diameter at the detector end, from reflecting back on the baffles or starshade to be seen by the detector. Second, the aluminum cone at the front of the light dump, together with an iris in front of the filter

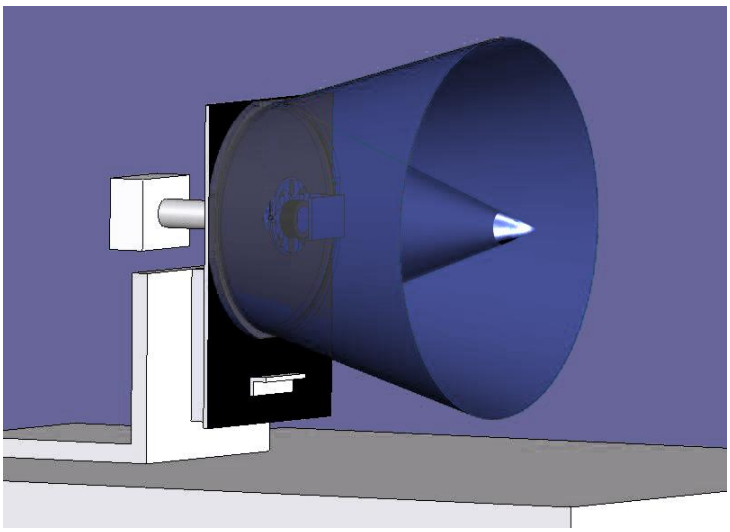

Figure 6: SolidWorks model of detector mount. The light dump cone points towards the light source and starshade. The PMT and CCD attach to the back end.

wheel, allow in only light originating from around the starshade. This ensures that scattered light entering the detectors is kept to a minimum.

4. PRELIMINARY TEST RESULTS

4.1. Photometer Data

The photometer program moves the PMT in an outward spiral starting from the on-axis position with the starshade. Since the diffraction pattern is darkest in the center, the filter wheel begins without a neutral density filter in front of the PMT. As the PMT scans to brighter regions, the program selects a darker neutral density filter appropriate to keep signal to noise (~20) at a sufficient level, but not so high as to saturate the detector. Figure 7 shows the PMT data

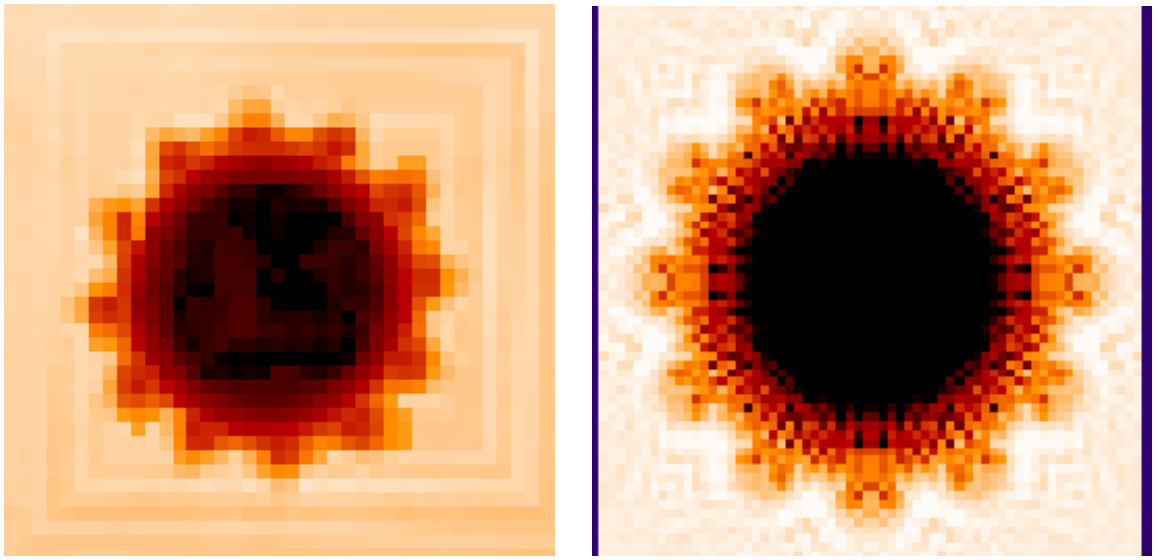

Figure 7: 2D plot of PMT-measured data (left) and calculated diffraction pattern (right) for the 12 petal starshade.

compared to the theoretical prediction. At low contrast levels along the outer edge, (10^{-1} – 10^{-4}) there is good agreement between the two. The 12 lobe structures correspond to the 12 petals, and the sharp drop off to higher contrast is seen as well. The floor of our data does not match that predicted by our code. The angle-averaged intensity is plotted as a function of radius in the focal plane for both the PMT data and the calculated diffraction pattern. The use of equations 3 and 4 had to be modified slightly due to the fact that our experiment uses light that is not effectively a point source at infinity. This merely changes the focal length F of the system to the inverse addition of the distance between the starshade and the source and detector.

4.2. CCD Images

Using the CCD attached to our detector mount shows where light originates on the starshade, raising the achievable contrast level. The peak response of the CCD is around 600-700 nm, which is slightly different than the PMT response. Thus the neutral density filters had to be re-calibrated in order to make appropriate contrast measurements. Several starshades were tested to find the best fabricated. NIST fabricated two 100 micron thick starshades with 12 and 16 petals, and two 200 micron thick starhades with 12 petals each. The 16 petal 100 micron thick and one of the 12 petal 200 micron thick starshades were of sufficient quality and compared for contrast measurements. In addition, a planet simulator was used to see what contrast level could be detected by our setup. This consisted of a flashlight positioned next to the entrance light dump cone approximately an inch and a half from the center of the starshade. A 3-micron pinhole was placed over the flashlight to simulate a planet 10^{-9} of the incoming sunlight.

For contrast measurements, a high neutral density filter was placed in front of the CCD and an off-axis image of the entrance iris was taken with a short exposure time. This was compared with a long, open exposure at the on-axis position. These images are shown in Figure 8 for the best test article, the 200 micron thick starshade. The main noticeable feature is a ring of 12 points of light corresponding in position to the bases of the petals. In addition there are three bright spots 120 degrees apart corresponding to where the wires intersect with the petals. Other bright points are believed to be dust sticking to the wires or starshade.

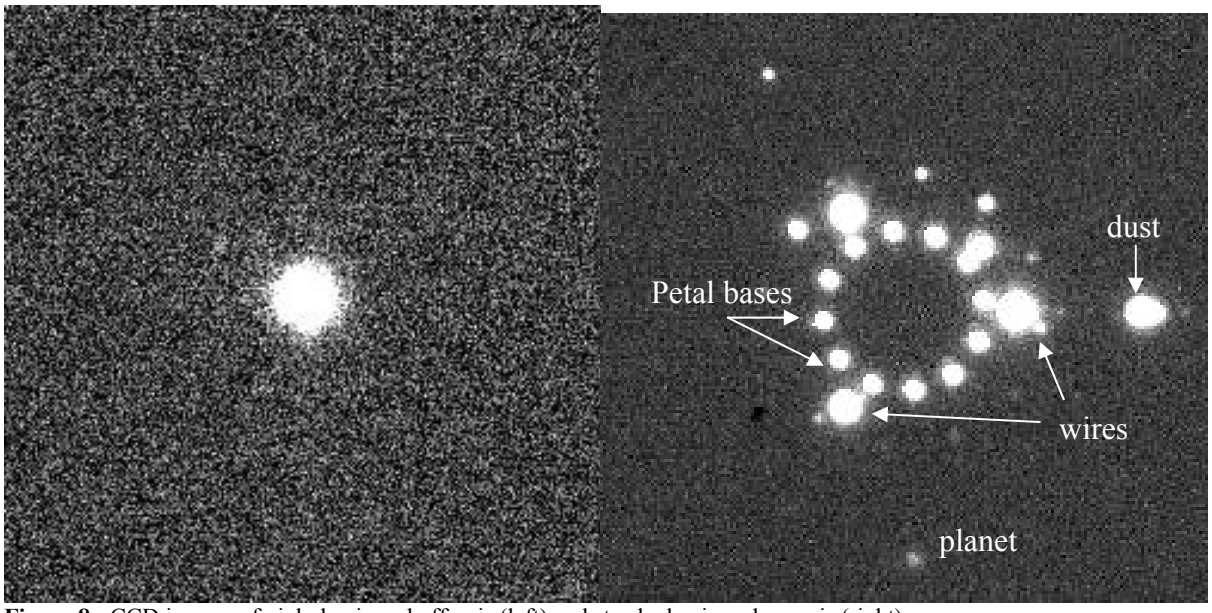

Figure 8: CCD images of pinhole viewed off-axis (left) and starshade viewed on-axis (right).

By directly comparing the light from these spots to the light from the iris we can determine what are the major contributors to the lower contrast achieved. The points of light from the wires are each $2x10^{-7}$, as is the entire ring of petal base lights. The remaining points of light, plus diffuse scatter, must make up the remaining light that contributes to the contamination shown in Figure 8. The planet is at a contrast of $5x10^{-9}$, detected at twice the level of the background. The 16 petal starshade exhibits spots with far less intensity of those from the 200 micron 12 petal starshade. It was photolithographed from both sides, yielding a thinner edge along each petal. It is for this reason we believe that the intense light at the petal bases and wire intersections are due to the large finite thickness of the starshades relative to their area. Light is reflecting off the petal-base edges and into the focal plane. It is also possible that the petal bases are not manufactured close enough to spec to create the correct diffraction pattern. Our code is currently not setup to predict such features, but we are investigating this. In addition, we will obtain microscope data of the profile of the starshades to correlate with theory.

5. SUMMARY

We have conducted preliminary tests at air and vacuum of deep reactive ion etched silicon starshades illuminated by a broadband source. The results show good basic agreement with theory. We believe the difference between the CCD images and the theoretical suppression patterns is due to the different finite thickness of the test articles compared to the wavelengths considered. Scattered light raises the achievable contrast to the $5x10^{-6}$ level at the center of the focal plane shadow. Efforts are under way to further reduce scatter in the tank, and understand potential errors in the manufacturing process.

ACKNOWLEDGEMENTS

We would like to thank Mike Kaiser, Sarah Levine, and Thomas Rogers for their contributions to the experiment. In addition we thank Jim Beall from NIST for fabricating the starshades.

REFERENCES

1. Cash, W., "Detection of Earth-like planets around nearby stars using a petal-shaped occulter," Nature, **442**, 51-53, 2006.
2. Vanderbei, R.J., Kasdin, N.J., Cady, E., "Optimal Occulter Design for Finding Extrasolar Planets," arXiv:0704.3488
3. Dubra, A., Ferrari, J., "Diffracted field by an arbitrary aperture," Am. J. Phys., 67, 1, 1999
4. Leviton et al., these proceedings.

NWO NGAS Testbed Report

Rocco Samuele, Rupal Varshneya, Tiffany Glassman, Ann Shipley*, Amy Lo, Kelley Chilcott, Chuck Lillie
*University of Colorado, Boulder, CO

Northrop Grumman Aerospace Systems (NGAS) operates an NWO testbed located at Northrop Grumman's Space Park Campus in Redondo Beach, California. It is an ongoing experimental effort to evaluate starshade performance. It is also our goal to develop an error budget and test starshade resilience to shape deformities, observational misalignments, and band pass sensitivity.

The testbed was designed to mimic the Fresnel number of the mission configuration and can be rearranged to vary starshade and detector separations, which is useful when testing various starshade diameters and evaluating a variety of Inner Working Angles (IWAs). The testbed uses a 42 m long, mechanically constrained vacuum chamber, which also acts as a light baffle. The source is a visible band, halogen lamp mounted into an integrating sphere, focused through a pinhole, and then collimated. The beam propagates to the starshade and then to a CCD ~40 meters downstream in the shadow of the starshade. An iris simulates the entrance aperture of a space telescope and then a lens focuses the residual light onto the CCD.

It is important to note that the IWA of the starshade cannot be preserved while maintaining the system Fresnel number, without scaling the wavelength down into the x-ray range. For the testbed, evaluating starshade performance in the visible band was a priority, thus maintaining the same IWA had to be sacrificed. Therefore, locations in the testbed contrast images will be scaled to the IWA of the full-scale system.

Currently, we are testing a 40mm effective diameter, silicon etched starshade, fabricated by the NGAS foundry. The figure below shows a face-on view of the 12 petal test starshade.

Silicon etched, 40mm effective diameter starshade.

Shadow-plane images, when a lens is not used to focus the shadow onto the CCD, not only reveal light suppression, but also help to verify that our simulations do, in fact, mimic the actual diffraction patterns established by the starshade. The following figure shows a mosaic of shadow-plane images (left) juxtaposed with a simulated diffraction image of a similar starshade shape. There is clearly strong correspondence between the Fresnel diffraction patterns.

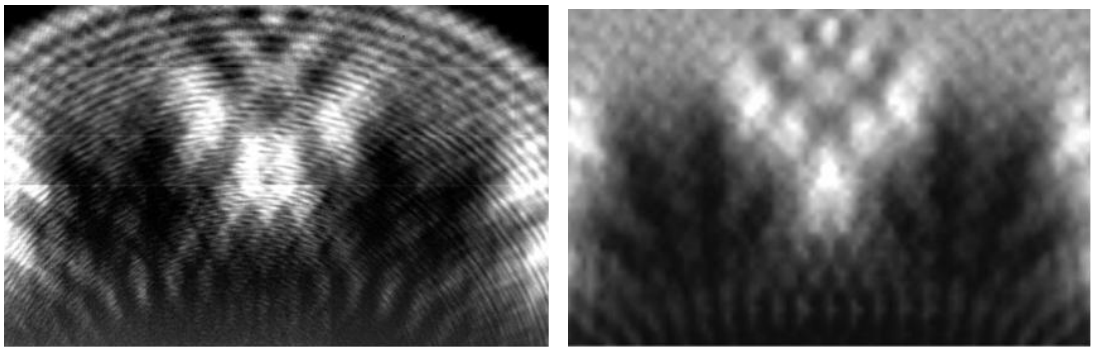

Left: Experimental shadow plane image, where a lens was not used to focus the shadow onto the CCD. Note that the concentric rings in this image are due to an error source which has since been eliminated. Right: A simulated shadow plane image.

Using a lens to focus the shadow onto the CCD, we get the residual light profile shown in the figure below. We estimate that the suppression in this plot is ~10^{-6} at an offset ~2.5 times the IWA (or 2 starshade radii). The suppression level is computed from the ratio of the azimuthally-averaged residual light profile to the peak brightness of the unblocked source. At the IWA, the normalized contrast is currently worse than 10^{-6} due to the wings of a false peak centered about 1.75 starshade radii. The false peak is not a signature of the starshade, but rather an artifact of scatter from the collimating lens which appears in the field of view of the detector lens and is slightly undersized for the collimated beam. The sub-peak emerging at ~1 starshade radius could be the actual signature of the starshade.

It is our first priority to replace the collimating optic which we expect to allow us to measure a true starshade contrast ratio well beyond 10^{-6}. The testbed limitations are currently due to the optical setup and evacuating the vacuum chamber has not been necessary as of yet.

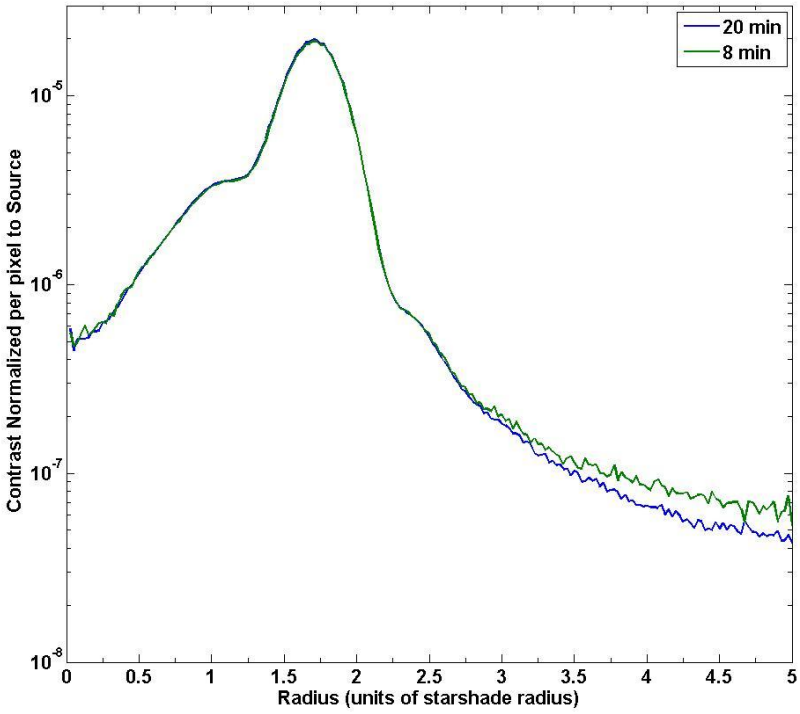

Contrast is estimated to be ~10^{-6} at ~2.5 times the IWA or 2 starshade radii. At the IWA, the normalized contrast is currently worse than 10^{-6} due to the wings of a false peak centered about 1.75 starshade radii.

The testbed will continue to operate in 2009 and a number of improvements will be implemented, including improved collimating optics and a broader-bandwidth super-continuum laser source. In addition, we will continue testing the current generation of silicon starshades, while producing a new generation of starshades with higher precision edge shapes. Our goal in the next year is to achieve a 10^{-9} contrast at the testbed IWA.

White light demonstration of one hundred parts per billion irradiance suppression in air by new starshade occulters

Douglas B. Leviton[a*], Webster C. Cash[b], Brian Gleason[b], Michael J. Kaiser[b], Sarah A. Levine[b], Amy S. Lo[c], Eric Schindhelm[b], Ann F. Shipley[b]

[a]NASA Goddard Space Flight Center, Greenbelt, MD 20771
[b]Center for Astrophysics and Space Astronomy, University of Colorado, Boulder, CO 80303
[c]Northrup Grumman Space Technology Corporation, Redondo Beach, CA 90278

ABSTRACT

A new mission concept for direct imaging of exo-solar planets called New Worlds Observer (NWO) has been proposed. It involves flying a meter-class space telescope in formation with a newly-conceived, specially-shaped, deployable star-occulting shade several meters across at a separation of some tens of thousands of kilometers. The telescope would make its observations from behind the starshade in a volume of high suppression of incident irradiance from the star around which planets orbit. For an efficacious mission, the required level of irradiance suppression by the starshade is of order 0.1 to 10 parts per billion in broadband light. We discuss an experiment to accurately measure the irradiance suppression ratio at the null position behind candidate starshade forms to these levels. We also present results of broadband measurements which demonstrated suppression levels of less than 100 parts per billion in air using the Sun as a light source. A simulated spatial irradiance distribution surrounding the null from an analytical model developed for starshades is compared with a photograph of actual irradiance captured in situ behind a candidate starshade.

Keywords: starshade, occulter, irradiance suppression, New Worlds Observer, extra-solar planets, exo-planets

1. INTRODUCTION AND TEST OBJECTIVES

Light occulters of new shapes have been conceived which provide significant regions of space in their geometric shadows in which very deep suppression of irradiance occurs, even in broadband light. Dubbed starshades, these occulters would hopefully provide a means to suppress light from a star so that planets around that star (exo-planets) could be directly imaged by a space telescope of modest size and quality. Suppression levels of at least eight orders of magnitude with goals of ten would be required for direct imaging of Earth-like planets at a distance of 10 parsecs.

As proof-of-principle for a proposed new mission called the New Worlds Observer (NWO), tests have been conducted in the laboratory at the Center for Astrophysics and Space Astronomy (CASA) at the University of Colorado to determine how deep a suppression of broadband irradiance in the plane of the starshade itself can be achieved in the geometric shadow of the starshade using scaled-down devices. The objective of the tests described here was to build small, anatomically-correct starshades of candidate shapes, expose them to a beam of light like that from a star, and measure the suppression of irradiance to levels as low as one tenth of a part per billion.

2. CONSIDERATIONS FOR TEST CONFIGURATION

2.1 Test Layout

A simplified layout of a suitable test configuration is shown in Figure 1. Light from a source passes through a small aperture some distance from the starshade, simulating a star. The greater the distance from the aperture to the starshade, the more plane-wave-like is the light reaching the starshade. Also, the smaller the entrance aperture, the smaller the apparent angular extent of the source and thus the more star-like it is. The starshade is suspended in the beam some distance from the source by as little structure as possible to prevent that structure from diffracting or scattering light into the irradiance null behind the starshade. A scanning photometer – part of a detector assembly – in the observation plane on the other side of the starshade from the source measures the irradiance pattern in that plane.

* doug.leviton@nasa.gov, phone 1-301-286-3670, FAX 1-301-286-0204

UV/Optical/IR Space Telescopes: Innovative Technologies and Concepts III
edited by Howard A. MacEwen, James B. Breckinridge
Proc. of SPIE Vol. 6687, 66871B, (2007) · 0277-786X/07/$18 · doi: 10.1117/12.742927

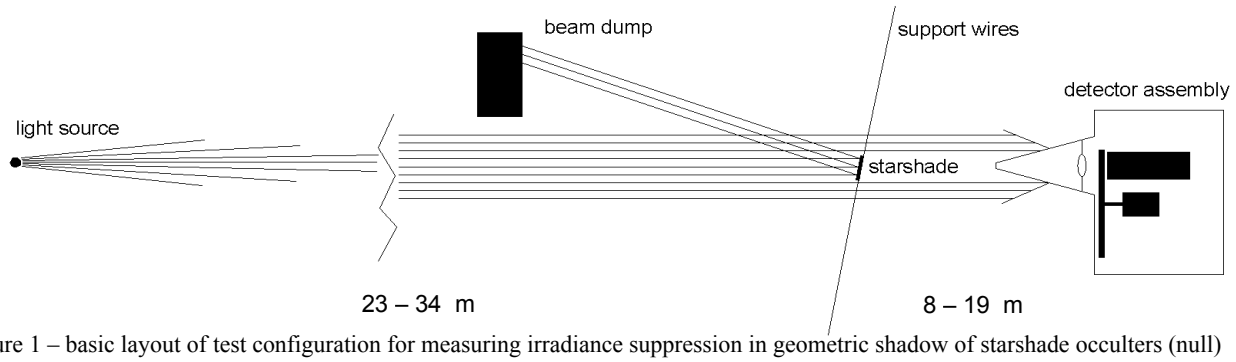

Figure 1 – basic layout of test configuration for measuring irradiance suppression in geometric shadow of starshade occulters (null)

A dark tunnel created by erecting a frame of PVC pipe covered with two layers of 150 micron thick, black, sheet polyethylene blocked external stray light from spoiling the measurement and enclosed the measurement volume, allowing dust particles which would scatter light into the photometer and spoil the null to settle out over time. The facility for the experiment allowed a distance from entrance aperture to photometer within the tunnel of ~42 m. The internal height and width of the tunnel were 2 m and 1.8 meters, respectively. Distances from entrance aperture to starshade ranging from 23 m to 34 m were used with corresponding distance from the starshade to the detector of 19 m to 8 m, respectively. For those source distances, a 1 mm pinhole had an angular extent of ~6 – 9 arcseconds.

2.2 Measurement Feasibility: Photometric Flux Budget

When planning this measurement, it became immediately obvious that measuring optical flux at a part per billion level of some incident flux requires both a very intense light source and a very sensitive light detector. To determine whether a system which would accurately measure irradiance over ten decades of dynamic range would be feasible, we developed a flux budget in which it was convenient to explore that dynamic range using the properties of the brightest, most readily available, broadband light source – the Sun – and those of the most sensitive type of optical detector – a photon counting photomultiplier tube (PMT) as a baseline. A photon counting system already in hand with a PMT having a bi-alkali photocathode (most sensitive from near UV to blue-green) would be used in this study.

We start by estimating how much solar flux within the spectral response range of our PMT we can expect to come through our system's entrance aperture, assumed for now to be a 1 mm^2 pinhole. The mean bolometric flux from the Sun – assumed to be a 5800 K blackbody – outside the Earth's atmosphere is ~1.35 x 10^3 W/m^2. This is our starting point for estimating what irradiance will actually be measurable in the plane of the starshade.

Using the Planck radiation formula[1] to estimate what fraction of that bolometric energy is within our measurement passband (350 nm, limited by the building's windows, to 550 nm, limited by the long wavelength spectral response cutoff of the PMT's photocathode), we calculate that 25% of the exo-atmosphere solar flux or 3.3 x 10^2 W/m^2 is within that passband. We must further de-rate this value by the transmission of the atmosphere over that passband as well as by the estimated transmission of the building's windows and our feed optics. To be conservative in our budget, let us suppose that only 30% of that available flux makes it through the atmosphere, through the building's window, is reflected off of our three flat fold mirrors and passes through our entrance aperture. This means that the irradiance at our entrance aperture is about 100 W/m^2, and a paltry 1 x 10^{-4} W will pass through our 1 mm^2 aperture within our passband.

At a distance from entrance pinhole to photometer of 42 m, and considering the divergence angle of sunlight passing through the pinhole (~9 mrad), the area covered by our 0.1 mW of energy is a circle ~0.37 m in diameter having an area of about 1.1 x 10^5 mm^2, giving an irradiance at the starshade of 1 x 10^{-9} W/mm^2. If the photometer's collection aperture is, say, ~4 mm^2 in area, then the photometer will collect 4 x 10^{-9} J/s when staring at the entrance aperture. The typical photon energy in our passband is about 3 eV or 4.8 x 10^{-19} J, so the photometer collects approximately 8 x 10^9 photons/s.

The typical quantum efficiency of our PMT over the measurement passband is ~0.2, so that the highest count rate we expect to register is ~1.6 x 10^9 counts per second (cps) using the assumed apertures. If we were to increase the entrance aperture to 3 mm in diameter and detector aperture to 6.3 mm^2, we would boost that signal to about 2.3 x 10^{10} cps. This implies that if the photometer were positioned in the null of the starshade and that null were 10^{10} deep, then our signal

would be 2.3 cps – difficult to measure meaningfully over the ~200 cps dark count rate of our PMT. Meanwhile, we can distinguish between the PMT's dark count rate and a measured limiting count rate of ~240 cps (40 cps above the dark rate) with a signal-to-noise ratio of unity. So, we can barely measure an irradiance suppression ratio of 20×10^{-10} with a 1 s integration time or 2×10^{-10} with a 10 s integration time. With a null only 10^8 deep, our signal would be a readily measurable 230 cps above dark. For the sake of measurement linearity with our photon-counting system, we limit our peak count rate to $\sim 1.5 \times 10^5$ cps. Therefore, when the photometer looks directly at the entrance aperture without the starshade in the way, we require a neutral density attenuator in front of the PMT with a transmission of $\sim 1 \times 10^{-5}$ (ND5).

2.3 Stray Light Suppression

Even a few stray photons can spoil a measurement of irradiance suppression at the 1 part per billion level. For this reason, stray light control in the measurement setup is paramount in importance. While the photometer's design (discussed in Section 3.2) is chiefly responsible for stray light control, a couple of obvious aspects of construction of the measurement layout helped to control stray or re-entrant light. The dark tunnel constructed of black sheet plastic is well-oversized compared to the size of the naturally, slowly diverging beam of sunlight traveling down its length, so there no structure for the beam to reflect off of. Light striking the source side of the starshade is specularly reflected back into that incident hemisphere and is dumped into folds in the black tent material out of the photometer's direct view.

3. APPARATUS

3.1 Heliostat

The Sun makes an ideal light source for these measurements for several reasons. Fundamentally, it is the most intense – and in Colorado, one of the most reliable – sources of broadband light available with a spectrum well-matched to the spectral sensitivity of the PMT's bi-alkali photocathode. When passed through a pinhole aperture, the Sun beam's natural divergence angle (~f/110) obviates the use of baffles to prevent stray light in the setup. Simply letting the Sun beam propagate in an open tunnel results in no scattering edges directly illuminated within view of the photometer.

In order to use the Sun as a source for measurements requiring the better part of an hour to complete, a heliostat is required to track the Sun and feed its light continuously to the experiment. We constructed a heliostat quickly and relatively cheaply by retrofitting a commercially-available, motorized, telescope fork-mount with a flat fold mirror in a cradle in place of the telescope tube to steer the Sun's light in a fixed vector direction, replicating existing mechanical interfaces on each side of the mount's declination axis. Additional, fixed, fold mirrors steered the light through the pinhole at the entrance to our dark tunnel.

Figure 2 shows the telescope mount and a solid model of the cradle which holds the plane of the flat fold mirror so that it contains the mount's declination axis and is centered on mount's right ascension axis. Figure 3 shows the completed heliostat folding Sunlight to the first fixed fold mirror. The heliostat is placed as close as can be to the window and is azimuthally oriented due celestial South as well as possible. The default drive rate of the heliostat which is sidereal is close enough to the solar rate that only occasional tweaks to heliostat tracking are required during the time needed to make even a detailed raster map of irradiance behind the starshade. A user may slew and make fine adjustments to tracking by pressing or tapping up/down and left/right buttons on a pendant control. The direction of sunlight passing through the illumination system is maintained by the proper tracking of the Sun by the heliostat.

A small flat mirror is placed adjacent to the entrance pinhole outside the tent, and the sunlight it picks off is folded again so that it propagates outside the tent along its length to a screen at the operator's station. The operator adjusts tracking during a raster scan of irradiance using the pendant control connected to the heliostat by a long extension cable. The pattern of sunlight on the screen outside the tent is essentially identical to that at the photometer inside the tent. A baffled, silicon photodiode located at the center of the pattern stares back into the Sun beam to monitor and record the solar flux over time. Each photometer reading is normalized to the available Sun flux at the time the reading was made.

3.2 Photometer

Figure 4 is a solid model rendering illustrating the anatomy of the photometer. The main elements of the photometer are the large beam dump with small entrance aperture, an iris which limits the photometer's view volume, a motorized wheel containing calibrated neutral density filters, the PMT, and a motorized X-Y stage. The top edge of the light dump was hinged so that it could be lifted and propped up, and a thermo-electrically cooled CCD camera mounted in place of

Figure 2 – L) commercial, motorized telescope with control pendant extended to remote location using an ordinary ethernet cable with RJ-45 connectors at each end; an external DC power supply provides power to the heliostat system; R) solid model of cradle which fits in telescope fork replicating mechanical shaft features of original telescope assembly (removed); the plane of the flat, elliptically shaped mirror contains the declination axis; the mount's polar axis also passes through the flat's aperture center

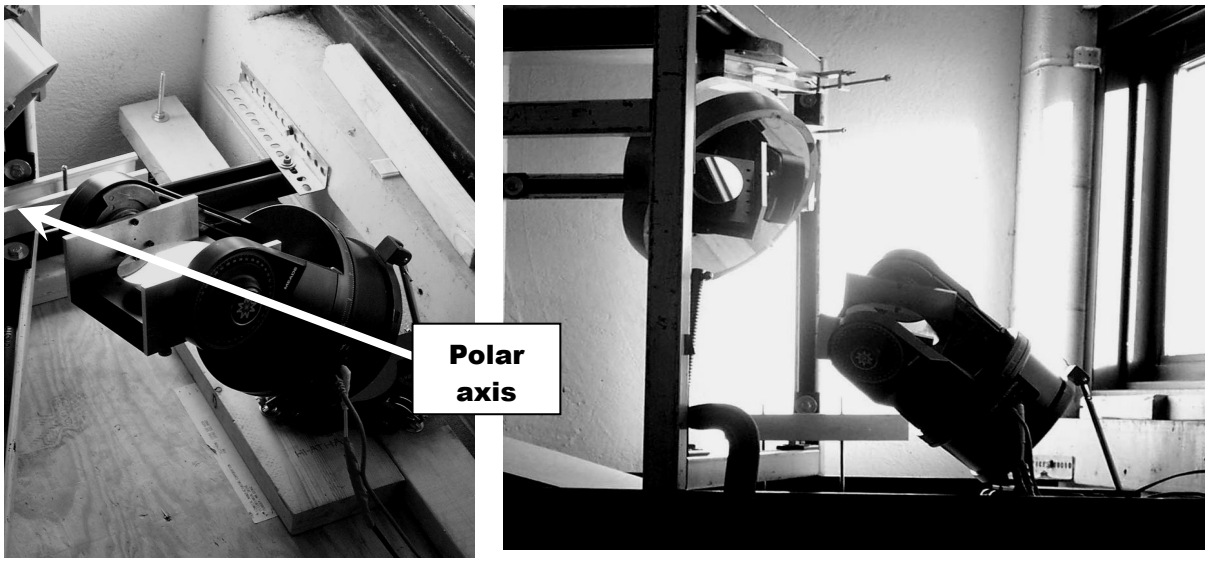

Figure 3 – L) completed heliostat assembly built from commercial motorized telescope mounted in front of a South facing window; R) large flat mirror suspended from a steel frame folds beam from heliostat down and toward entrance aperture to dark tunnel

the photometer could image the starshade and its support wires as well as the photometer's view volume from the location of the irradiance null. The treatment of image data obtained with the camera is described in Section 5.

The two axis, X-Y stage driven by stepper motors has 150 mm of travel and 0.025 mm position resolution in each axis and is arranged to allow the entire photon-counting photometer to be raster-scanned through the irradiance null behind the starshade in a plane parallel to gravity. The entire photometer assembly was mounted on a stiff, right angle bracket and then to a stand adjustable in height, transverse position, pitch, and yaw to allow boresighting of the photometer's line of sight with the starshade and the entrance aperture before measurements commenced.

The beam dump comprises a pyramidal cavity with a specularly reflective, pyramidal foil tip at its center protruding a few cm in front of the cavity. The 0.4 m deep cavity, 0.5 m along each edge, is oversized to accept the entire beam from the Sun regardless of the photometer's scan position. All surfaces (inner and outer) of the beam dump are covered with

self-adhesive, black flocked paper which both deeply absorbs visible light and also diffusely reflects light not absorbed on the initial bounce, allowing that light extra opportunities to be absorbed in subsequent bounces within the cavity. The pyramidal foil piece on the front of the beam dump has its tip cut off to create a square entrance aperture ~2.5 mm on a side and is farthest forward on the detector assembly so that light which does not pass through the aperture skips specularly into the beam dump and undergoes at least two diffuse reflections inside the steep walls of the black cavity.

Once the light has passes through the photometer's entrance aperture, it passes through an iris, sized to create an acceptance cone which when projected to the plane of the starshade, covers an area about four times the diameter of the starshade. The iris restricts the volume of air and dust particles which errantly scatter light into the photometer yet assures that the entire starshade remains in view with margin at any scan position. Any light passing through both apertures is considered to be valid flux coming from the starshade or its supporting wires. A wheel of calibrated, neutral density attenuators was placed immediately behind the internal aperture to adjust the count rate in the photometer.

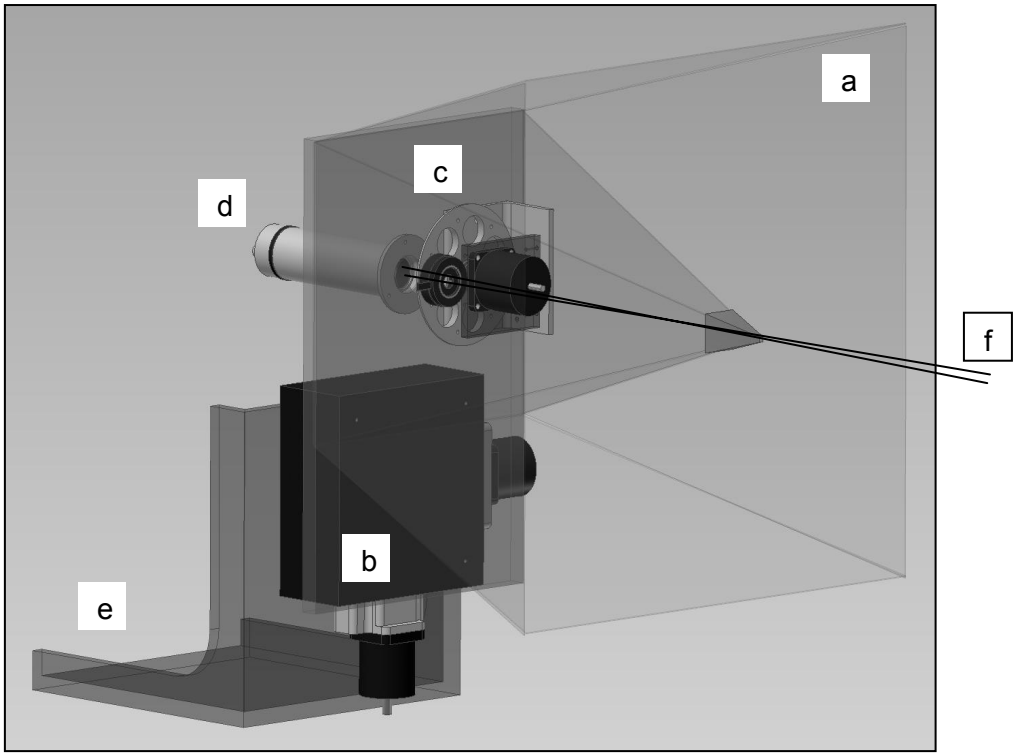

Figure 4 – solid model of photometer assembly: a) light dump (transparent grey pyramidal cavity) with pyramidal aluminum foil entrance aperture tip; b) stepper motor driven X-Y stage (solid black) moves entire photometer in a plane parallel to gravity; c) motorized, detented attenuator wheel (grey) and iris assembly inside light dump in front of d) pulse counting photomultiplier tube (light grey cylinder); e) support bracket; f) black rays crossing at tip and passing through iris depict acceptance cone of photometer

3.3 Starshade Mounting

A wooden frame mount was built to support the starshade under test. Each starshade was suspended from the frame in the Sun beam from three 80 micron diameter, nichrome wires. The frame was large enough to allow great clearance for the Sun beam (Figure 5). The frame also allowed adjustment of the starshade's transverse position within the frame as well as the clocking angle of support wires so that the projection of the wires could pass through the sharp tips of these petal-shaped occulters.

3.4 Automated Instrumentation

A block diagram of the measurement instrumentation is shown in Figure 6. The stepping motor controllers, digital voltmeter, and frequency counter are all controlled by a PC. A silicon photodiode monitors the Sun's flux in real time outside the tunnel at a location equivalent that of the starshade inside the tunnel. An optical power meter pre-amplifies the diode's photocurrent and produces a voltage proportional to incident flux that is logged by the digital voltmeter along with measured PMT counts at each position in the irradiance map.

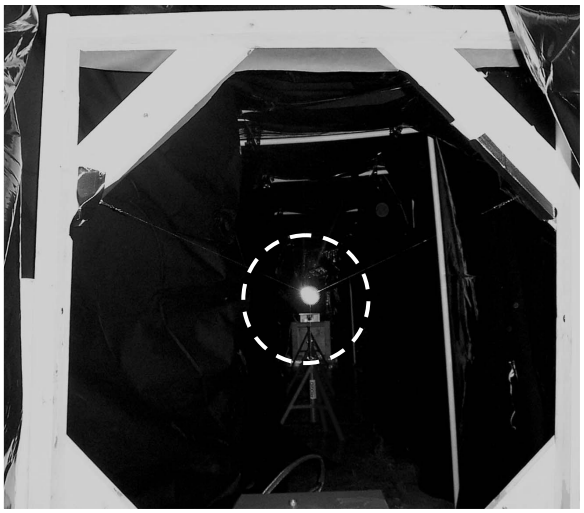

Figure 5 – starshade suspended in beam path by three, fine nichrome wires from custom-built, adjustable wooden support frame; beam diameter from Sun at starshade is indicated by dotted circle

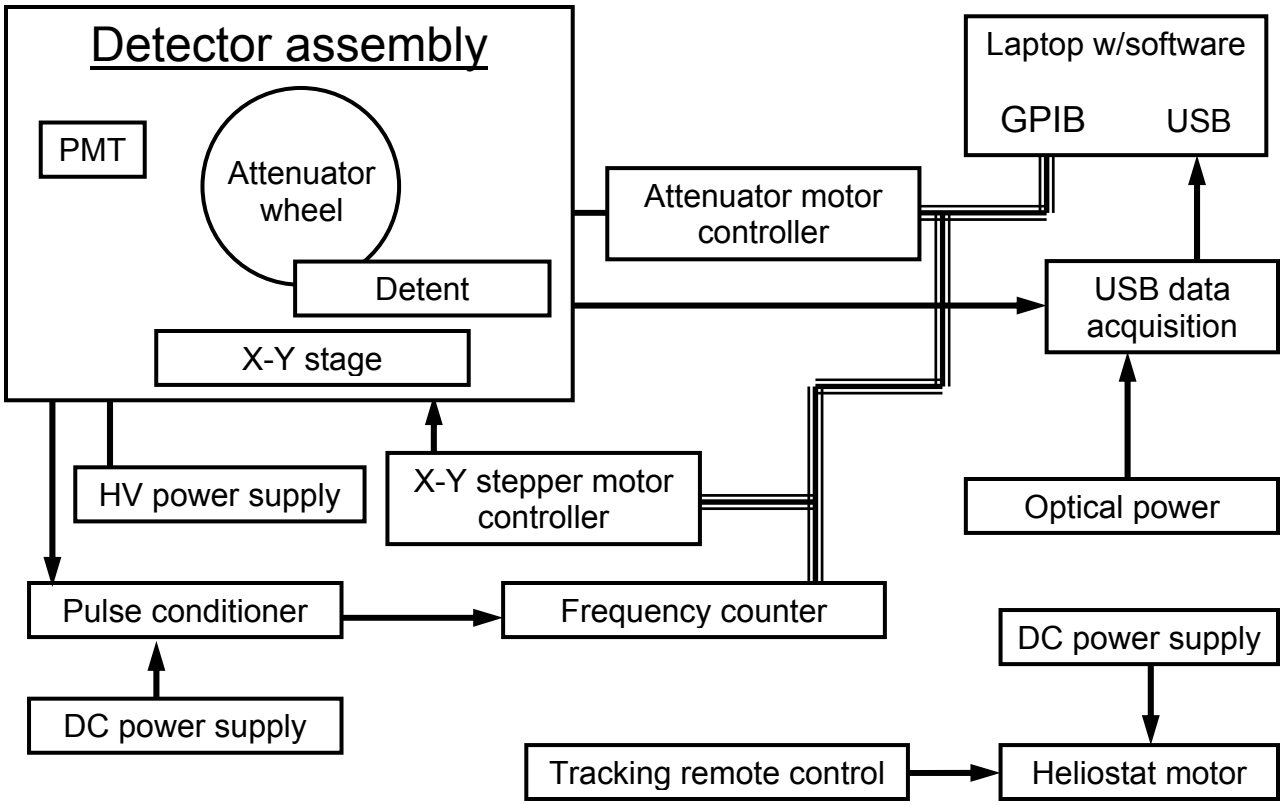

Figure 6 – instrumentation block diagram for starshade irradiance mapping

Light levels incident on the photometer's PMT at any moment were maintained in a range where count rates were as high as possible for optimized counting statistics but below some value above which the risk of pulse pile-up – resulting in non-linearity – would occur. This was achieved through software interchange of the selection of neutral density filters in a motorized wheel just in front of the PMT inside the light dump. At each position in the X-Y map, the PC initiates an integration of counts from the PMT and logs the counts before moving to the next position. If the counts are outside of high or low flux limits, the PC commands a change of attenuation to either decrease or increase counts, respectively, for

the current position before moving to the next position. If counts are below some selected value with no attenuator in place, the PC increases the integration time for that position in the map to improve signal statistics.

The neutral density filters were calibrated in situ in a way which not only established their broadband transmission relative to one another with the Sun as a light source and the PMT as the detector, but also used a wide range of light levels so that the range of count rates which would ensure linearity could be determined. Measurements of flux recorded at each raster scan position using the pulse counter were tagged with time, date, available Sun flux, photometer integration time, and selected attenuation so that a properly normalized map of irradiance could later be re-constructed.

4. TEST ARTICLES

The best starshades tested for New Worlds Observer were made by the National Institute of Standards and Technology (NIST) in Boulder, CO using deep reactive ion etching (DRIE) of the computed starshade shape into a silicon wafer. Two starshades were tested – one with 42 petals and one with 16 petals. Si test articles ranged in size from about 25 mm to 50 mm tip-to-tip. These delicate starshades with vanishingly-small tips (a few microns in size) were supported in the beam by very fine wires clamped to a small puck bonded to its back side (Figure 7) to allow handling without breakage. Each starshade was opaquely coated with aluminum on its input face to make sure that it was truly opaque so that any sort of leakage would not spoil the null. The mathematical form of the petals is discussed in another paper at this conference.[2] Metal starshades made by electroforming were also tested, but, although they were far safer to handle, it is believed that their shapes were not as well-controlled as their Si counterparts – their petal shapes being composed of a relatively small number of line segments instead of smoothly varying curves and their edges rougher and thicker.

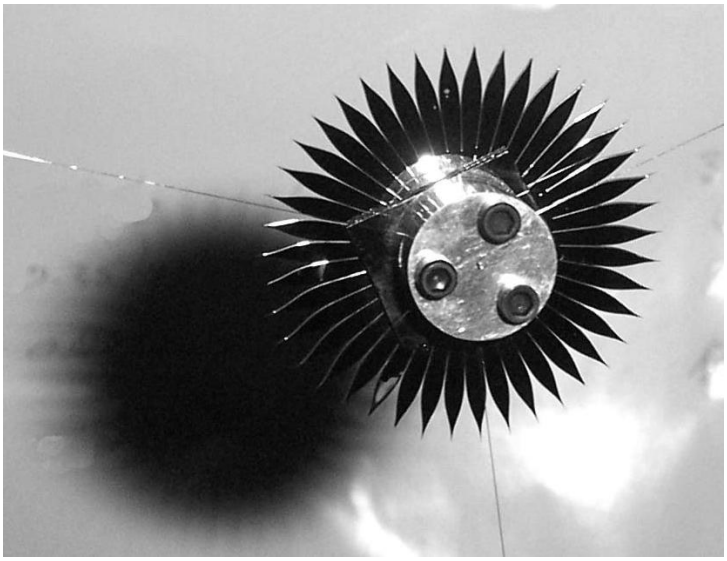

Figure 7 – 42 petal Si starshade supported by fine wires clamped to a puck bonded to the back of the starshade

5. TEST RESULTS

A number of raster scans of irradiance behind starshades were carried out for several test articles. Fairly consistent results were obtained for raw, measured suppression of irradiance of the order of just less than 1×10^{-6}. Here, raw means simply computing the ratio of lowest adjusted signal in a raster map to highest adjusted signal. Adjustment entails computing, for each signal, what count rate would have resulted with constant Sun had raw measured count rate used no attenuator (always the case near the null) and had there been no dark or background count rate from the PMT.

The best, raw, repeatedly measured suppression ratio under the best of conditions with a distance from a 16 petal Si starshade to the photometer of 19 m was 8.4×10^{-7}. Figure 8 shows a quadrant cutaway of the raster map for that raw result accompanied by a similar map made with a circular disc supported in the Sun beam instead of a starshade. The peak in the center of the map for the disc is the expected and well-known spot of Arago – an essentially diffraction-

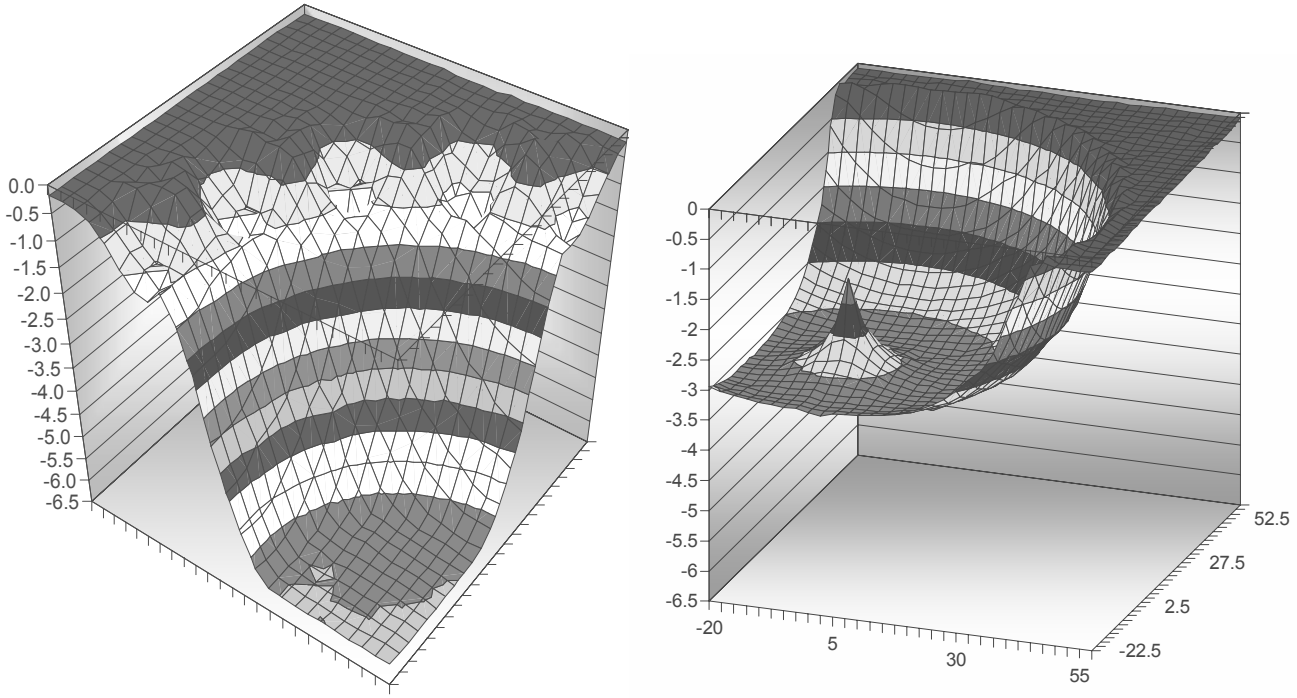

Figure 8 – L) quadrant cutaway of log (base 10) irradiance map for 16 petal Si starshade giving raw suppression ratio of 8.4 x 10^{-7}; R) similarly-scaled map for circular disc occulter illustrates how petal-shaped starshades thwart formation of the spot of Arago

limited image of the source pinhole (peak irradiance level of the spot is underestimated due insufficient spatial sampling to resolve the spot). Figure 9 shows in black and white a recording on color negative film in the plane of the photometer showing the intricacy of the actual diffraction pattern created by the starshade, accurately captured at relatively low spatial resolution by the mapping photometer. Several analytical models of irradiance behind these petal-shaped occulters have matured in the last two years. The features in the irradiance pattern in Figure 10 resulting from a computational method using two-dimensional Fourier transform techniques bear striking similarity to the actual, photographically recorded pattern features in the photograph in Figure 9.

The raw, measured level of suppression of 8.4 x 10^{-7} is referred to the plane of the photometer. Because irradiance goes inversely with the square of the distance from the source, the irradiance of the Sun beam in the plane of the starshade for this particular measurement was 3.3 times higher than it was the plane of the photometer. Thus, the measured suppression of irradiance referred to the plane of the starshade is 2.5 x 10^{-7}. (On station in flight, incident irradiance from a star at the starshade and at a telescope trailing the starshade by tens of thousands of km would be essentially the same.) Electroformed metal starshades consistently performed at the 1 to 2 x 10^{-6} level of suppression, referred to the plane of the starshade.

Numerous sources of stray light are available to spoil the null including: a) light glinting off of starshade support wires; b) light glinting off of dust particles which have attached themselves to the starshade and support wires; c) light diffracting around broken tips or valleys or defective edges of starshade petals; d) light scattering off of aerosol within the view volume of the photometer; e) light bouncing off of the source side of the starshade to structures inside the dark tunnel but within view of the photometer; f) light scattered back out of the light trap on the photometer off the back of the starshade and starshade support structure; g) light from the diffuse sky component surrounding the Sun and illuminating things within view of the photometer.

In order to account for as many of these null spoilers as possible, a cooled, CCD camera was arranged in place of the photometer so that it could image precisely the same light which the photometer detected when the photometer was located in the position of the null. The focal length of the camera was selected to image the same area which the photometer could accept in the plane of the starshade, and the aperture over the camera lens had a diameter substantially

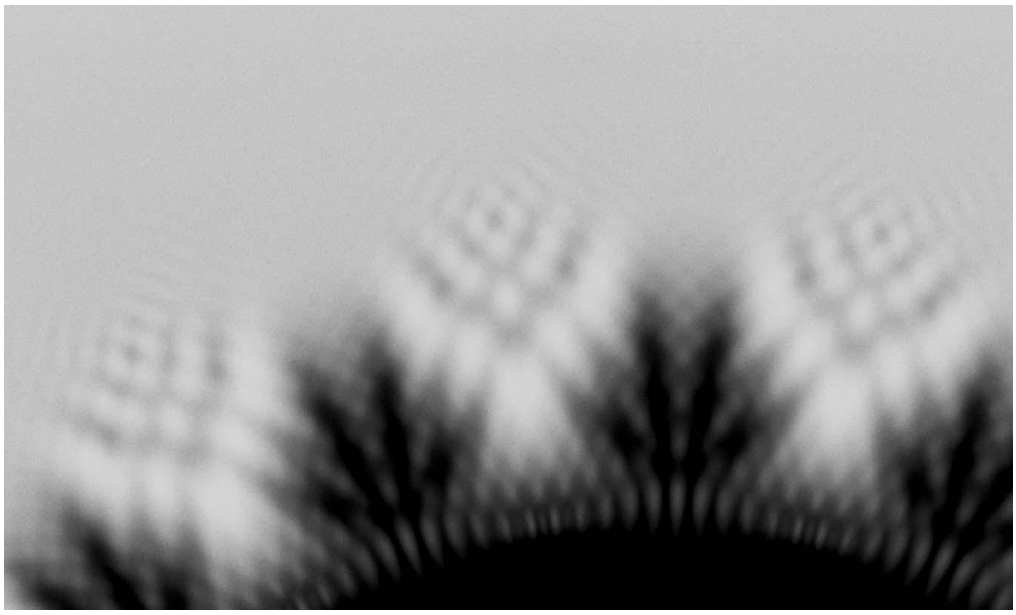

Figure 9 – recording on color negative film shows the intricacy of a portion of the actual diffraction pattern created by 16 petal starshade which could not be resolved by raster scanned photometer

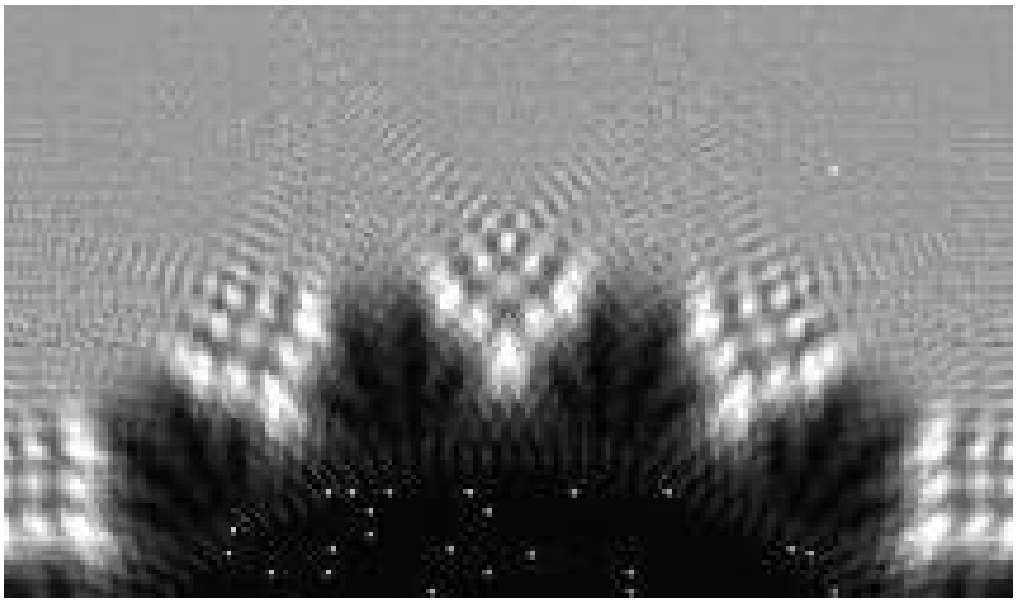

Figure 10 – detail of an irradiance map from one of several computational models of the 16 petal starshade is remarkably similar to actual irradiance

smaller than the measured area of the flat part of the irradiance null shown in Figure 8. That aperture was cone-shaped similarly to the entrance aperture on the photometer itself. Long, dark-corrected camera images (with a dark image of the same exposure length numerically subtracted), allow accurate accounting of how much relative flux collected by the photometer came from support wires, dust particles and obvious defects on the starshade, and how much came from the more ideal parts of the starshade itself. This accounting was used to adjust the raw measured suppression ratio to an effective value assuming that the starshade was acting alone in creating the irradiance null measured by the photometer.

Figure 11 (top panel) is a 60 s exposure, dark-corrected, digital image of the 16 petal Si starshade taken shortly after the raster map in Figure 8 was completed (shown as negative) identifying everything the photometer saw when it was located in the starshade's irradiance null, giving rise to the raw result for irradiance suppression of 2.5×10^{-7}, referred to the plane of the starshade. A simple accounting of image flux shows that 34% of the signal in the null was due to scatter from the starshade support wires and dust particles accreted on them. Without the flux contribution from the support wires (simulated in the lower left image in Figure 11), the measured suppression ratio would be 1.7×10^{-7} referred to the plane of the starshade and 5.6×10^{-7} referred to the plane of the photometer. For comparison, a dark-corrected photo of an electroformed metal starshade (Figure 12) shows petal edges more or less uniformly lit up, clearly illustrating the superiority of the Si starshade in edge shape, smoothness, and sharpness.

The lower middle image in Figure 11 depicts the removal of only the most glaring defects from the starshade itself. Accounting for flux contributions in the null for those defects, a suppression ratio of 1.0×10^{-7} is derived, referred to the plane of the starshade and 3.3×10^{-7} referred to the plane of the photometer. The lower right image in Figure 11 simulates a starshade with all tips as dim as the dimmest tip and all valleys between petals as dim as the dimmest valley, and represents the most ideal miniature starshade which could be made within fabrication accuracy limits. The ultimate suppression value which would have been achieved with such a starshade is 1.0×10^{-8}, referred to the plane of the starshade or 3.3×10^{-8}, referred to the plane of the photometer. Table 1 summarizes the suppression ratios accounting for various measured levels of flux contributions to the null by defects.

The strongest features in the top image of Figure 11 are consistent with naked eye observations from the null location. The wires and edges of the petal at 12 o'clock and several petal tips could be seen faintly glowing. In fact, several of the tips which glowed most brightly were seen to be blunt (broken) under subsequent microscopic examination of the starshade while others remained very sharp. Glowing points along the edges of the petals were found to be dust particles in most cases. These particles were rarely removed so as to minimize risk of breaking the unique and delicate starshade.

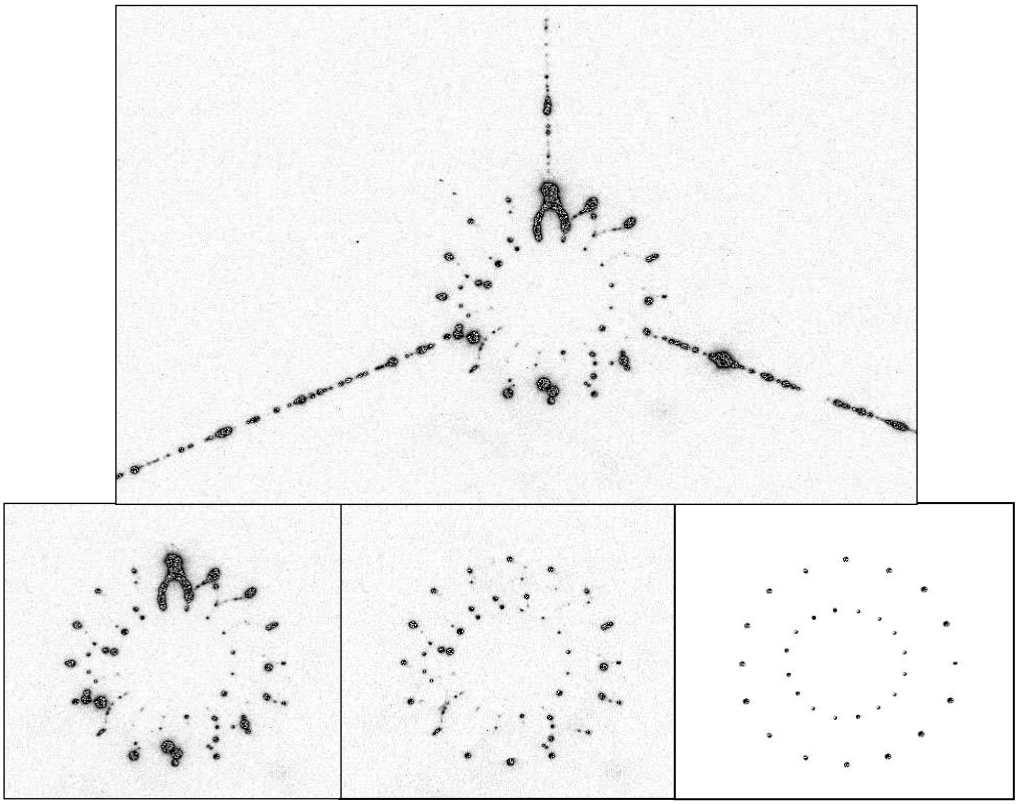

Figure 11 – (top) 60 second exposure image (negative) of starshade showing contributions to flux in location of the null by starshade defects and support wires; (lower left) simulated image of case where starshade defects alone spoil the null; (lower middle) simulated image with worst starshade defects repaired; (lower right) simulated image of case where all starshade tips and valleys are as good as the best tips and valleys – the most defect-free miniature starshade which might practically be made in Si using NIST's process

To this point, the background in the images in Figure 11 has been treated as if it were perfectly dark. However, with one's dark-adapted eye placed in the location of the null behind the starshade 19 m away, one can see the glow of Sun-illuminated aerosol in the dark tunnel within the view volume of the photometer. This glow gave rise to a faint background count in the dark-subtracted camera image which is very dim compared to image features from defects discussed above. Still, a crude estimate of the integrated contribution to the photometer signal in the null of that aerosol glow is up to 30%. To first order, the suppression ratios reported in Table 1 would be lower by as much as 30% if these measurements were done in vacuum, all other things being equal.

Table 1 – summary of raw and adjusted measured irradiance suppression ratios in the null of the 16 petal Si starshade

	Referred to plane of photometer	Referred to plane of starshade
Raw measurement	8.4×10^{-7}	2.5×10^{-7}
Adjusted for glowing wires	5.6×10^{-7}	1.7×10^{-7}
Adjusted for worst starshade defects	3.3×10^{-7}	1.0×10^{-7}
Adjusted so all tips/valleys are same as best tips/valleys	3.3×10^{-8}	1.0×10^{-8}

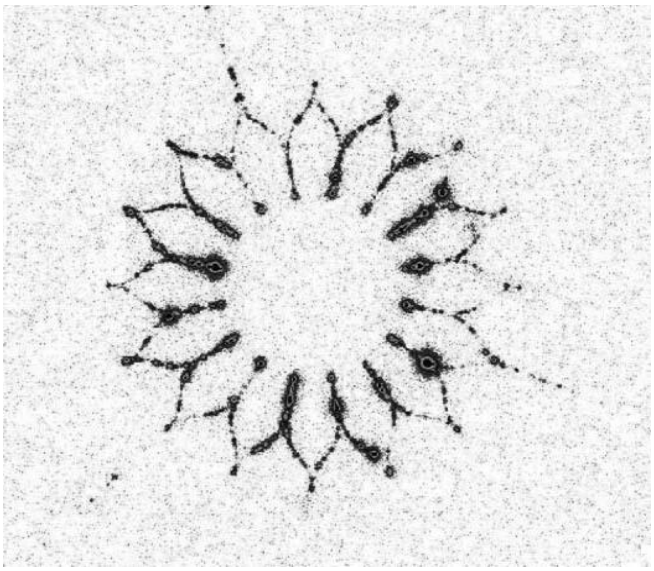

Figure 12 – dark-corrected photo of an electroformed metal starshade; lit up petal edges show how metal starshade is inferior to Si starshade in petal edge shape, smoothness, and sharpness

The photometer signal in the null was ~3% uncertain due to photon counting statistics. Uncertainty in the attenuation value used when the photometer stared directly at the Sun beam is ~7%. The estimated uncertainty in accounting for flux seen by the photometer from defects and contamination is ~4%, treating the image background as dark. So, the estimated root sum square uncertainty in measured suppression ratios is ~10%.

6. SUMMARY

High fidelity miniatures of new candidate starshade shapes have been fabricated in etched Si. A raster-scanned, photon counting photometer has been developed capable of measuring a raw suppression of irradiance of roughly one part per billion in the null behind a starshade. Digital imagery gathered with a cooled, scientific-grade CCD camera from the location of the null behind the starshade enables accounting for flux contributions which spoil the null as measured by

the photometer and allow reasonably accurate adjustments to be made of raw measured suppression ratios. Candidate starshades were found to perform to levels of around 100 parts per billion or lower in air when immersed in broadband light from the Sun. The measurement bandwidth was ~200 nm wide (from 350 to 550 nm) and the average wavelength of the measurement was 450 nm. The fractional measurement bandwidth was thus ~40%.

It is believed that the suppression level measured at CASA was limited in part by scatter of sunlight by illuminated aerosols within the view volume of the photometer. Although the signal-to-noise ratio of the CCD camera imagery is insufficient to quantify this diffuse effect with high accuracy, one can place one's dark-adapted eye in the location of the null and look back at the starshade and see the glowing aerosol column illuminated by the expanding cone of the Sun beam. This visual observation has motivated the adaptation of the experimental setup described here to a 30 m long, 1.2 m diameter, horizontal vacuum tank fed by a large heliostat at the National Center for Atmospheric Research (NCAR) in Boulder, CO to repeat these measurements in the absence of aerosol scattering. These studies are going on as of this writing.

ACKNOWLEDGEMENTS

We give many thanks to Jim Beall at NIST/Boulder for his diligence in fabricating the Si starshades used in this study.

REFERENCES

[1]http://hyperphysics.phy-astr.gsu.edu/hbase/quantum/radfrac.html#c1
[2]W. C. Cash, et al, "External occulters for direct observation of exo-planets: an overview," SPIE **6687-31,** August 2007

Section E: Starshades
Subsection E.3: Starshade Design
Lead Author: Tiffany Glassman

Introduction

In this appendix, we will describe the considerations that went into choosing the current design of the NWO starshade. We will look at the system-wide trades that took place in determining the architecture of the NWO mission, especially the size of the starshade. We will also discuss some of the details of the design, such as the number of petals, and parameters that affect these details. There were many trades considered in this process and many trades will be carried forward for further analysis.

In designing the starshade, we start with performance requirements, such as IWA and suppression, and mission requirements, such as cost and technology development. We analyze the ability of NWO to meet these requirements using models of e.g., the optical diffraction, sky coverage and orbits, and mechanical dynamics. The inputs to these simulations include a large number of design parameters that can be traded, such as the starshade's size, shape, number of petals, and tolerances and the telescope's diameter and wavelength range. These parameters affect the performance in complex and coupled ways. A few have clear optimal values, e.g. the starshade parameter *n* should be about 6-7 (see Appendix E.1 for definitions). However, most of the parameters interact and therefore cannot be optimized separately.

In order to define the applicable NWO trade space, we need to understand these interactions and look at how all the parameters affect each other. A first step is to look at which parameters have the most effect on the requirements and which way each parameter affects each requirement. For example, we find that increasing the number of petals provides a larger shadow but also increases the mass and cost of the starshade. Table E.3.1 summarizes the functional relationship between a handful of key requirements and the parameters that have the largest affect on them. Note that each parameter affects some requirements in a positive way and some in a negative way. We will continue to refine this list and the relationships as we learn more about the system.

Table E.3.1: Functional Relationship between Requirements and Parameters

Requirement	**Baseline Value**	**Better Value**	**Effect of Parameter Change**						
			Bigger Starshade	Larger Separation	Bigger Tel.	More petals	Better shape control	Better alignment control	Less scattered light
IWA	50 mas	↓	↑	↓	↓	N/A	N/A	N/A	↓
Suppression	10^{10}	↑	↑	↓	N/A	N/A	↑	↑	↑
λ Range	0.3 - 1 μm	↑	↑	↓	N/A	N/A	N/A	N/A	N/A
Shadow Size	6 m	↑	↑	↓	↑	↑	↑	N/A	↑
Num. of Obs.	~150	↑	↓	↓	↑	N/A	N/A	↑	↑

Cost	---	↓	↑	N/A	↑	↑	↑	↑	↑
Green = positive effect Black = neutral or no effect			Red = negative effect				↑ = increased value ↓ = decreased value		

Choosing the Mission Scale: first attempt at taming the trade space

In order to trade mission parameters, we need to know more about how they affect the performance. We do not yet have a full end-to-end model of the NWO system that can tell us exactly how the performance changes with each parameter. We therefore need another way to narrow down the complex trade space so that we can choose a baseline starshade design. This requires simplifying assumptions to control for some of the trade-space complexity. Our first approach to this problem is to focus on two main requirements: starlight suppression and IWA, and two main parameters: starshade size and distance between the starshade and telescope. We can then look at which combinations of size and distance fulfill the requirements and choose baseline values for these starshade parameters. This sets the scale of the mission architecture. Here we show the results of applying this method and use it to illustrate the smoothness and flexibility of the trade space.

To apply this method, we model the optical performance of a range of ideal starshades and determine which cases meet a set of requirements. Figure E.3.1 shows the starshade parameters that are compatible with an example set of requirements: 1) suppression < 10^{10}, 2) IWA < 110 mas, and 3) the combination of these two requirements. The latter gives us a minimum design point – the smallest starshade that fits *both* requirements. If the requirements get more stringent, the design point moves smoothly to a larger starshade, farther away.

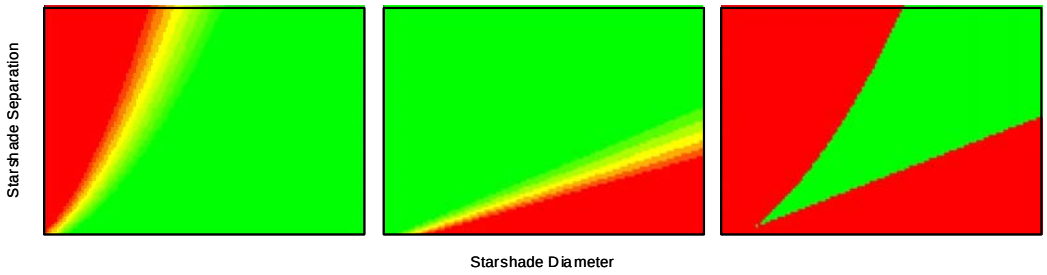

Figure E.3.1: Constraints on the starshade size and separation are shown for requirements of suppression > 10^{10} (left), IWA < 110 mas (center), and the combination of the two requirements (right). The starshade parameters that are compatible with these requirements are marked in green. Parameters that are not compatible are marked in red.

Other performance and mission requirements can also be added to this type of plot and their effects on the parameter space determined. As seen in Figure E.3.2, these additional requirements shrink the design space available, but it is still continuous. From left to right, the top row figures show cases being excluded for the following reasons: 1) Large separation maneuvers take too much time. 2) Large starshades become too difficult and expensive to build. 3) Sunlight scattering from the starshade edge increases the effective

IWA due to the "ring of fire" (at larger separations, intensity drops, so it is less important). On the bottom row, exclusions are due to: 4) Imperfections in the shape of the starshade (from manufacturing or deployment), reduce the suppression provided. 5) Misalignment of the telescope and starshade requires a larger shadow to accommodate these motions. The final design space of starshades that meet all these requirements is shown in the bottom rightmost figure. By constructing a larger starshade, we can accommodate all the factors that affect performance. We find, as a result of this exercise, that NWO is a flexible and accommodating design – it's easy to build in margin for realistic engineering constraints.

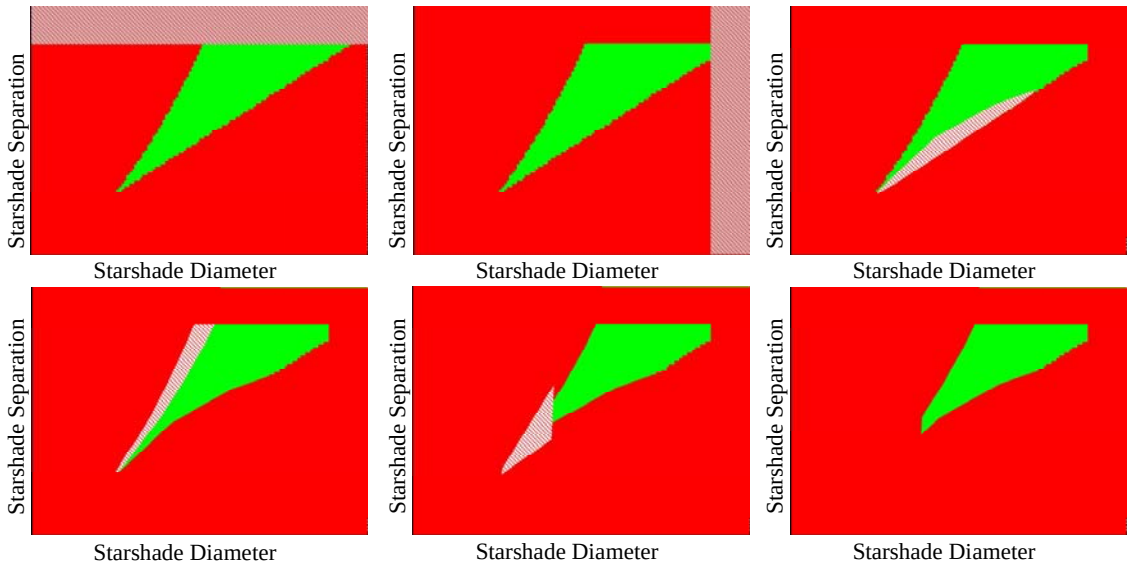

Figure E.3.2: Notional diagrams showing the effect of a series of mission requirements on the available starshade design space. These are the same diagrams as in Figure 1, with starshade size versus separation shown for cases that meet the requirements (green) and cases that do not meet the requirements (red). The light red regions are singled out to show which cases are being excluded by each new requirement.

Another major parameter for which we must choose a baseline value is the number of petals. The biggest effect of the number of petals is on the size of the shadow. The region of the shadow with suppression greater than 10^{10} must be large enough to accommodate the telescope as well as some extra space to allow for alignment errors between the two spacecraft. With the 4 m telescope, we need a shadow size ~6 m in diameter. This value is still very flexible – if we increase the accuracy of the TAC system, the shadow can get smaller; if we find it difficult to meet the ±1m fine alignment requirement, the shadow needs to be larger. The number of petals we use is also constrained from the other direction because additional petals mean additional mass, volume, and complexity in the starshade structure. We find that 16 petals meets the 6m-diameter shadow requirement without extraneous mass. This is therefore our baseline value, but it is subject to change.

Conclusions

Determining the best starshade architecture is a complex process with a large number of free parameters. We have just begun to understand the starshade performance and much more work is needed before we can claim to have fully explored the starshade design space. However, we believe that we have a process that allows us to choose a realistic baseline design and to identify the necessary steps to move forward. This method is very simple in that it uses just two science requirements, assumes that a starshade must provide a suppression of 10^{10} in order to see a planet with a contrast of 10^{10}, and does not provide an easy method to trade between different requirements – it is just a simple way to start exploring the trade space and define a baseline design.

Our next step will be to take a more subtle look at the performance of the starshade. Instead of simple requirements like suppression and IWA, we will directly use the ability of the system to see the target exoplanets. This will entail more detailed simulations of observations of exo-solar systems including:

- Nominal starlight suppression
- Performance degradation from starshade errors
- Telescope characteristics such as PSF, throughput, instrument noise, wavelength range, scatter, etc.
- Astronomical noise sources such as sky background and exo-zodiacal light
- Other astronomical parameters such as stellar color and size
- Realistic models of the population of desired exo-planet targets
- Real post-processing of simulated data

One of the principal tasks is to develop an observatory error budget and a full understanding of the starshade tolerances, so we can accurately quantify the performance loss due to both manufacturing and on-orbit errors. This will also allow us to better understand starshade risks. With this full simulation, we will be able to establish the ability of the system to do the required science in a more direct way.

Section E: Starshades
Subsection E.4: Starshade Tolerance Analysis
Lead Author: Tiffany Glassman

Introduction

The basic performance requirement for the NWO starshade is to suppress starlight by a factor of 10^{10} while allowing planet light ≥ 50 mas from the star to pass. In the previous section, we described the design and ideal shape of a starshade that performs as required. However, it is also critical to know precisely how much the starshade can deviate from its ideal shape while maintaining the required performance. This is one of the tall poles for the NWO system; it is critical to know the shape requirements on the starshade in order to design the structure to meet those requirements. In this section, we describe our approach to this problem and the first steps we have taken in this analysis.

In order to fully understand the shape requirements on the starshade, we must do a system-level analysis of how they interact with other mission requirements. Choosing a point design and developing individual requirements in isolation will not work. This is a major system-trade effort involving the whole mission design. All the requirements on the system will continue to evolve as the mission science case and capabilities are determined and we further understand the interaction of the various elements. Table E.4.1 below gives just a few examples of areas where starshade performance is intimately tied to other areas of the mission.

Table E.4.1: Example Starshade Requirement Interaction

Requirement/Parameter	**Interacts with:**
Wavelength range	Science requirement to get spectra of water line
Shadow Size	Telescope diameter, alignment control system (TAC)
Distance to Telescope	TAC, fuel budget, scheduling/ science program
Tolerance of Starshade errors	Structure/ Deployment, Cost, risk, mass, …

Starshade Distortions

In order to determine how tolerant the starshade performance is to shape errors, we start with an ideal, or nominal, shape and apply distortions to that shape. These distortions could be caused by a variety of errors, such as: Mechanical piece part manufacturing, 1 G assembly verification error, Thermal distortion, etc.

Describing the actual distorted shape of the starshade that would result from these error sources is not straightforward. To approach this problem, we have identifies two methods of describing the shape distortions. In the first method, we have created a set of simple shapes that describe the various ways the starshade could distort. We will determine the tolerance to each of these shapes individually and in combination to help us understand where the starshade is most sensitive and how different error sources combine. For the second method, we have built a mechanical model of our preliminary starshade deployment design as well as some of the error sources such as a thruster firing profile

and a thermal load. We will use a Finite Element Model to determine the response of the starshade to these loads and then model the effect on the performance. This will tie the tolerance work into the reality of the mechanical design and help determine if our baseline deployment scheme meets the tolerance requirements. Ultimately what we will get out of these two approaches is a single set of shape tolerances that the mechanical design of starshade must meet.

Philosophy for Nominal Design

In order to distort the starshade shape and determine the tolerances, we need a nominal shape to start with. In the previous section, we described the ideal, Hypergaussian shape that is our starting point. However, there are a number of choices that can be made in defining the nominal shape that affect the performance of the shade as well as our ability to build the specified shape. For example, the mathematical Hypergaussian shape has petal tips that extend out to infinitely far and get extremely thin. Likewise, the gap between two adjacent petals at the base of a valley gets extremely narrow. We can cut both the tips and valleys off at less than their full length while maintaining adequate performance. The question is, where exactly should we cut them off to maintain excellent performance with room for additional degradation due to the errors we are modeling while also keeping the tips and valleys wide enough to be reasonable. Our philosophy is to create nominal shape that slightly exceeds performance requirements to leave room for errors, takes into account buildability (e.g. not too narrow tips and valleys), balances shadow size and number of petals, etc. The chosen shape is somewhat arbitrary – it will evolve as we learn more about the starshade tolerance and the system as a whole. In fact, this has already happened. The number of petals went from 12 to 16 to allow more alignment tolerance. The valley width went from an estimated cm range to ~50 microns as the optical simulations evolved to higher fidelity.

In order to do the tolerance work, we need to define a minimum performance level that can be easily measured for every error case to determine if that level of error is acceptable. We chose to measure the average suppression in the telescope at a wavelength of 500 nm and allow it to go as low as 10^{-9}. This is fairly arbitrary and really the final performance with all errors taken into account should be about this level, but it's a convenient benchmark to use for now. We can use 10^{-9} because a planet with 10^{-10} contrast to its parent star can be seen even if the total residual starlight is 10^{-9}. Note that we are tolerating large factors of performance degradation. This is not sensitive to a 10% performance fall off.

Tolerance Methodology 1: Basic Distorted Shapes

The first method is to define a set of simple shapes that represent errors that the starshade could have. We will apply these in various ways to turn the individual shapes into an error budget. Figure E.4.1 shows our preliminary drawings of the distorted shapes to

consider. This list will evolve as we learn more. It has already evolved as we tried to model these shapes.

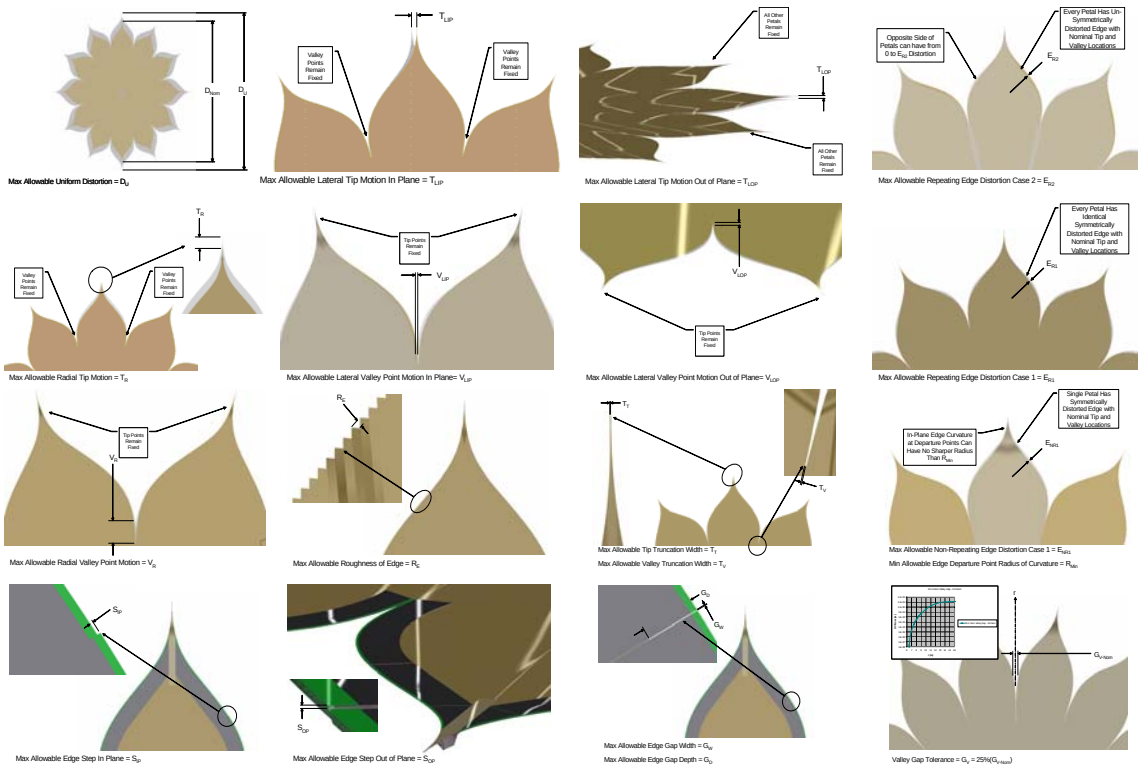

Figure E.4.1: Various Starshade errors.

We next tried to define these shapes mathematically and put them into our optical codes. Some assumptions had to be made about how to implement these shapes which resulted in some changes to our original ideas. For example, some types of shapes turned out to not affect the performance at all while other types of shapes turned into multiple cases. We started by modeling a single instance of each distortion on a single petal.

So far, we have run the case where there is one error at one location – usually meaning on one petal. The next steps are to combine these shapes in these various ways and ultimately come up with an error budget for the starshade tolerance.

The starshade's performance is more affected by some of these distortion types than by others. For example, the performance is very tolerant of uniform expansion of the whole starshade. From our current understanding, it seems that the distortions that are most critical for the performance are ones that:

- Affect the width or length of the tip or valley
- Have a mid-spatial frequencies along the edge
- Coherently perturb the width of every petal in the same way

Tolerance Methodology 2: Mechanical Models

The other method we have started to understand the tolerances is to use the preliminary design of the starshade deployment mechanism. We modeled real loads on the structure and got more realistic distortions for a few cases. There will be a lot of back and forth between the performance model and the mechanical models to come up with an error budget for these errors.

We came up with a mechanical design that we expect to meet the requirements as we currently understand them (see section xx). We then modeled various mechanical error sources that could cause distortions in the starshade shape (see above). We started with thermal and thruster firings. We created finite element models (FEM) of the starshade's response to these errors. This work has just started, so we only have a few test cases to prove the concept, not a full analysis of the tolerances to these error sources.

Conclusions

The next steps in defining the tolerances include:

- Combine individual errors coherently and incoherently
- Increase the fidelity and detail of models of mechanical performance and of error sources
- Use individual error tolerances to understand where the starshade performance is sensitive to the mechanical distortions
- Use a broader range of performance metrics – e.g. other wavelengths
- Combine errors due to different disturbances – e.g. thermal and piece-part manufacturing
- Adjust nominal shape and baseline deployment scheme as necessary to achieve the desired performance within the mission constraints
- Establish up with an error budget that will define the final requirements on the starshade structure

Section E: Starshades
Subsection E.4: Mechanical Design and Deployment
Lead Author: Dean Dailey

Introduction

The Starshade shape must provide a minimum of 10^{-9} suppression of central starlight from a neighboring star system under observation, while permitting unblocked viewing of planets within the system's habitable zone. The shape shown in Figure E.5.1 is designed to be flown in formation with a Starshade/Telescope separation distance of ~72,000 km.

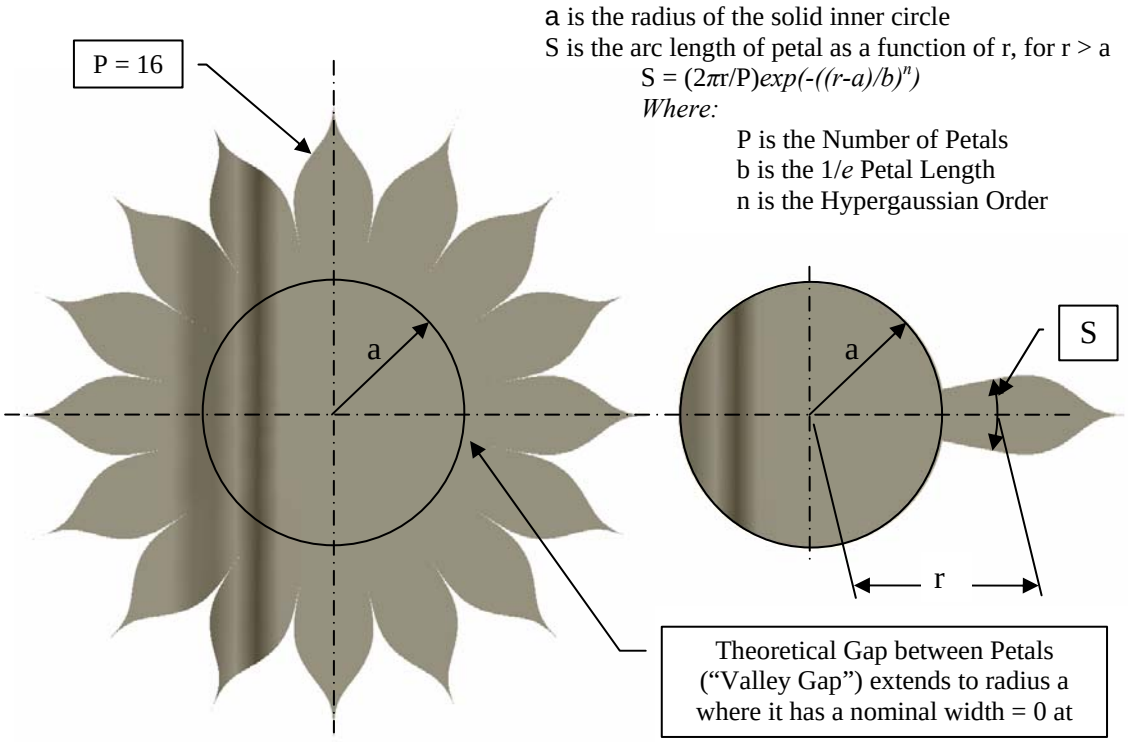

Figure E.5.1: Basic Starshade shape requirement

The basic Hypergaussian shape has an infinitely long tip and a valley gap that extends to the circle or radius a, at which point it has a gap width of 0. Both limits require truncation to provide a shape that may be considered producible as a space deployable design. Table E.5.1 shows these truncations as "trunb" and "trunc" as well as the Hypergaussian design nominal values selected for the 2008 New Worlds Starshade.

Table E.5.1: Basic Starshade Shape nominal values

Symbol	Description	Nominal	Unit
A	solid disk radius	12.5	m
B	petal 1/e length	12.5	m
P	number of petals	16	
n	hypergaussian exponent	6	
trunc	tip truncation raidus	31.3	m

trunb	valley truncation radius	14.3	m
$T_{V\text{-}Norm}$	nominal tip truncation width	1.2×10^{-4}	m
$T_{T\text{-}Norm}$	nominal valley truncation width	5.0×10^{-5}	m

Starshade Mechanical Deployment Concept

The Starshade mechanical deployment design concept begins as shown in Figure E.5.2 in the launch configuration. A stowed set of 16 vertically arranged spoke booms and folded petal frames containing a folded Kapton blanket assembly are designed to be launch locked in a cylindrical volume approximately 7.7 meters tall and 4.5 meters in diameter - suitable for launch. The stowed Starshade is shown as a "top mounted" payload on a notional starshade spacecraft.

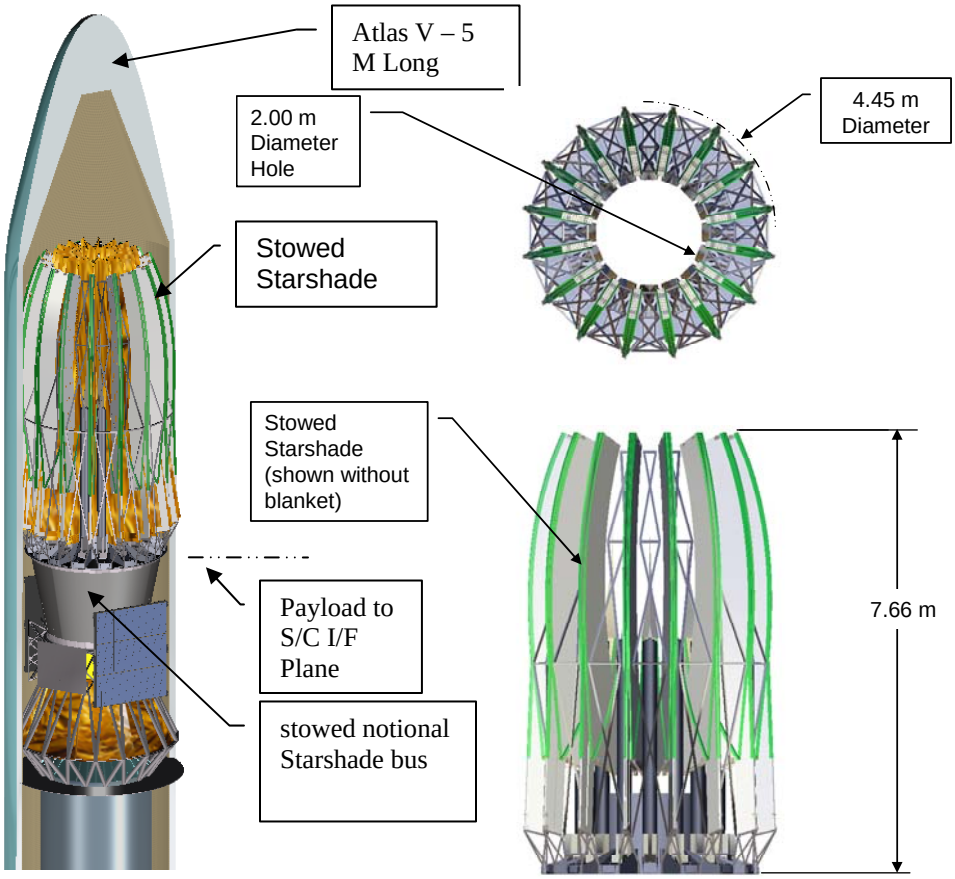

Figure E.5.2: Stowed Starshade payload on notional bus

Mechanical deployment transforms the shape of the Starshade into a 62.6 meter (tip to tip) flower shaped planar object having 16 petals, arranged in a horizontal configuration, supported by 16 spoke booms. The deployed Starshade is shown in Figure E.5.3 mounted to a notional starshade spacecraft. 16 deployed petals can be seen arranged in a horizontal plane, each having Edge Panels supported by a Spoke Boom that is connected

to the edge panels at the tip fitting. The primary Starshade cover (>84% of total area) is provided by a light weight 3 layer Kapton blanket. The view is taken from the spacecraft side.

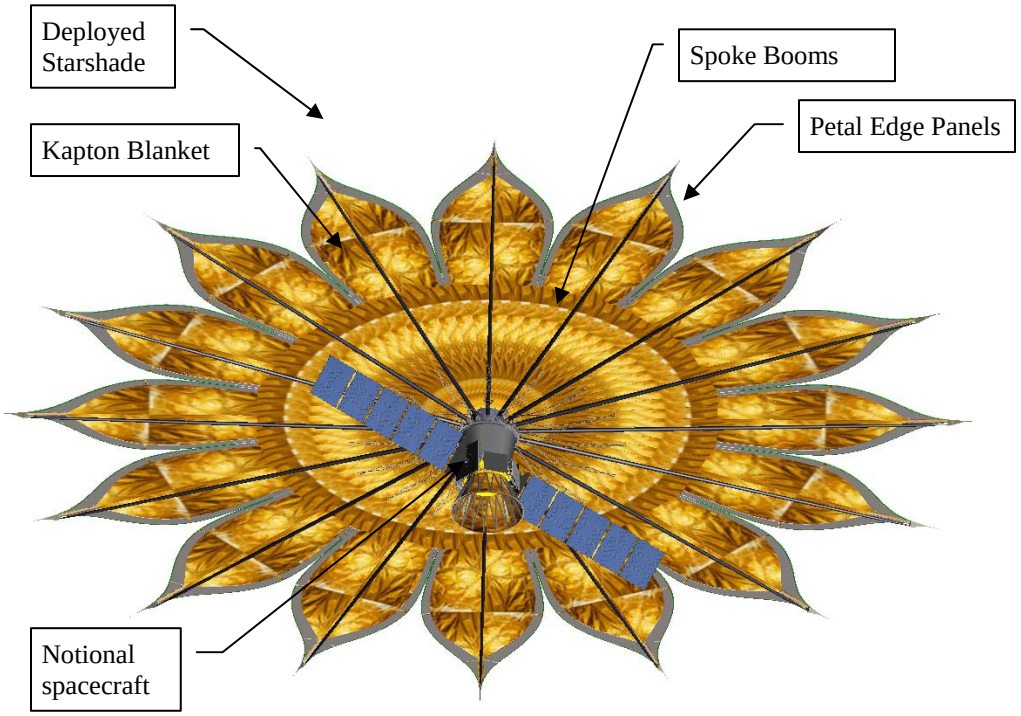

Figure E.5.3: Deployed Starshade viewed from spacecraft side

The primary function of the Starshade is to provide at least 10^{-9} suppression of central starlight from a neighboring star system under observation, while permitting unblocked viewing of planets within the system's habitable zone. A critical derived requirement for the side of the Starshade facing the Telescope is that it must remain completely free of sunlight during planet observations. Figure E.5.4 illustrates the Starshade observation mode sun angle requirements. Also shown is the maximum Telescope to Starshade alignment angle design range.

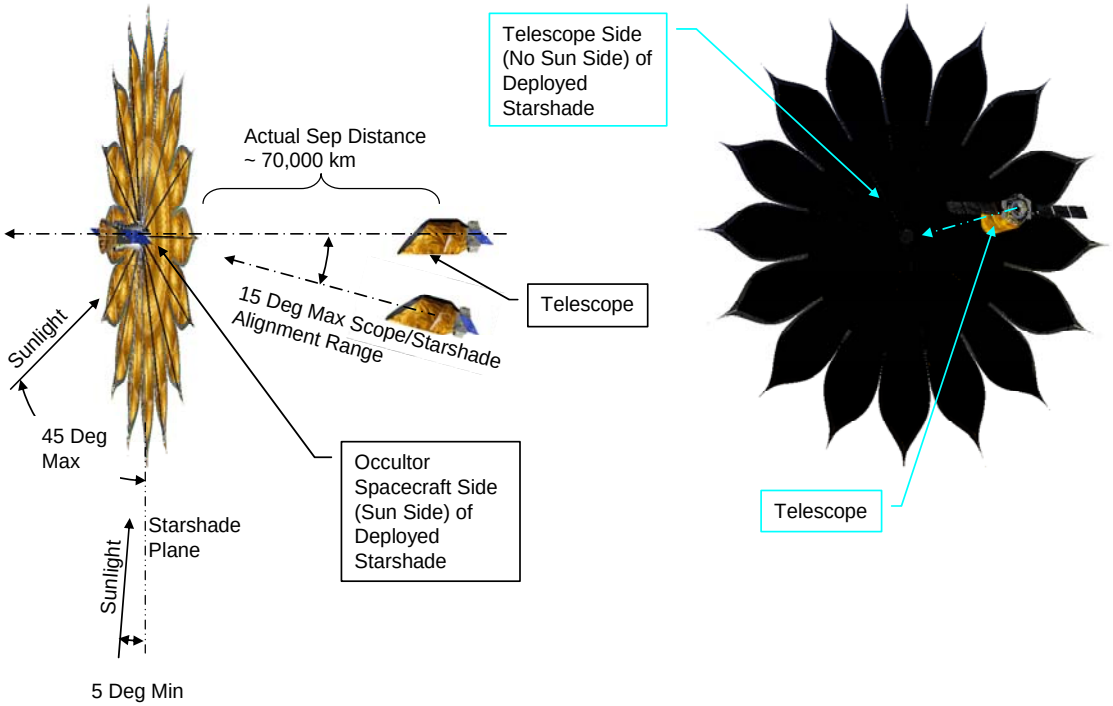

Figure E.5.4: Starshade observation mode sun angle requirements

A 2 meter diameter hole is provided in the center of the Starshade providing clearance for key starshade payload equipment such as the JMAP instrument, Star Trackers and a medium gain antenna for communication with the Telescope Spacecraft. A protective cover for this equipment would be required to protect this equipment during launch and then deployed on-orbit as shown in Figure E.5.5.

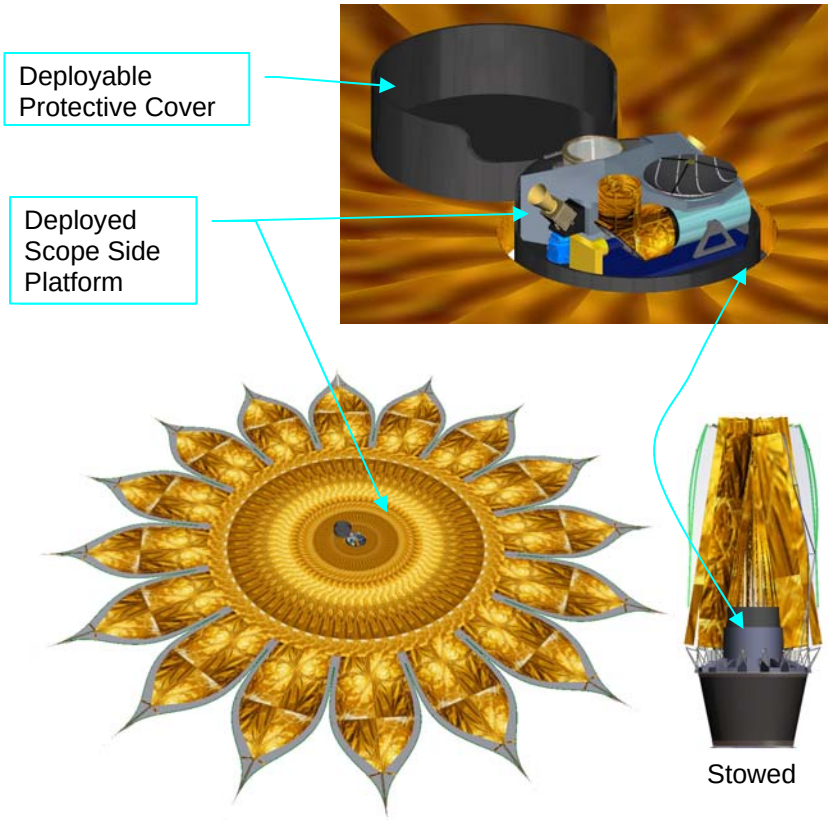

Figure E.5.5: Deployed Starshade, viewed from Telescope side

Figure E.5.6 shows the notional field of regard of the JMAPS beam:

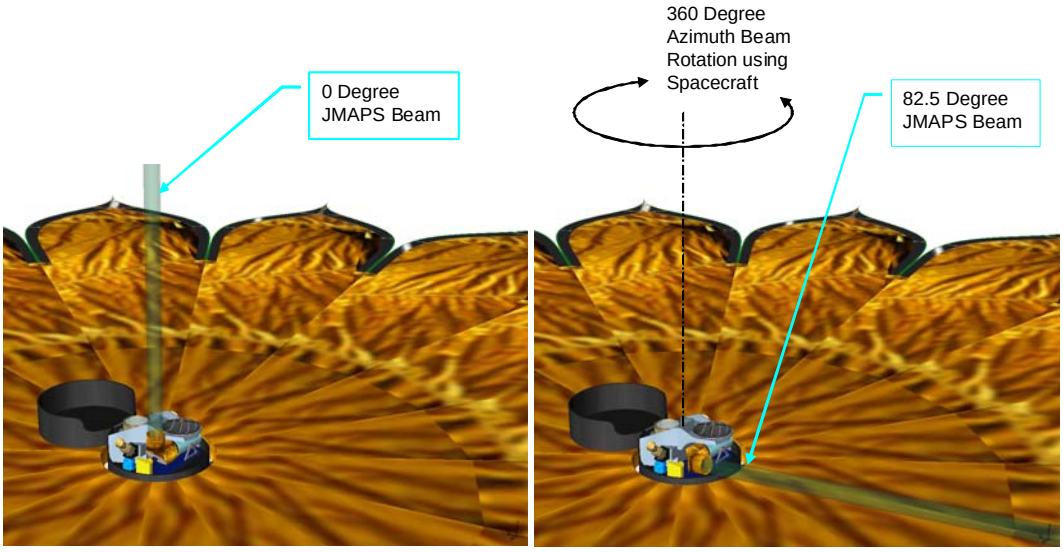

Figure E.5.6: JMAPS field of regard

Figure E.6.7 shows a notional communication antenna field of view

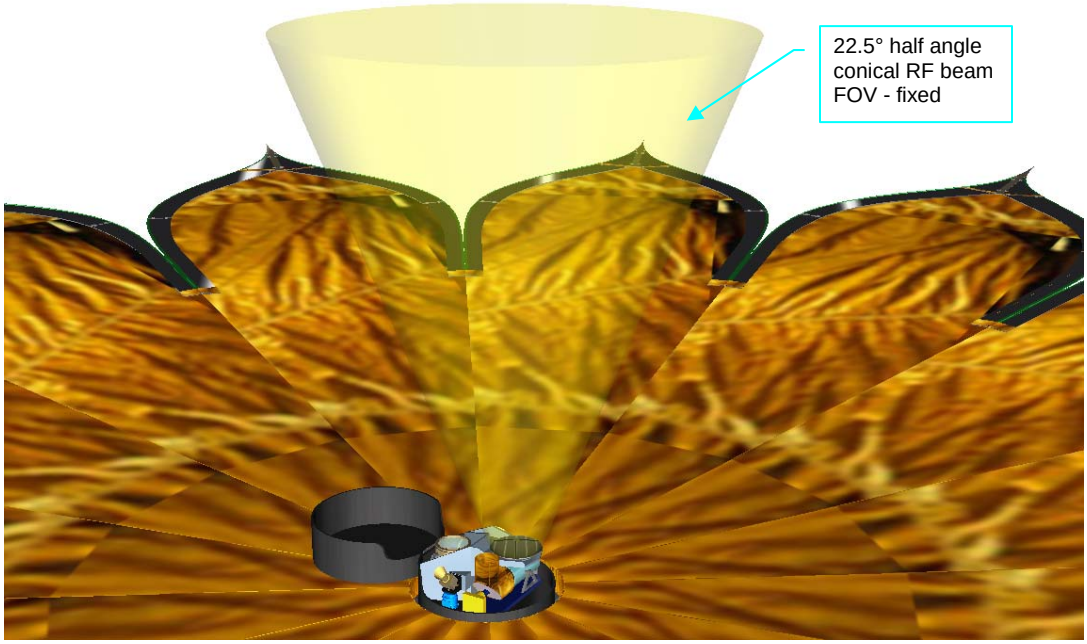

Figure E.5.7: Medium Gain Antenna field of view

Figure E.5.8 shows notional Star Tracker camera orientations.

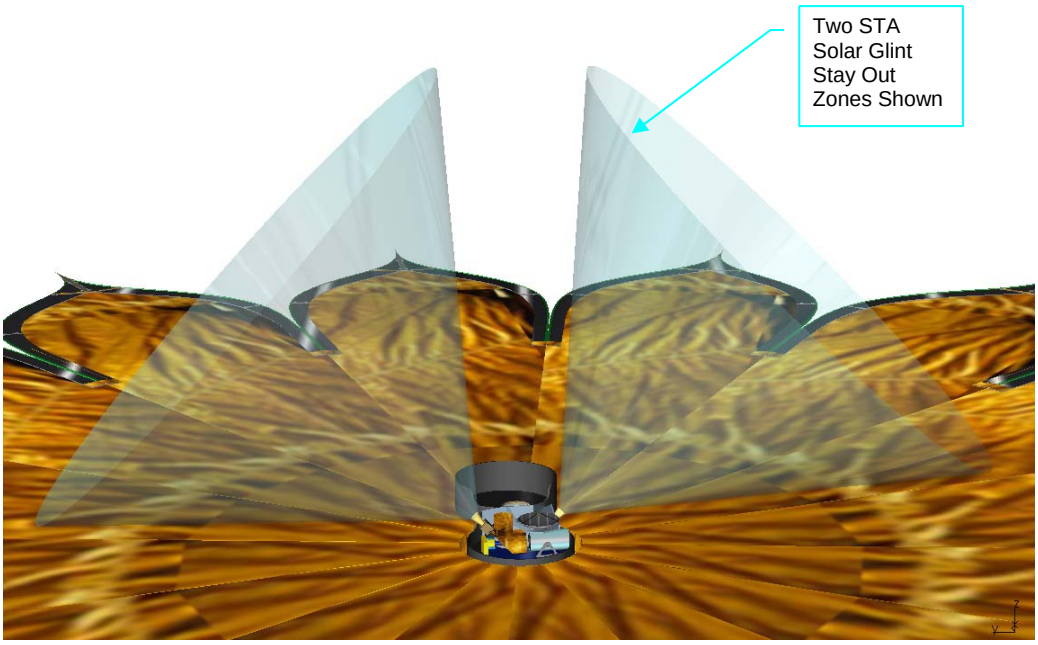

Figure E.5.8: Star tracker notional orientations

All components mounted on the scope side of the Starshade need to be positioned with positive clearance margin to the minimum sun angle Beta as shown in Figure E.5.9.

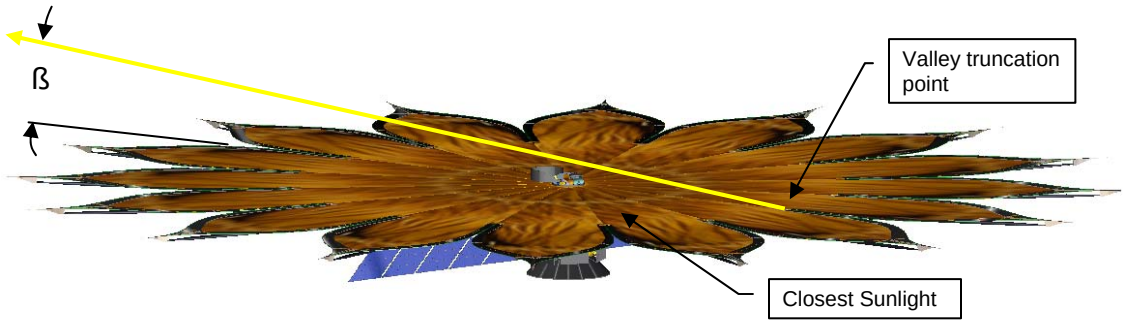

Figure E.5.9: Telescope side sunlight clearance margin

At the core of the Starshade deployment concept is a GFRP hub structure designed to accept cantilever mounting of 16 sets of spoke boom root hinges. Restraint Truss Braces may be attached at their hinge pivots as shown in Figure E.5.10.

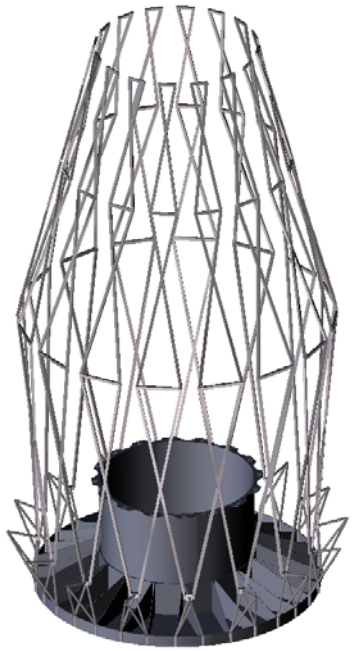

Figure E.5.10: Restraint truss brace installation

The Astro Telescoping Boom Assembly is shown in Figure E.5.11. This would be a derivative of model 7301 (Patent No. 5,315795) and would be tailored as needed for stowed/deployed lengths as well as stem drive details needed to provide approximately 100 N deployed preloading capability. The boom design uses eight or nine stages, each made of thin wall GFRP tubing. Tube overlap sections have doubled wall thickness for strength. At the base would be a spring driven root hinge assembly using eddy current damper resistance to slow deployment if needed. At the tip would be a GFRP tip fitting attached to the inner boom stage.

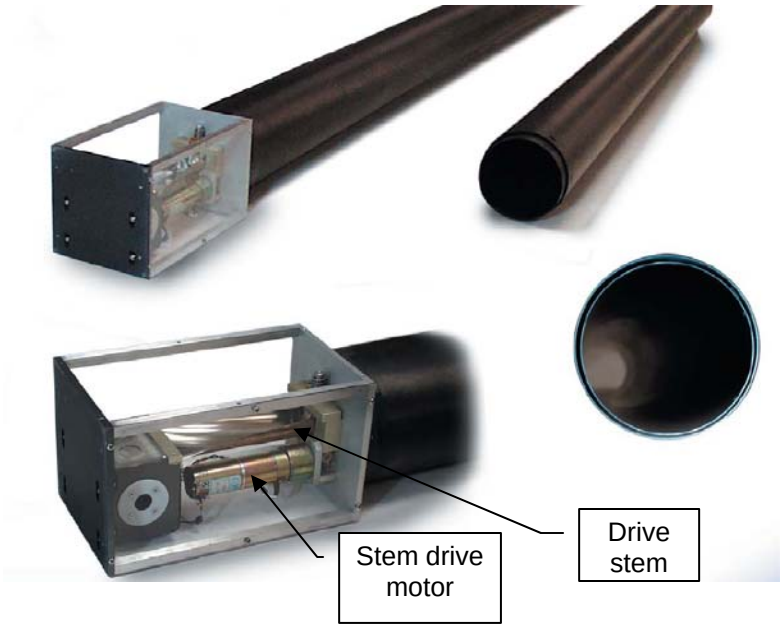

Figure E.5.11: Astro telescoping boom assembly

The Starshade Perimeter Frame can then be stowed and restraint system closed to check and align launch locks between trusses and petals (Figure E.5.12). The restraint system provides an efficient external load path providing for greater than 8 Hz stowed (including blanket mass) with minimal restraint system mass. The stowed configuration of the spherical deployment joint is also shown.

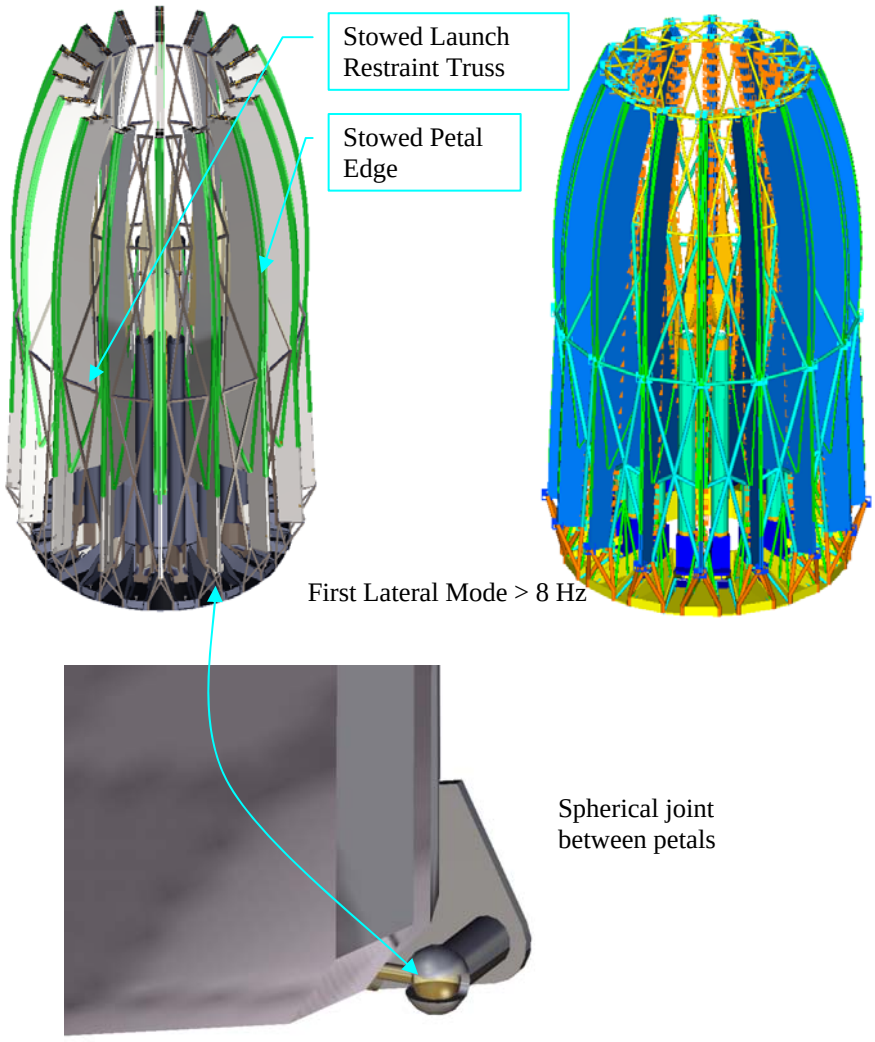

Figure E.5.12: Stowed Starshade frame

All deployment drive forces are provided by either the root hinges or the Stem Drives. The panel to panel hinges would have light deployment springs that would be synchronized by the 3 dimensional mechanism linkage of the petals. Deployment pace of the panel to panel hinges would be provided by the Stem Drives.

The kapton blanket assembly covers more than 84% of the Starshade surface so it's important that the design takes advantage of the mass optimizing potential of the MLI blanket. At the same time, consideration must be given to micrometeoroid protection and basic deployment handling concerns to ensure a robust reliable light shading capability. By using a three layered MLI approach and including lightweight layer spacing features like "pop-up" kapton Z shaped shear web stringers, a very lightweight robust blanket is formed. The three layers increase reliability of surviving micrometeoroid strikes for a couple of reasons. First, the spacing between layers provides a method of staggering micrometeoroid impacts. The first layer impact is thought to provide the micrometeoroid shattering event, producing a subsequent expansion of particles away from the first layer.

The separation distance between layers permits the particle expansion to lower the areal density impacting the second layer. The third layer provides a redundancy in this effect and ultimately provides a much higher reliability of complete blanket assembly penetration. As a fall back, the second reliability enhancing feature is the probability of parallel to bore-sight alignment of a three-hole penetration through the blanket assembly is extremely low compared to a single layer puncture. As a third reliability enhancing feature, the blanket assembly acceptable tolerance limits of complete micrometeoroid puncture area (area projected parallel to bore-sight) are being assessed as 1500 mm^2 (8.2e-7 * Total Starshade Area).

Figure E.5.13 shows the design using two outer layers of 50 micron silicon coated Kapton and an inner layer of 25 micron silicon coated Kapton. Internal pop-up Z-Stringers are made from 125 micron Kapton with lightening holes, forming half meter bays and providing layer spacing after deployment. Stowage and launch ascent require air venting capability so the layers have non-overlapping vent holes as needed to provide good blanket folding and good air escape paths during launch.

Overall transmissibility of the 3 layer blanket should be less than 10^{-9} to prevent starlight passing directly through the blanket from creating noise in a planet imaging 4 meter telescope some 70,000 km's away.

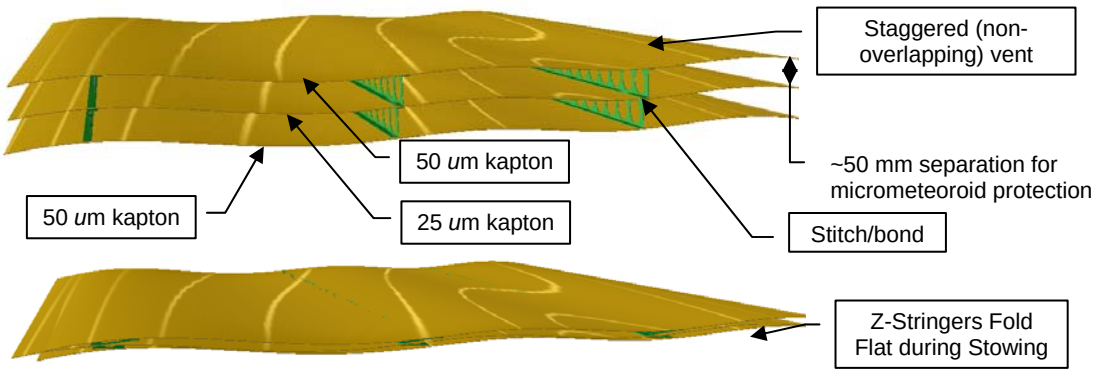

Figure E.5.13: Deployed (top) and Stowed (bottom) starshade Kapton membrane

The Starshade deployment sequence is shown in Figure E.5.14. The restraining truss folds back, and the telescoping booms pushes out the starshade rigid perimeter, while the untensioned Kapton blanket rides out along attachment points.

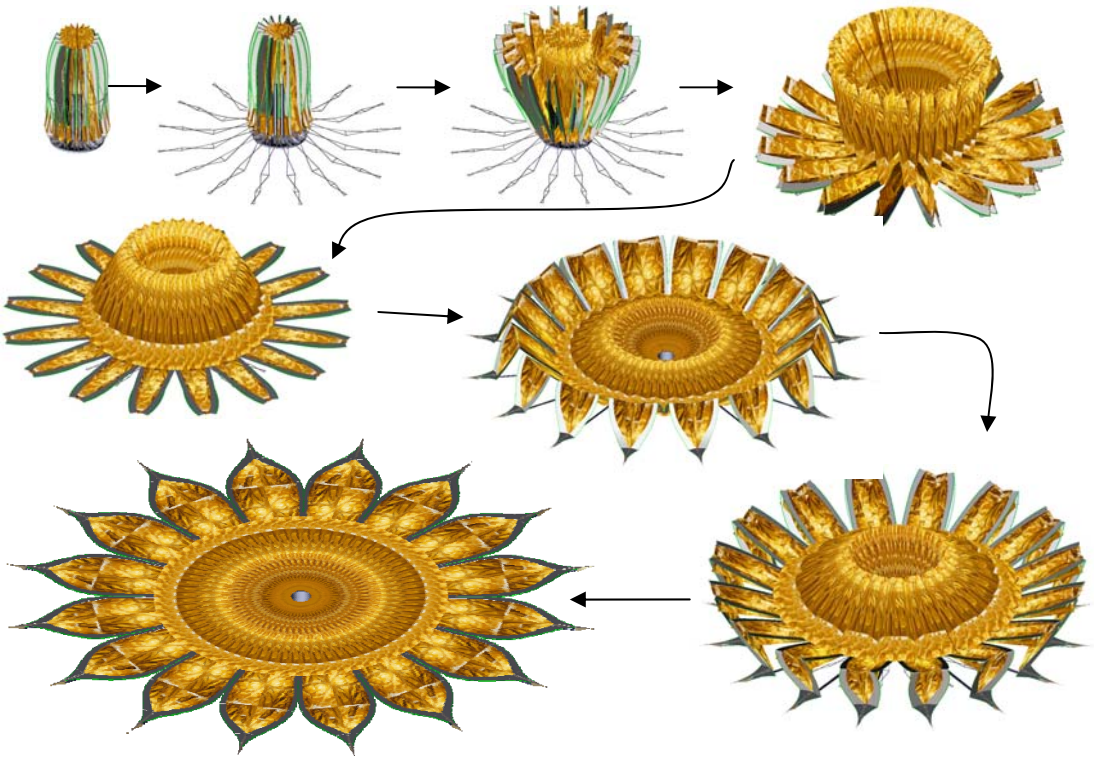

Figure E.5.14: Starshade deployment sequence

Section E: Starshades
Subsection E.6: Starshade Spacecraft
Lead Author: Amy Lo

Introduction

Starshade Spacecraft Functional Requirements

The main function of the starshade spacecraft is to:
1) support the deployment of the ~50 meter starshade
2) enable the starshade to perform occultation of target stars, which includes retargeting maneuvers from star to star, alignment with the NWO telescope spacecraft, and stationkeeping to allow exoplanet observations.
3) enable communication between the telescope spacecraft, the starshade spacecraft, and ground
For a full list of the starshade requirements, please refer to Section D. The starshade spacecraft is illustrated in figure 1, with the payload, communications antennae, and solar arrays fully deployed; close ups of the bus is shown below the fully deployed view for details.

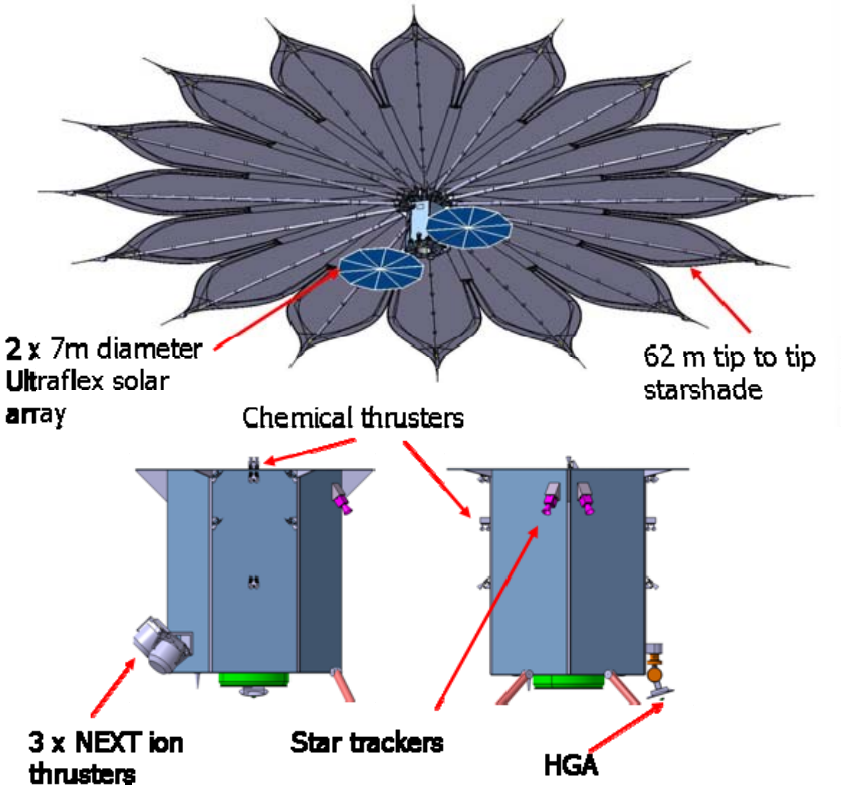

Figure E.6.1: The New Worlds Observer Starshade and Starshade spacecraft

The starshade payload is 62 m tip to tip, and is attached to the starshade bus at the interface plane. This is the only mechanical and electrical interface between the payload and the starshade, designed to minimize bus to payload mechanical and electrical interference. This was done so the bus can accommodate a wide variety of starshade payload designs. For more details on the starshade payload, see subsection E.3 and E.5.

A representative list of trades studied during this study is shown in Figure 2. The green highlighted option is the baseline option.

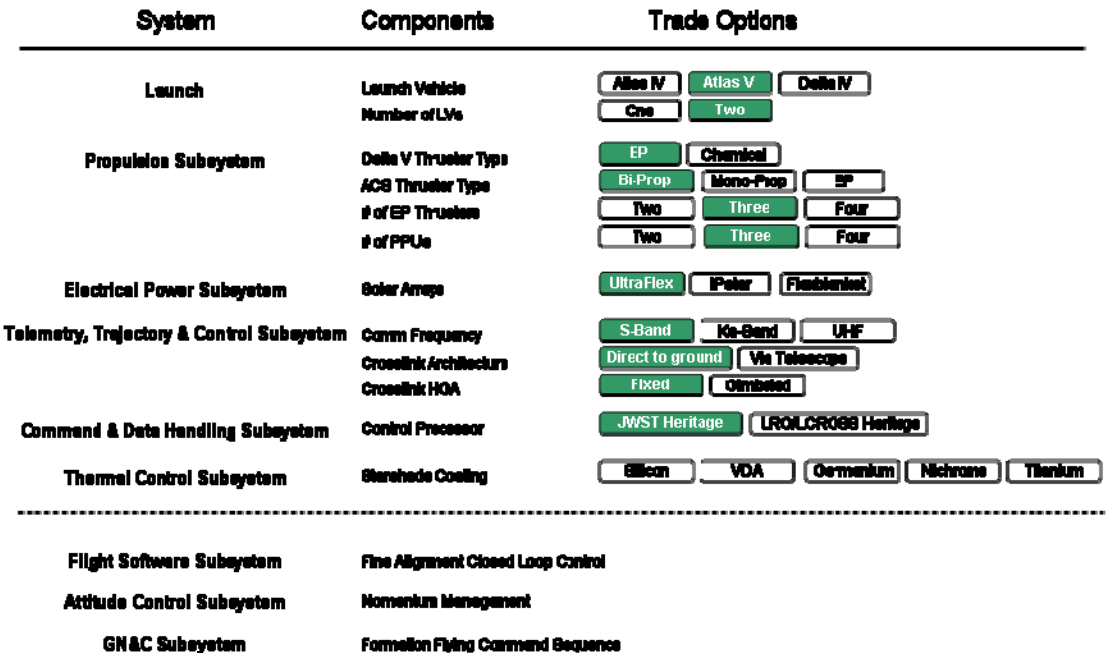

Figure E.6.2: The New Worlds Observer Starshade Top Trades

These trade selections have resulted in the starshade configure as shown in Figure E.6.1. Where possible, the NWO starshade spacecraft uses heritage components and standard parts. The only two elements not currently at TRL 6 are the NEXT engine, currently being qualified, and the Ultraflex array, currently being considered for use on the Orion crew module. The selected trades are discussed below.

Starshade Subsystems

For each subsystem, we outline the function requirement, driving design requirement, and major trades. We show the baseline options chosen for each subsystem.

Propulsion

The functional requirement of the propulsion subsystem is to enable the starshade to slew from point to point, and allow the starshade to maintain alignment with the telescope. As such, it is one of the most important subsystems on the starshade and a primary design

driver. With a baseline of 72,000 km separation between the telescope and starshade, a 10 degree slew, for example, requires the starshade to travel around 12,000 km.

There are two maneuver requirements for the starshade:

1. We derived using the NGST NWO Mission Planner, a retargeting delta V requirement of 8000 m/s during the starshade's 5 year mission.
2. We derived using the NGST NWO Mission Planner, a stationkeeping delta V requirement of 175 m/s during the starshade's 5 year mission.

The high retargeting delta V requirement drove the propulsion design to use an Electric Propulsion system, as chemical propulsion would have required the spacecraft to carry more than 2x its dry mass in fuel. The EP system we chose is the NASA Evolutionary Xenon Thruster, NEXT, for its high Isp. The NEXT system is currently being tested and developed. Its projected system statistics are as follows:

- F = 235 mN
- Isp = 4100 s, 6.85 kW to thruster
- 14800 hours burn time accumulated on prototype unit
- With 3 primary thrusters, throughput estimated to deliver 10,193 km/s delta V
- Accelerator electrode life limit estimated at 730 kg
- 7.25 kW input per PPU
- Contamination stay-out zone 45º from grid screen to solar array

After its planned developing and testing, we expect the NEXT system to be able to meet the performance requirement for NWO. We anticipate possibly needing ~78,000 hours of lifetime test extension for NWO, an additional 35%. This could be done as part of NWO's phase A technology development.

The number of thrusters and Power Processing Units (PPU) needed is an area of active study. The top configuration trades for thruster and PPU redundancy are shown in Figure 4. Our baseline is currently option 1 for the most cost effective and least massive configuration. The trades, cost, and hardware masses are shown in Figure E.6.3.

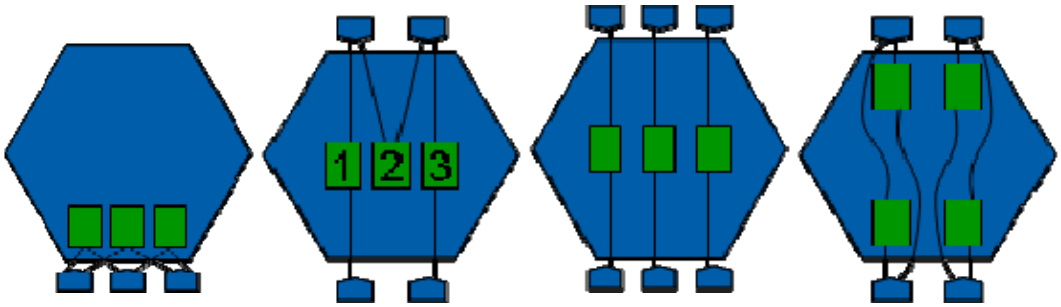

Option 1 Option 2 Option 3 Option 4

Option			Cost	Mass
	#PPU	# Thruster	($M)	(kg)
1	3	3	~13.0	269
2	3	4	15.0	294
3	3	6	20.0	345
4	4	4	18.0	357

Figure E.6.3: NEXT Propulsion system redundancy trades.

For stationkeeping, we baselined a set of chemical thrusters to maintain telescope and starshade alignment. Our simulations of the stationkeeping process indicated that the direction one needs to stationkeep with is highly variable from one target to the next, therefore, the starshade needs at least 2 degrees of freedom in stationkeeping thrust capability. The stationkeeping zone of approximately 1 m also dictated the need to perform a stationkeeping maneuver as often as once every 15 minutes. This is a result of both the gravitational and solar torque differential acting on the starshade relative to the telescope. Lastly, momentum build up (discussed later) requires relatively frequent momentum unloading maneuvers during particularly unfavorable solar orientations. These considerations drove us to implement a separate chemical propulsion system instead of using the retargeting EP system to perform the stationkeeping. The EP system could not be used because it has a limited on-off cycle, and it is too costly and mass inefficient for stationkeeping. Having a highly predictable and high thrust propulsion system adds redundancy and reduces risks for the starshade.

The chemical propulsion system trade resulted in the bi-prop system being selected. While more complex and slightly more expensive, the bi-prop system offered significant mass savings compared to the mono-prop system. The following are the properties of the chemical propulsion system:

- 12 x 22 N Dual Mode DTMs
- 22 N maximum BOL thrust,
- Isp = 290 – 300s
- Off the Shelf Propellant tanks

The NEXT propulsion functional architecture is illustrated in Figure E.6.4. The ion thrusters are run pairwise, with a total thrust of 0.47 N. Three thrusters are carried in total, with pairwise pointing through the center of gravity, and can be compensated by the

20 degree gimbals on the thrusters.

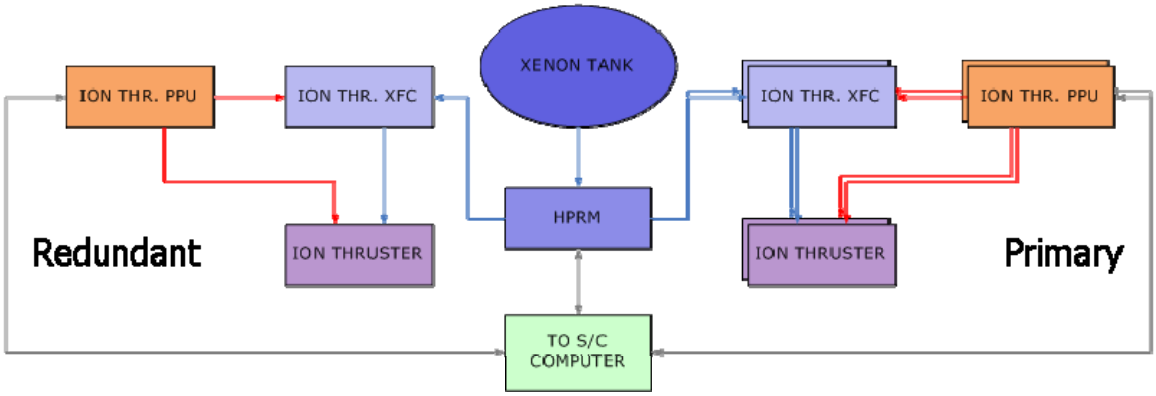

Figure E.6.4: NEXT Propulsion system Architecture

Each 22N thruster for the chemical propulsion system is a dual thruster module, and therefore fully redundant. The 11 thrusters are positioned with 10 on the spacecraft side of the starshade payload, and one on telescope facing side of the starshade payload, located on the payload central equipment panel. This DTM is designed to supply backup z axis maneuverability, should it be needed during a stationkeeping maneuver.

Power

The decision to use the NEXT solar electric propulsion is the major driver for the design of the power subsystem. Here we have listed the requirements for the power subsystem. The major driver is the 14,500 W needed by the SEP system.

- Mission duration: 5 years, 10 year goal
- Orbit: L2, zero eclipses
- Shadowing: penumbra partial shadowing, maximum 40 hours
- Off-pointing: 1 hour for launch and anomalies
- Redundancy: single fault tolerant
- Electric propulsion (80-160 vdc): 14,500 watts

Capabilities of the UltraFlex system are the following:

- 7 meter dia. – TRL6 -150 w/kg
- Each 7 meter provides 9 kW with 30% cells (2 required
- Total weight (7M) : 120 kg

The baseline NWO power subsystem comprises of two, 7 m Ultraflex solar arrays. Power for the NEXT propulsion is run direction from the solar arrays. The battery is sized for penumbra.

1. We also looked at thin film solar array technology, potentially using the back side of the starshade (away from the telescope) as the surface to hold the cells. This was rejected

Telemetry, Tracking, and Command

The starshade TT&C subsystem needs to perform the following functional requirements:

- enable starshade to receive retargeting and stationkeeping telemetry
- distribute JMAPS science data to ground
- enable operation of spacecraft
- 5 year lifetime.

The baseline architecture for NWO's starshade TT&C is to have an independent system capable of both cross-link with the telescope, and downlink directly to ground.

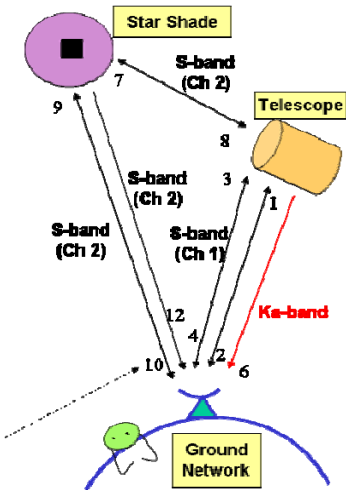

Figure E.6.5: Starshade TT&C Links

The starshade TT&C subsystem is primarily driven by crosslink and downlink to ground. The downlink data rate is driven by the science data downlink for JMAPS, and to provide back up for telescope science in case of failure. The crosslink data rate is driven by the telemetry needed for the Trajectory and Alignment Control system. Those requirements are discussed in Section G. Potential descopes include removing JMAPS science, and this would eliminate the need for the HGA to ground. With the HGA, we have chosen as our baseline a fixed HGA, to save cost.

We have an all S-band TT&C system. Our communications architecture is summarized in Figure E.6.5 and Figure E.6.6.

The following lists the assumptions made in our TT&C subsystem architecture:

- TT&C Links required between Star Shade & Telescope and between Star Shade and Ground (for command & control of the Star Shade)
- Link Design: Telescope communicates with Star Shade using same RF links as the ground to communicate with the Star Shade
- Star Shade ~ 72,000 – 80,000 km from Telescope
- Earth Range to Star Shade: 1.3M – 1.8M km max
- Star Shade Astrometric Instrument requires ~ 12 Gbits/day
- Downlink rate baselined at 2 Mbps
- Ground Network: DSN
- Two Low Gain Antennas (one on each side of Star Shade)

Link	Data Rate	Frequency	Data
1. Ground to Telescope (LGA)	1- 4 Kbps	S-band	Command/Ranging
2. Telescope to Ground (LGA)	125 bps - 2 Kbps	S-band	Telemetry/Ranging
3. Ground to Telescope (MGA)	1-16 Kbps	S-band	Command/Ranging
4. Telescope to Ground (MGA)	1-10 Kbps	S-band	Telemetry/Ranging
6. Telescope to Ground (HGA)	24.5 Mbps [TBR]	Ka-band	Science + Telemetry
7. Telescope to SS (HGAs)	**2 Kbps**	**S-band**	**Command**
8. SS to Telescope (HGAs)	**1 – 16 Kbps**	**S-band**	**Telemetry**
9. Ground to SS (LGA)	**0.008 - 4 Kbps**	**S-band**	**Command/Ranging**
10. SS to Ground (LGA)	**125 bps - 2 Kbps**	**S-band**	**Telemetry/Ranging**
12. SS to Ground (HGA)	**2 Mbps (QPSK)**	**S-band**	**Science + Telemetry**

Notes: 1. SS = Star Shade
2. Telescope-to-Star Shade Ranging available
3. Telescope links and data rates are preliminary estimates for information only

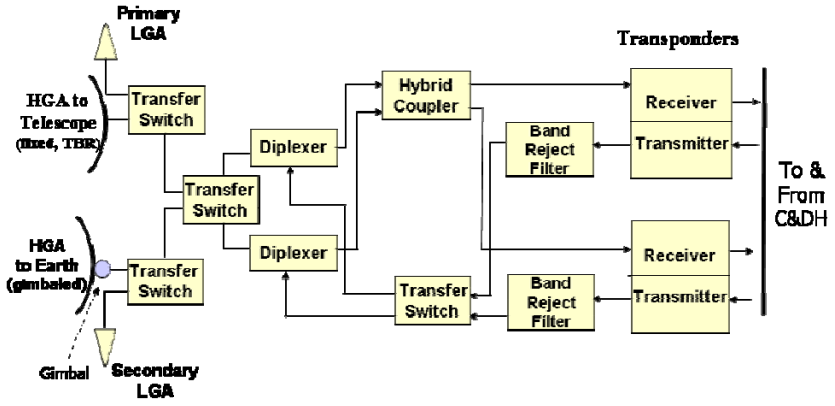

Figure E.6.6: Starshade TT&C Block Diagram

Structures

The Starshade bus has a hexagonal structure with sufficient clearance to the 5 m dynamic envelop of the launch vehicle fairing. The bus configuration allowed us more panels to mount the PPUs and avionics boxes. The panel configuration also allows for a more modular design that eases integration.

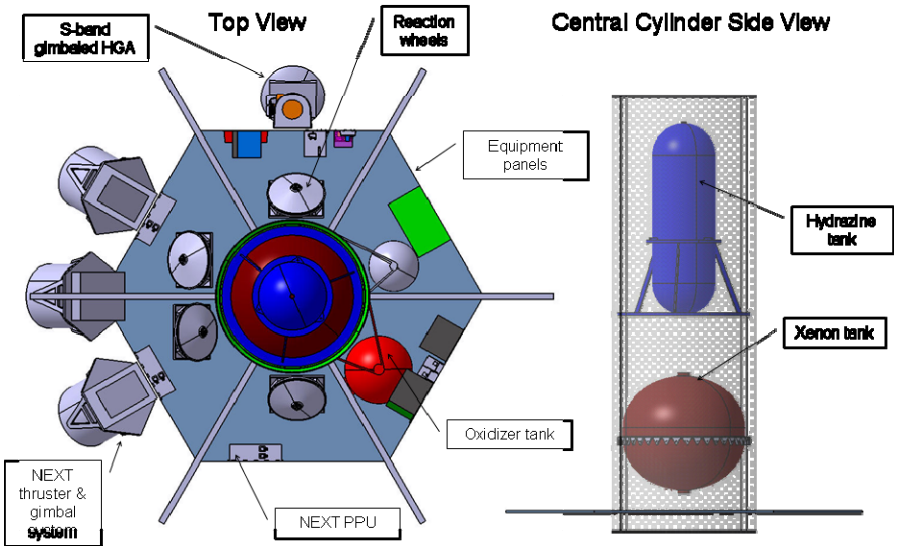

Figure E.6.7: Starshade Structure and bus layout

Thermal Control

The TCS must be able to accommodate sun angles of 0º to 90º (parallel & normal to Starshade), and to dissipate PPU heat from the NEXT propulsion system. The temperature and stability requirements for the starshade are very similar to JWST. The goal lifetime is 5 years, with steady-state duty cycles.

The TCS design uses passive thermal control, mainly via coatings and radiator panels. As the instruments on the starshade do not require cryocooling, these controls are sufficient with heaters to maintain the required temperature stability.

While the starshade payload Kapton layers may experience temperature changes on the order of several 100 ºC, the edges are baselined with graphite wrapped honeycombed aluminum, and will experience minimal thermal expansion. The Kapton layers are designed to be slack, non-tensioned members, and will be allowed to thermally breathe. The boom assemblies are to be thermally controlled with thermal coatings and laminates to maintain acceptable temperature ranges, and the boom stem drive motors to be actively controlled with heaters and insulation during deployment, and then turned off for the duration of the mission.

Normal bus thermal control methods are used, such as aluminum honeycomb radiator panels, embedded heat pipes, second surface mirrors, and the possible use of deployable radiator shades. Electronic panels may use thermal doublers to reject unit dissipations. The bus electronics use heater and sensors to maintain temperature requirements, and the sensors and payloads will have coatings and insulation as required on RWA, STA, and Propulsion units.

Attitude Control

The main function of the attitude control system is to maintain the starshade's attitude during slew and stationkeeping maneuvers. The frequent movement of the starshade and its attitude requirements means this is one of the key subsystems of the spacecraft.

The attitude sensing is done via coarse sun sensors and star trackers while momentum management accomplished by wheels and thrusters. The Bi-prop thrusters are used in pairs for momentum control and pointing, and stationkeeping.

Command and Data Handling

C&DH is handled using standard NGAS C&DH systems.

Guidance Navigation and Control

The GN&C function requirements are covered in the Trajectory and Alignment control section of the appendixes. The system is essentially a distributed system, taking data not just from the ACS and ground, but also from the telescope spacecraft. It is a major subsystem for the NWO Starshade.

Dynamics

We created a Finite Element Analysis model of the starshade payload and bus, both stowed and deployed. For the stowed configuration, we modeled the launch loads and determined that the launch restraints gave the stowed structure sufficient rigidity to withstand launch loads. For the deployed starshade, the primary concern was disturbance to the starshade spacevehicle due to thruster firings. We modeled the thrust profile from the chemical thrusters and determined that the jitter induced on the spacecraft was far below the 1 m threshold required for stationkeeping. Optically, the starshade is very tolerant to jitter, and the design of the starshade payload incorporates jitter control mechanisms (see section E.5). However, spacecraft jitter and stability deserves further study and will be one of the top priorities of the next round of study.

Conclusion

We have performed a detailed trade, analysis, and architecture of the NWO Starshade spacecraft and its subsystems. The final mass rack up is shown in Figure E.6.8. The starshade subsystems, as designed, meet all level 1 and 2 system requirements, but further work should be done to ensure it meets all level 3 and 4 requirements.

Starshade (50m)	MASS			
Component Description	Total Mass w/out Cont (kg)	Cont (%)	Cont Mass (kg)	Total Mass w/ Cont (kg)
PAYLOAD	1574.8	30.0%	472.4	2047.2
Astrometric Sensor (AS)	79.8	30.0%	23.9	103.7
Star Shade	1495.0	30.0%	448.5	1943.5
SPACECRAFT BUS	1252.4	30.0%	375.7	1628.1
GN&C	82.4	30.0%	24.7	107.2
C&DH	60.5	30.0%	18.1	78.6
EPS	148.8	30.0%	44.6	193.4
Cable & Harness	50.0	30.0%	15.0	65.0
Propulsion (Bi-Prop Version)	333.8	30.0%	100.2	434.0
Structure & Mechanisms	482.1	30.0%	144.6	626.7
Primary Structure	319.1	30.0%	95.7	414.8
Secondary Structure	163.0	30.0%	48.9	211.9
TCS	75.0	30.0%	22.5	97.5
SPACE VEHICLE DRY MASS (KG)	2827.1	30.0%	848.1	3675.3
PROPELLANT MASS - Xenon (KG)	1220	--	--	1220.0
PROPELLANT MASS - Biprop (KG)	339	--	--	339.0
TOTAL WET MASS (KG)	4386	--	--	5234.3

Figure E.6.8: Final Mass Rack up of the Starshade Spacevehicle

Section E: Starshades
Subsection E.7: Strategy for Verification and Validation
Lead Author: Amy Lo

Introduction

This section outlines the Verification and Validation (V&V) strategy for the New Worlds Observer. V&V is an integral part of the NWO system development. Although we did not develop a detailed plan during this study, some thoughts and strategies that have been gathered over the years are captured in this package. We outline our main concerns, describe our top-level strategies, and show some examples of how we will apply those strategies. This section does NOT contain details of how to verify and validate particular systems, a specific timeline or plan for V&V, or any quantification of the parameters to be verified and validated. Our goal is to develop a V&V roadmap in 2009 that will include many of those details. This will work hand in hand with our technology development roadmap to show how we will bring the NWO system to TRL 6 and then verify and validate the system performance to the required level.

The Top Three NWO V&V Challenges

For our top three challenges, we have laid out the overarching V&V strategy, the approach we will most likely take, and some specifics where we have pertinent information, in Table E.7.1.

Table E.7.1: Basic Starshade Shape nominal values

V&V Challenge	Mapping to Technology Development	Mapping to Requirements
Starshade Mechanical System	Precision deployment, shape control, starshade membrane material, micrometeorite impact, thermal control	62 m tip-to-tip starshade deploys and maintains shape within specified tolerances
Starshade Optical Performance	Starshade optical simulation, stray light control, diffraction validation	Starshade creates shadow at 10^{-10} contrast and ~50 mas IWA, that is large enough to accommodate telescope and TAC box size
Trajectory and Alignment Control	TAC sensors, TAC algorithms, and communication	Achieves and maintains inter-spacecraft alignment to within ± 1 m

The fist challenge for the NWO V&V plan is the starshade mechanical system, namely the deployable starshade payload, 62 m tip to tip, which must be manufactured, stowed, launched, deployed, and maintained at various levels of precision. One of our primary goals for the next year is to understand the tolerance levels required for the starshade in order to produce a starshade error budget that defines its mechanical requirements.

The second top challenge is validating the starshade optical performance. The large size of the starshade and the large separation between it and a telescope make a to-scale ground demonstration of its optical properties almost impossible. We need to develop strategies that will demonstrate the optical performance of the starshade without resorting

to the expense associated with a large-scale, ground demo. These will involve validated simulations and sub-scale testbeds.

The final top challenge is the V&V of the Trajectory and Alignment Control system (TAC). This is a distributed system across both satellites and the ground and may pose challenges in signal processing and data analysis. We specifically address these three NWO challenges. Our technology development roadmap includes others which are not specifically discussed here.

V&V Strategy

We anticipate using three basic strategies for the NWO V&V: experimentally validated models, judicious use of partial- and full-system testing, and "hardware in the loop" simulations. These are the typical approaches for large-scale projects where full demonstration of capabilities in an equivalent environment isn't feasible.

Experimentally validated models will be used to correlate measurable quantities to on-orbit performance, especially the top science drivers. An example of this type of approach is the use of diffraction simulations to predict a subscale starshade's suppression performance based on measurements of the perimeter shape of the test starshade.

In a few cases, we will manufacture an element of the system as closely as possible to the full scale and test its properties. For example, we plan to build ~20 m long, full-scale petals and test their deployment in a thermal-vacuum chamber with gravity off-loading. We also plan to test the deployment of the full 62-m starshade in an ambient environment.

"Hardware in the loop" simulations will make judicious use of simulations using as-built and flight-like data with validated models. For example, the TAC performance can be simulated using the starshade diffraction modeling to create the input to the shadow sensor, combined with as-built astrometric sensor and shadow sensor performance.

There are several approaches we can take to implementing these V&V strategies. For example, we can perform incremental V&V to buy down risk as early as possible as was done for the JWST sunshield, where they will create up to six pathfinders. For NWO we will start from small-scale and partial deployment demos and work our way to full scale. We will also apply learning from existing programs and use testbeds in parallel with the flight system design.

Challenge #1: Starshade Mechanical System

Our overall strategy for the V&V of the starshade mechanical system is to build pathfinder units of increasing complexity leading to deploying and testing the full

starshade in a large, custom-built chamber with gravity offsetting. Additional testing will possibly be done with a subscale flight demo. The elements that we need to consider in creating a V&V plan for the starshade are the overall 62 m deployment system, the specific deployment mechanisms, control of the edge shape to the required tolerances, and impacts from the L2 environment such as thermal loads, micrometeorites, and charging. Some of the strategies we use will have heritage from existing programs such as the sunshield development for JWST. Although most of the elements of the starshade have high heritage and TRL (such as the joints shown in Figure E.7.1), the deployment system as a whole is new. Incremental testing and verification of the ensemble system will be a critical in ensuring the proper functioning of the starshade

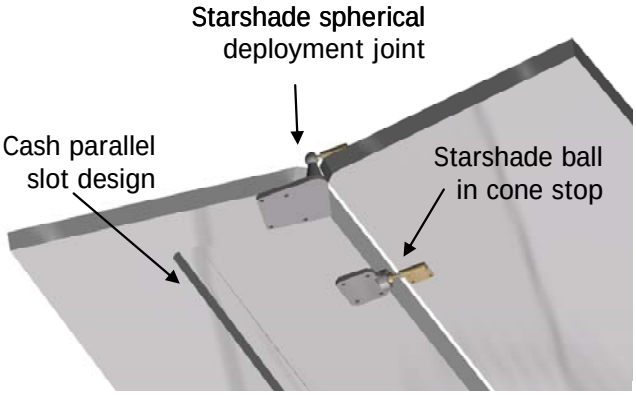

Figure E.7.1: Starshade rigid edge joints

Challenge #2: Trajectory and Alignment Control

Our V&V strategy for the TAC system includes ground tests of the sensor performance, functional testing of the flight control system with simulated sensor stimuli and dummy thrusters, and performance testing of the control algorithms in a simulation environment; facilities such as the ones at JPL and NRL can be used. The control system, though distributed over two spacecraft, is unambiguously controlled from only one, simplifying the algorithm verification. Figure E.7.2 shows an overview of the TAC operation. Key performance requirements to be verified include:

- Astrometric sensor *precision* and *stability* at the 5 mas level (25 nrad), and *calibratable* on orbit to the same level.
- Shadow sensor centroid accuracy to 30 cm or better for a wide range of brightness, and proper acquisition from large offsets.
- Proper software implementation of the operations concept, from slew into alignment control
- Robustness to distributed system challenges, and robustness through the handoffs from one sensor or thruster system to the other.

Again there are existing programs whose heritage we can learn from, e.g. the L2 environment from WMAP and JWST. Orbital Express performed formation flying at a level similar to our 1 m control box, although with a different sensor. Elements that are unique to NWO (distributed control system, sensors, operations concept, and possibly the software architecture) will be tested in simulations and/or “hardware in the loop” tests.

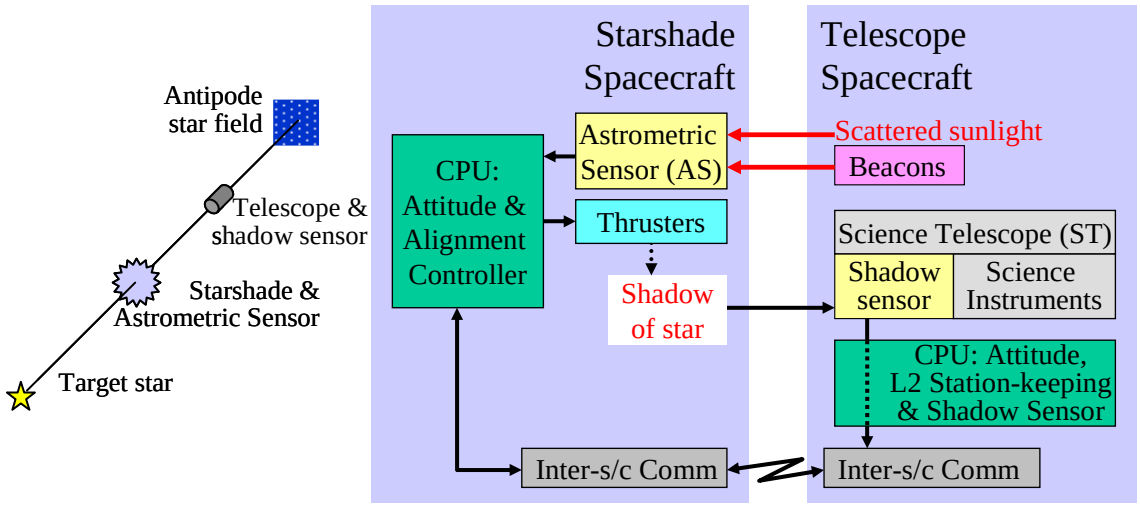

Figure E.7.2: Trajectory and Alignment Control System Overview.
Left: spacecraft and measurement geometry. Right: simplified TAC functional block diagram

Challenge #3: Starshade Optical Performance

Our overall strategy for the V&V of the starshade optical performance relies on measurements of the perimeter shape and edge quality of the deployed starshade, coupled with validated models of shadow performance with respect to its shape. We will validate the optical simulation code using sub-scale testbed results coupled with measurement of full-scale optical components (an example shadow plane image is shown in Figure E.7.3). We are also developing a sub-scale flight demo plan that could demonstrate the optical performance at a scale close to the full size. The main elements that will need to be verified and validated are the diffraction code (to prove that the optics work as claimed), that the light scattered by the edges is within the tolerances, that the starshade opacity is adequate, and that the starshade performance meets the optical and science requirements. There is some similarity to existing programs such as starshade material opacity from the JWST sunshield that may be leveraged. Unique aspects of NWO include scattered sunlight control and precision starshade diffraction modeling and its validation. Several testbeds at the University of Colorado and Northrop Grumman are well underway to demonstrating very high suppressions.

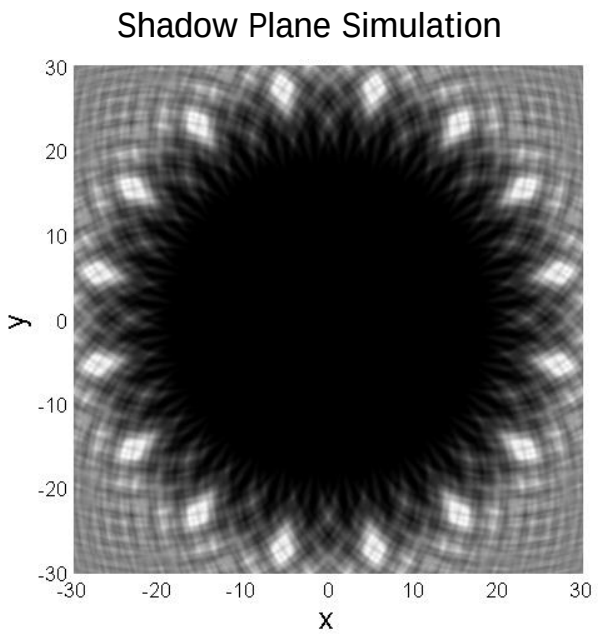

Figure E.7.3: Starshade shadow plane simulation

Conclusion

The NWO study has not developed a detailed V&V plan. We have been iterating the design solution and documenting rationales and believe we now have a baseline design. Following on from this baseline design, we are now starting to develop a V&V plan which we intend finish by the end of 2009. In this plan, we will address the top three V&V challenges, develop a time-phased plan for V&V, develop a time-phased plan for I&T, map NWO faults to science reduction, and develop a risk management plan.